Journal of
Manufacturing and Materials Processing

MDPI

Review

A Review of Optimization and Measurement Techniques of the Friction Stir Welding (FSW) Process

D. A. P. Prabhakar [1,2,*], Akash Korgal [1], Arun Kumar Shettigar [1], Mervin A. Herbert [1], Manjunath Patel Gowdru Chandrashekharappa [3], Danil Yurievich Pimenov [4] and Khaled Giasin [5,*]

1 Department of Mechanical Engineering, National Institute of Technology Karnataka, Surathkal 575025, Karnataka, India; akashk.217me001@nitk.edu.in (A.K.); akshettigar@nitk.edu.in (A.K.S.); merhertoma@nitk.edu.in (M.A.H.)
2 Department of Mechatronics, Manipal Institute of Technology, Manipal Academy of Higher Education (MAHE), Manipal 576104, Karnataka, India
3 Department of Mechanical Engineering, PES Institute of Technology & Management, Shivamogga 577204, Karnataka, India; manjunath.mech@pestrust.edu.in
4 Department of Automated Mechanical Engineering, South Ural State University, Lenin Prosp. 76, 454080 Chelyabinsk, Russia; danil_u@rambler.ru
5 School of Mechanical and Design Engineering, University of Portsmouth, Portsmouth PO1 3DJ, UK
* Correspondence: pavan.prabhakar@manipal.edu (D.A.P.P.); khaled.giasin@port.ac.uk (K.G.)

Abstract: This review reports on the influencing parameters on the joining parts quality of tools and techniques applied for conducting process analysis and optimizing the friction stir welding process (FSW). The important FSW parameters affecting the joint quality are the rotational speed, tilt angle, traverse speed, axial force, and tool profile geometry. Data were collected corresponding to different processing materials and their process outcomes were analyzed using different experimental techniques. The optimization techniques were analyzed, highlighting their potential advantages and limitations. Process measurement techniques enable feedback collection during the process using sensors (force, torque, power, and temperature data) integrated with FSW machines. The use of signal processing coupled with artificial intelligence and machine learning algorithms produced better weld quality was discussed.

Keywords: friction stir welding; process parameters; optimization; Taguchi orthogonal array (OA); machine learning; process monitoring; artificial neural network; response surface methodology

Citation: Prabhakar, D.A.P.; Korgal, A.; Shettigar, A.K.; Herbert, M.A.; Chandrashekharappa, M.P.G.; Pimenov, D.Y.; Giasin, K. A Review of Optimization and Measurement Techniques of the Friction Stir Welding (FSW) Process. *J. Manuf. Mater. Process.* **2023**, *7*, 181. https://doi.org/10.3390/jmmp7050181

Academic Editor: Dulce Maria Rodrigues

Received: 18 August 2023
Revised: 4 October 2023
Accepted: 4 October 2023
Published: 7 October 2023

1. Introduction

FSW is a promising solid-state welding processing route developed by The Welding Institute, UK [1]. FSW-processed aluminum alloy parts produce enhanced mechanical and metallurgical characteristics suitable for defense, aerospace, automotive, and marine applications [2–11]. Aerospace industries fabricate parts such as spacecraft propellant tanks, fuel tanks for Delta II and Delta IV rockets, Eclipse 500 business jet parts (skins: wing, cabin, side cockpit and aft fuselage, engine beam), liquid hydrogen tanks, space shuttles, and airframe structures using FSW processing techniques [3–5]. The FSW process is used in railway industries to join stringers to roof panels, side walls, and floor panels of bullet trains [5]. FSW-processed automotive parts include alloy wheels and rims, crash boxes, drive shafts, bumper beams, fuel tankers, brackets, trunk lid, rear axle and spoiler, frames, manifolds, boosters, vehicle suspension systems, body structures, and tailored blanks [5,6]. Shipbuilding and marine industry parts such as decks, on-board-ship fish freezing panels, inshore patrol vessels, bulkheads, offshore oil platforms, floors, hulls, and internal surface of boats are fabricated viz. FSW [7]. Aluminum alloys' excellent formability, low density, corrosion resistance, and high specific strength led industrialists to adapt the FSW technique to fabricate parts suitable for the above applications [5]. Conventional fusion welded parts for heat-treated alloys result in strength loss and processing difficulties, and the drawbacks can be overcome with the FSW processing technique [8]. The FSW process possesses a wide range of engineered applications attributed to its ability to produce solid joints for various configurations (butt, lap, and spot) of dissimilar metal systems [5,9]. Conventional fusion welding results in deteriorated microstructural (such as porosity formation) and mechanical properties in Al alloys, particularly in high-strength grades [12–18]. Conventional fusion welding techniques are susceptible to hydrogen pores [12] and porosity [13] formation in Aluminum alloys. Although additive manufacturing-based laser processing technology has proven its potential in producing engineering parts, utmost care is essential to overcome the shortcomings of porosity formation in aluminum alloys and limited to thin-walled structures and geometries [14]. Several methods, such as using an external magnetic field [15], wires as filler materials [16], beam oscillation [17], and different joint configurations [9,18], were applied to minimize the porosity levels in laser-assisted welding technologies. The presence of porosity affected the mechanical and microstructure characteristics of the produced joints [13]. The FSW process is a solid-state welding technique wherein parts are joined without melting at a lower operating temperature than conventional fusion welding [1,11]. Therefore, no or minimal porosity and homogeneous grain structure produce better mechanical properties, such as strength and hardness in FSW parts [1,11,19]. The lack of fumes, filler material, and fewer cracks and distortions are the potential benefits of the FSW technique [19]. Simar et al. [20] developed an integrated model for FSW of 6XXX series Al alloys to establish a process-structure–property relationship. The models mainly focused on temperature evolution, their influence on microstructure (precipitation, strength, and strain hardening), and micro-mechanics damage analysis for 6XXX series Al alloys [20]. FSW-fabricated aluminum alloys and different composites grades are discussed in Section 2. FSW uses friction to generate heat (thermal source), leading to plastic deformation that could cause a strong weld bead. Friction stir principles applied to produce strong joints are discussed with different friction stir techniques [21]. The literature focuses on the advantages, limitations, applications, and working principles. There are also numerous works on modeling weld parameters, material flow, and thermomechanical conditions in FSW [22–26]. A 3D thermo-mechanical finite element analysis-based model was established to simulate the process parameter, tool dimensions, and material flow pattern on the behavior of tool–workpiece conditions, temperature, and strain rates [22]. FEM models were established to estimate the torque and temperature distribution at different parametric conditions in welding aluminum alloys [23]. Tool rotational speed and tool dimensions are significant parameters influencing heat generation, whereas the traverse speed and material thickness affect the torque during FSW. The base material properties, plate thickness, and welding condition (welding speed, rotational speed, vertical force, pin diameter, shoulder diameter, and pitch angle) have a relationship with the torque evolution during AA5083 and AA6082 joints [24]. Tool rotation speed and plate thickness have a direct impact, whereas base material properties show an indirect effect on the torque results. The torque results were susceptible to varied axial loads and less sensitive to shoulder diameter. The tool geometry (conical and scrolled shoulder) at different tool rotation speeds, travel speeds, tool tilt angle, and plunge depth had an effect on material flow patterns of 1 mm thick AA 5182-H111-AA 6016-T4 joints. The conical shoulder tool resulted in an excellent appearance with thickness reduction compared with the scrolled shoulder [25]. Using a scrolled shoulder led to the transfer of bulk material from the advancing side toward the retreating side, resulting in inhomogeneous properties in the weldments. Morphological analysis performed at different weld zones is analyzed with dependent relationships with temperature, welding conditions, and residual stresses [26]. Therefore, studying and monitoring the variables that influence weld quality by applying different experimental, numerical, and analytical tools is essential. A comprehensive review was carried out by Kalita et al. [27] on the finite element model (FEM), predictive modeling, and optimization of inert metal gas (MIG), tungsten inert gas (TIG), and FSW. The authors concluded that the design of experiments (DOE) is an effective technique that reduces experimental trials and derives empirical prediction equations [27].

The advanced applications of friction stir techniques in utilizing metals and nonmetals by using fundamental principles concerning parametric optimization, energy generation, the evolution of microstructure (by analyzing temperature distribution and understanding the plastic materials flow), and their influence on mechanical properties of friction stir spot welded (hybrid combination of FSW and the resistance spot welding technique) joints are discussed in Shen et al. [28]. A good weld joint is necessary for achieving better properties. Ogunsemi et al. [29] conducted a study on strategies to improve the joint quality of AA6061-T6. The review focused on methods used for tool design, pre- and post-heat treatments, and grooves incorporated for deploying reinforcement particles that affect the joint properties, which are discussed in detail [1,21]. The detailed review report highlighted the importance of optimizing parameters that could alter the microstructure in attaining superplasticity in alloys [1,21,27,29]. The modification to the FSW technique (i.e., welding underwater) to minimize the peak temperature, which adversely affects the properties of the welded joints, is discussed by Mofid et al. [30]. They concluded the importance of widening the applications that ensure success in dissimilar materials welding, developing an analytical relationship between heat generation and properties evaluation. Previous review reports on friction stir welding proposed that optimizing the process parameters is essential in producing high-quality joints [1,2,8,19–27,31]. Not many efforts have been explored on methodologies applied for cost-effective optimization and their advanced technologies available in online and offline process monitoring.

FSW of steel for researchers and industrialists is always a challenging global task. This occurs due to inadequate transverse speed, which requires highly durable tools to withstand steel's high-temperature and hot-hardness properties. Pure tungsten and polycrystalline cubic boron nitride (PCBN) tools possess the properties mentioned above, compromising high tooling cost resulting in high cost of welding. Thorough analysis and possible solutions for welding steels are discussed in the published literature [1]. Steel-based tool material produces FSW of Al and Mg joints (lap and butt) [2]. Tool materials affect the processing cost, and tool profiles significantly impact process dynamics. FSW uses tool profiles including cylindrical, tapered threaded, pentagonal, hexagonal, and triangular shapes for better joint strength. In 2006, a US-patented convex tool profile was used to fabricate the welded joint [32]. The tool pin profile determines the flow of plasticized material from the leading edge to the trailing edge. FSW tools possessing different tool probes and shoulder geometry, tool dimensions, tool material, and tool wear affect mechanical and microstructural properties [19]. Tool profiles significantly affect the quality and strength of welded specimens. The impact of tool pin profiles on the mechanical characteristics of aluminum alloys is discussed in various publications [19,33]. Tools with a squared profile produce better properties than pentagonal and hexagonal profiles [34]. The threaded cylindrical profile is the preferred tool profile, and process parameters directly affect the weld quality.

The rotational speed (RS), traverse speed (TS), axial force, tool profile, and tilt angle influence the FSW process. The RS determines the stir action of the tool that allows the mixing of the material surrounding the tool, while the TS determines the completion of the weld moving from one side to another [35]. High RS generates a large amount of heat transferred from the tool to the tool–material interface. Friction at the interface increases with RS and is the prominent factor determining the welded strength. The tool pin's height determines the weld's plunge depth (PD). Excess penetration creates a flash at the welded joint. RS is considered the most crucial parameter, followed by TS. Therefore, the selection of optimal values is an important criterion to consider. Optimization techniques have proven to be effective, resulting in a realistic representation of the models developed to determine appropriate process variables. Optimization techniques are classified into statistical and AI tools. Statistical tools are experimental and analysis tools such as Taguchi, response surface methodology (RSM), and factorial design (FD).

In contrast, AI tools are artificial neural networks (ANNs), machine learning (ML) algorithms, fuzzy logic (FL), and so on. The Taguchi method is a widely accepted tool to perform modeling and conduct analysis amongst the statistical tools, whereas ANNs were applied for prediction and optimization under AI tools. Recently, hybridization of statistical and AI tools, namely, Taguchi-ANN, RSM-ANN, RSM-PSO, and so on, are widely practiced in performing optimization. Though much research has been reported on the FSW process, many potential areas still require significant attention to improve the weld properties of butt, lap, and T joints [36]. Many AI tools are applied to perform offline optimization of weld properties, but online monitoring and control possess significant benefits and require significant attention.

Process measurement or in situ monitoring is a way of collecting feedback during the process by using sensors. Many researchers have used process measurement along with multi-objective optimization techniques. Process measurement is a closed-loop system that helps regulate and improve the process. The selection of an appropriate sensor depends on the parameter to be measured. This is followed by effectively placing the sensor in the system, acquiring and analyzing the data, and arriving at substantial conclusions. In FSW, temperature, force, torque, vibration, and acoustic measurement require significant attention. FSW can usually be applied in force or position control. The compressive force and frictional contact at the tool interface generate a measurable quantity of force. These are measured using strain gauges and piezoelectric dynamometers. The in-situ monitoring of FSW machines is reported in the published literature [37].

The Industrial Revolution's development changed manufacturing aspects into a new era of technological innovation. Industry 5.0 comes with a fresh approach to solving problems like pollution and carbon emissions and emphasizes sustainability. Industry 5.0 involves human and autonomous machine collaboration. This motivates cyber–physical systems (CPSs) to become cyber–physical human systems (CPHSs). DT is a strategy for a real-time, digital, and precise replica of the manufacturing process. It has two worlds: the digital world and the natural world. The virtual world comprises digital tools for modeling and simulation, while the real world transposes these virtual tools into hardware models and virtual representations of the real world with remote monitoring.

The primary objective of this review is to lay out the work completed by scholars in the field of optimization and process monitoring with different materials. This work showcases an exhaustive summary of the work and points to research gaps that can be delved into in the future. Readers will acquire good knowledge of optimization and process monitoring. This paper will also act as a guide for anyone who wants to research FSW. This paper discusses the basic underlying principle of the process, process parameters, microstructural studies, and machines, which will give readers insight into the field of FSW. Different optimization techniques and their implementation in the FSW process are discussed. The advantages and limitations of major experimental modeling and optimization techniques useful for practical applications are discussed in detail. Process measurement during welding, the application and effective placement of sensors, and data acquisition tools are also highlighted. Figure 1 shows a schematic representation of optimization and process measurement in the FSW process. This article is divided into four sections: Section 2 explains the working principle, process parameters, microstructural studies, and the FSW machine's advantages and limitations. Section 3 discusses optimization techniques, which include statistical and AI tools. Section 4 focuses on process measurement of the FSW process using sensors and relevant theories associated with them. Section 5 briefly introduces Industry 5.0 and the digital twin (DT) technology framework. Section 6 concludes this paper and lists the research gaps that can be carried out in the future.

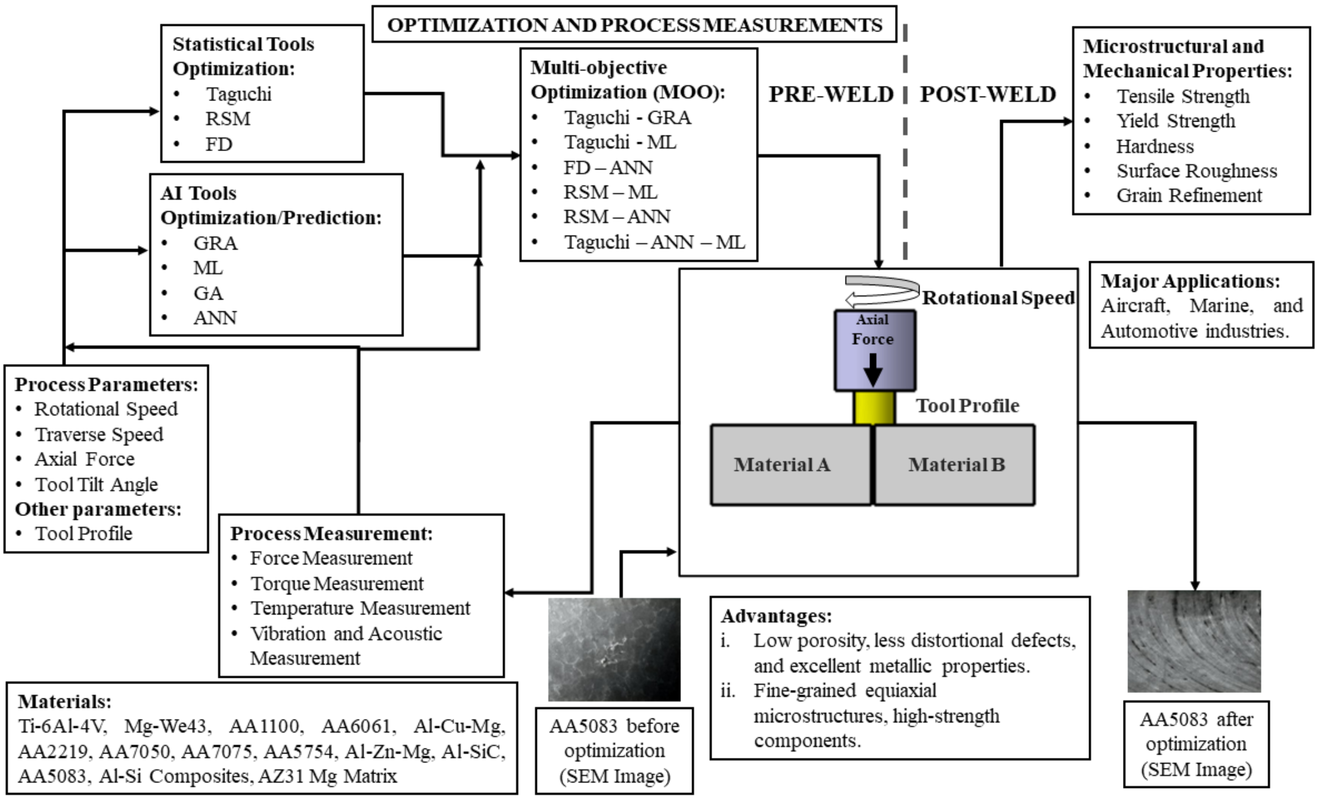

Figure 1. Schematic representation of optimization and process measurements of the FSW process.

2. Friction Stir Welding (FSW)

2.1. Process Description

In FSW, a non-consumable rotating cylindrical tool is placed between two materials and moved along the interface at a predetermined speed (welding or TS). The RS and axial forces operating along the tool axis cause friction at the interface between the tool pin and the material. The heat produced by friction causes the materials to become plastically softened, and mechanical mixing also occurs. After that, the tool is moved along the joint between the two materials, creating a solid weld [38]. Forging and extrusion produce axial force at the shoulder and material interface. From the front to the back, the soft substance moves. Figure 2 depicts the process schematics. Materials A and B may be similar or distinct from one another.

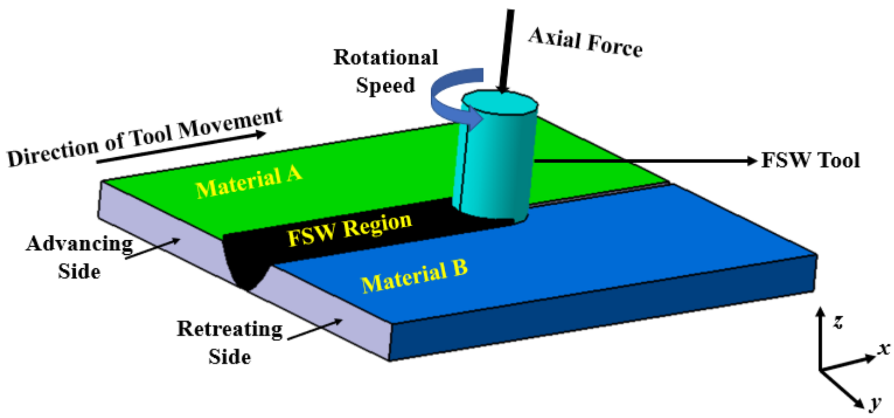

Figure 2. FSW process with a cylindrical tool when the tool is in motion. AS and RS depict the advancing and retreating sides (redrawn from [39]).

The tool RS, traverse speed, axial force, tool tilt angle, and tool geometrical parameters (shoulder and pin profile) affect the weld quality. Several studies have improved these parameters by optimizing the methods that produce joints possessing superior mechanical and microstructural characteristics [40].

FSW takes place in four stages, with the different steps explained in Figure 3:

- Plunge: the non-consumable tool thrusts into the workpiece at a specific RS up to a certain depth.
- Dwell: the tool stays in that position for some time.
- Traverse: The tool advances along the path at a specific speed.
- Tool Retract: the tool comes back from the BM to a certain height.

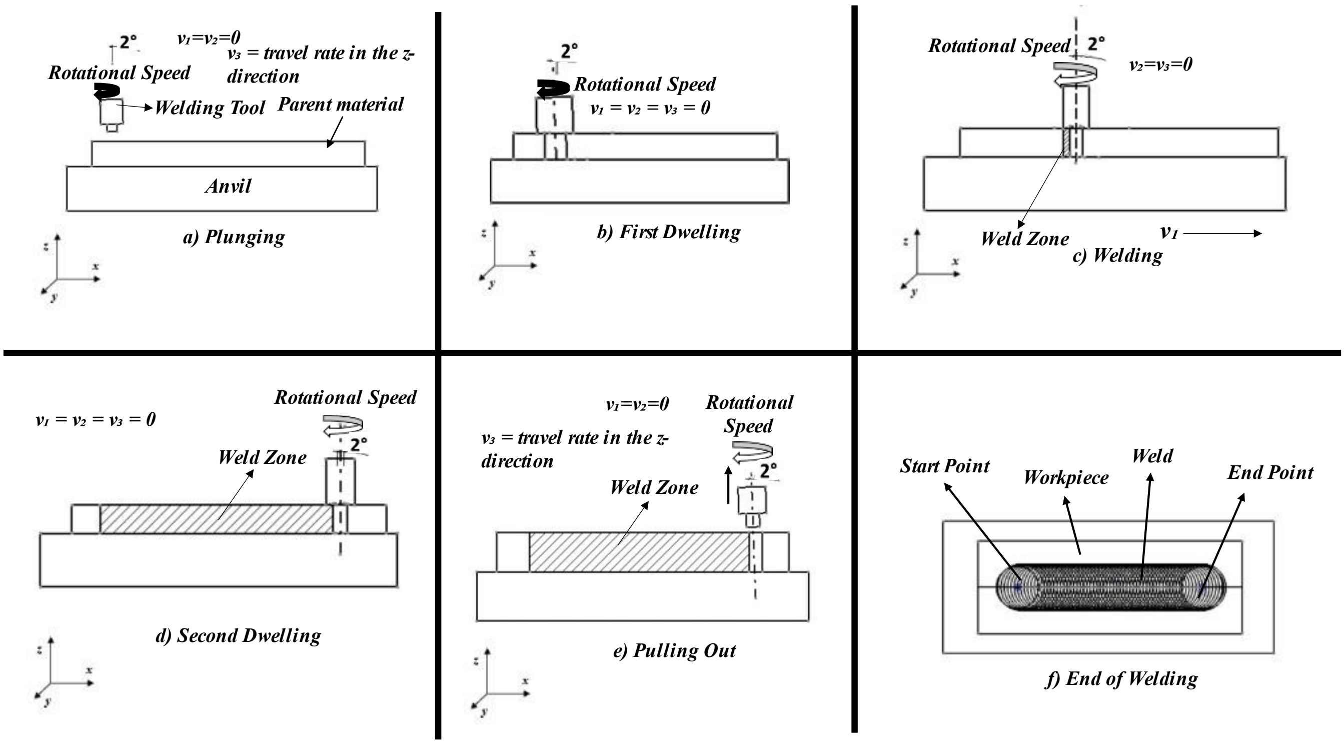

Figure 3. Step-by-step process of the FSW process. v1 = v2 = v3 = travel rate in the x, y, z directions [41].

FSW is used for the butt and lap joints. An increase in the tensile strength of the joint was observed by adding impurity materials like Cu, Zn, and brass as coating materials. The butt and lap joints were used for similar and dissimilar materials [21]. Dressler et al. [42] welded a butt joint composed of Ti-6Al-4V and AA2024-T3. The tensile strength of the joint was 73% of AA2024-T3 base metal. Referring to the work [43], Li et al. modified the existing butt joint for good formability of the Al-Ti joint. The majority of FSW studies were conducted in the butt joint. A hooking defect occurs when the upward flow of the material on the advancing side of SZ behind the tool moves the material upward and some portion remains un-welded, forming a hook. Hook joints are more prominent in the lap joint configuration and can occur in the advancing or retreating side of the joint. Albannai et al. [44] discussed different joints and preventive measures to reduce defect formation in detail. Mao et al. [45] studied the effect of process parameters on hook formation, microstructure, and fracture strength in the lap joint configuration of Al-Mg alloy. Wang et al. [46] explained the tool tilting mechanism's complete insight to suppress FSW void defects. Readers can also refer to the work of Lunetto et al. [47] for eliminating hook joints in similar and dissimilar lap FSW of Al-Mg joints.

2.1.1. Process Parameters

The RS, TS, depth of insertion into the material surface, and tilt angle are the major parameters affecting joint quality. High RS implies high heat generation [1,19,21]. The tool RS creates a frictional localized heat between the tool and the workpiece [48]. High TS or traverse speed leads to a fast procedure and the formation of defects [49]. Table 1 shows the different materials and their composites welded through the FSW process. Tool RS is related to the quantity of the weld, while traverse speed relates to the quality of the weld. As friction between the tool and the workpiece governs heating, a higher rotational speed is desired to mix the materials better. A high RS generates a large amount of heat that is transferred from the tool to the tool–material interface. When traversed at a slow speed along the weld line, the high amount of heat results in better quantity and quality of weld. This refers to the rate of cooling taking place during welding. Apart from the parameters mentioned above, tool design variables like tool shape, material, size, and surface features also play a pivotal role. Threaded, tapered, conical, square, pedal, and cylinder with threaded pin profiles are commonly used for friction stir welding [50,51]. A threaded profile is the most preferred for FSW [51]. Figure 4 showcases different FSW tool profiles. Axial force is a major process parameter that generates friction between the tool and the workpiece. A constant axial force is essential to generate friction and avoid surface voids and wormhole formation during welding, which requires a force controller in the process [52]. Tool force control generates better quality and strength weld joints [53]. Apart from the axial force, travel force and torque control are also necessary. Travel force results from the material's resistance to tool travel along the weld joint line. Controlling travel force can reduce defects like wormhole generation [54]. Torque is the consequence of friction between the tool and the workpiece and is related to the heat input in the system. High friction and a wide contact area require more torque. The motor driving tool must have sufficient torque to ensure a steady tool rotation [55].

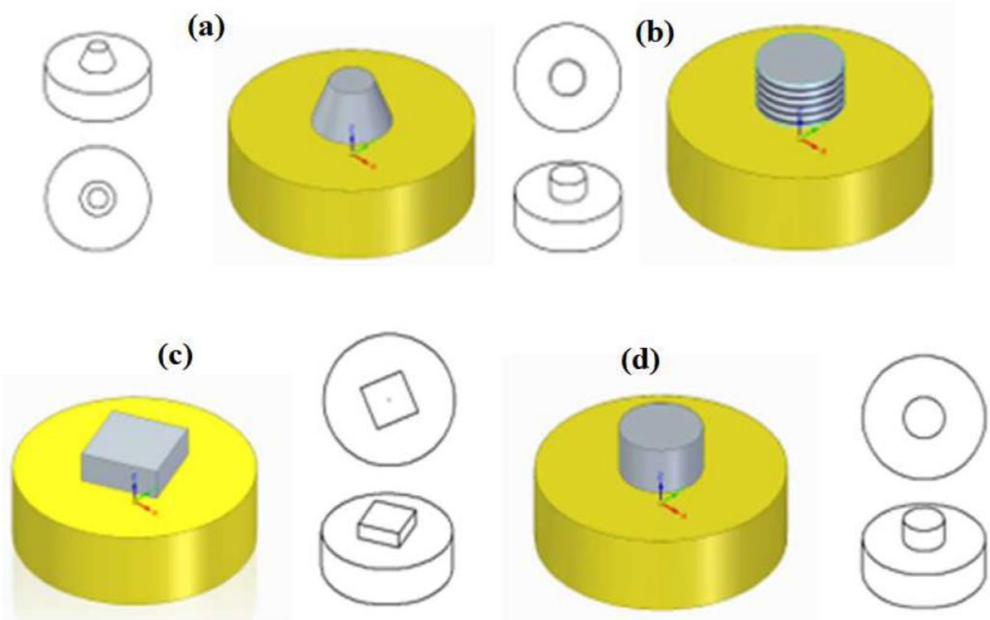

Figure 4. Tool profiles: (**a**) conical, (**b**) threaded, (**c**) square, and (**d**) cylindrical [21].

Effect of Process Parameters

Various studies have been carried out to determine the effect of process parameters on mechanical and microstructural properties. As mentioned above, proper mixing of materials is essential for a sound joint. A high RS results in adequate heat generation and proper mixing of materials. Based on studies in the literature, it was observed that high RS leads to softer plasticization of the material, turbulent material flow, and coarse grains in the NZ. It was also observed that with an increase in RS, the UTS of the joint increases to a certain value, and a further increase in RS decreases the UTS. At high TS, insufficient stirring occurs, and the material does not flow enough from advancing to the retreating side. The UTS, percentage elongation, and hardness decrease with increased TS. This is attributed to insufficient cooling of plasticized material, reducing the softened area. Though limited data are available regarding axial force, the material flow pattern depends on the axial force. A lower axial force results in tunnel defects at the bottom of the weld zone, and a higher axial force results in flash on either side of the weld. Axial force is also responsible for the plunge depth of the pin and plays an important role in propelling plasticized material to complete the extrusion process in the weld zone. A lower tilt angle results in improper material flow, leading to a bell-shaped nugget at the lower part of the weld zone, while a high tilt angle leads to an increase in heat generation. Readers can refer to the brief review report on FSW by [56].

2.1.2. FSW Modelling

Noreña et al. [57] proposed a model consisting of a set of algebraic equations showing how mass and energy in terms of power consumption are transformed along the process to predict the soundness of the joint. This model was developed for conducting the welding process on non-dedicated FSW machines. To solve the problem of varying axial forces due to improper clamping and deformation of back support, Zhao et al. [58] developed an axial force controller with time delay compensation. The controller was developed based on the linear–quadratic regulator (LQR) technique. Teng et al. [59] predicted axial force for the welding of AA2219. A model was developed using the ABAQUS/CEL model to predict the axial force. The authors observed an error of 12.9% between the simulated model and the experimental result.

Rabe et al. [60] considered external and internal process disturbances caused by the workpiece, gap tolerance, tool wear, and fixed parameters to develop a novel force feedback controller. The developed monitoring system precisely differentiated between good quality welds and welds with internal and external defects. Guan et al. [61] used machine learning, and Rabe et al. [62] used a deep learning approach to determine weld quality based on force characteristics during welding. Karlsoon et al. [63] used an industrial robot to develop a closed-loop control system for seam-tracking and force control during welding. The welds formed were defect-free, proving robots can be used effectively to conduct the welding process. Xiao et al. [64] developed a constant plunge depth control strategy for robotic FSW. From the above literature review, the appropriate choice of process parameters and their optimal values with suitable modeling (experimental, numerical, and analytical) tools and techniques resulted in better welded joint quality.

2.1.3. Microstructure

An analytical model was proposed considering several assumptions (based on sliding, sticking, and partial sliding/sticking contact conditions between the rotating tool surface and welding specimen) on heat generation corresponding to material characteristics [65]. A cylindrical probe and conical shoulder made up the tool configuration. The plunge force and experimental torque results were identified to establish the contact condition. The observations revealed a relationship between plunge force and heat generation in a sliding state. The interface between the tool and matrix had sticking contacts.

Song et al. [66] proposed a 3-dimensional heat transfer model corresponding to the dynamic coordinate system. The heat produced by the tool pin and shoulder was considered in the control equation to define the heat transfer control equation for the welding stage of the process, which occurs while the tool is moving at a constant speed along the weld joint line. Initial and boundary conditions were defined, and the heat flux was adjusted to zero to maintain the measured temperature below the material melting temperature. Longer preheat times increased the specimen's initial temperature in front of the tool pin, reducing material yield stress, making welding easier, and protecting the tool from being worn out.

Tool–material contact produces heat and deformation of the material. Heat increases the dislocation density by raising the possibility of dislocation rearrangement and deformation, resulting in refined equiaxed grains at the NZ [1,2,19,21,65].

A post-weld heat treatment (PWHT) factor analysis (temperature range of 200–400 °C for 1 and 4 hrs, speed of 950 rpm, axial force of 2.3 kN, and tilt angle of 1°) was conducted for a threaded conic tool on the microstructure and corrosion behavior at the NZ of AZ31 Mg alloy sheets [67]. The grain sizes of 470 μm and 776 μm after 1 hr and 4 hr holding time corresponded to the temperature range of 300–350 °C. Corrosion resistance increased with a decrease in grain size. The agglomeration of $Al_{11}Mn_4$ intermetallic compounds around Al_8Mn_5 particles increased the PWHT temperature and holding time. At 300 °C for 1 hr, PWHT showed maximum corrosion resistance. Experiments were conducted on plasma-assisted FSW (PA-FSW) of DH36 steel with a WC-10%Co tool to determine the effect on tool life and weld quality to provide solutions related to high tooling cost and shortened tool life [68]. Four specimens were prepared with tapered tool pin profiles operating at RS of 600 rpm, 60 mm/min TS, 13, 15, 17 A preheating current, and 20.5 V voltage. A K-type thermocouple was used to monitor the temperature evolution, and strain gauge-type force sensors were used for force measurements. All the welds from PA-FSW showed no volumetric defects. An increase in preheating current increased the peak temperature generated during welding. Microstructural studies revealed refined grains and ferrite phases. The yield strength and UTS were higher in all the welds. A 31% reduction in the tool force and a 58% reduction in tool wear were observed due to plasma preheating. This was due to material softening.

The microstructure of BM and NZ of FSW A 5052-O alloy is presented in Figure 5 [69]. In that work, an investigation of 3 mm thick AA5052-O plates was performed. The experiment was conducted at RS: 800, 1000, 1500, 2000, and 3000 rpm and constant TS: 120 mm/min. The authors observed a smooth surface morphology at high RS. In the NZ, a fine, recrystallized, and equiaxed microstructure was seen. Mg_2Al_3 particles were significantly broken and heterogeneously distributed in the α(Al) matrix. This was due to the redistribution of several particles within the SZ. These particles were found to negatively impact the tensile strength. The effect of rotation speed was important to obtain the desired microstructure in the welded joint. In another study, the finite element and Eulerian–Lagrangian hybridized methods were applied to develop 3-dimensional thermomechanical studies to obtain the desired shape and analyze the defects produced during the welding process of dissimilar materials (AA2024-T3 and AA6061-T6) [70]. The operating conditions of RS (550, 950, 1500 rpm), TS (40, 60, 80 mm/min), pin profiles (triangular, cylindrical, and cylindrical threaded), and tool tilt angle (1°, 2°, 3°) were varied and the weld quality was evaluated (defects: porosity, inclusions, cracks, and voids) using radiography inspection. The radiographic images were compared with the finite element results and developed the interaction between Lagrangian and Eulerian zones (AS of AA2024-T3 alloy, RS of AA6061-T6 alloy, and void zone wherein flash was visualized) during welding. The Lagrangian model's deformed mesh was translated to the Eulerian model (used 65,000 elements to mesh the part), and the transmitted material volume was computed. The welded joint found fewer defects at TS of 40 mm/min, whereas a higher effective strain rate was observed on the AA6061-T6 side than on the AA2024-T3 side.

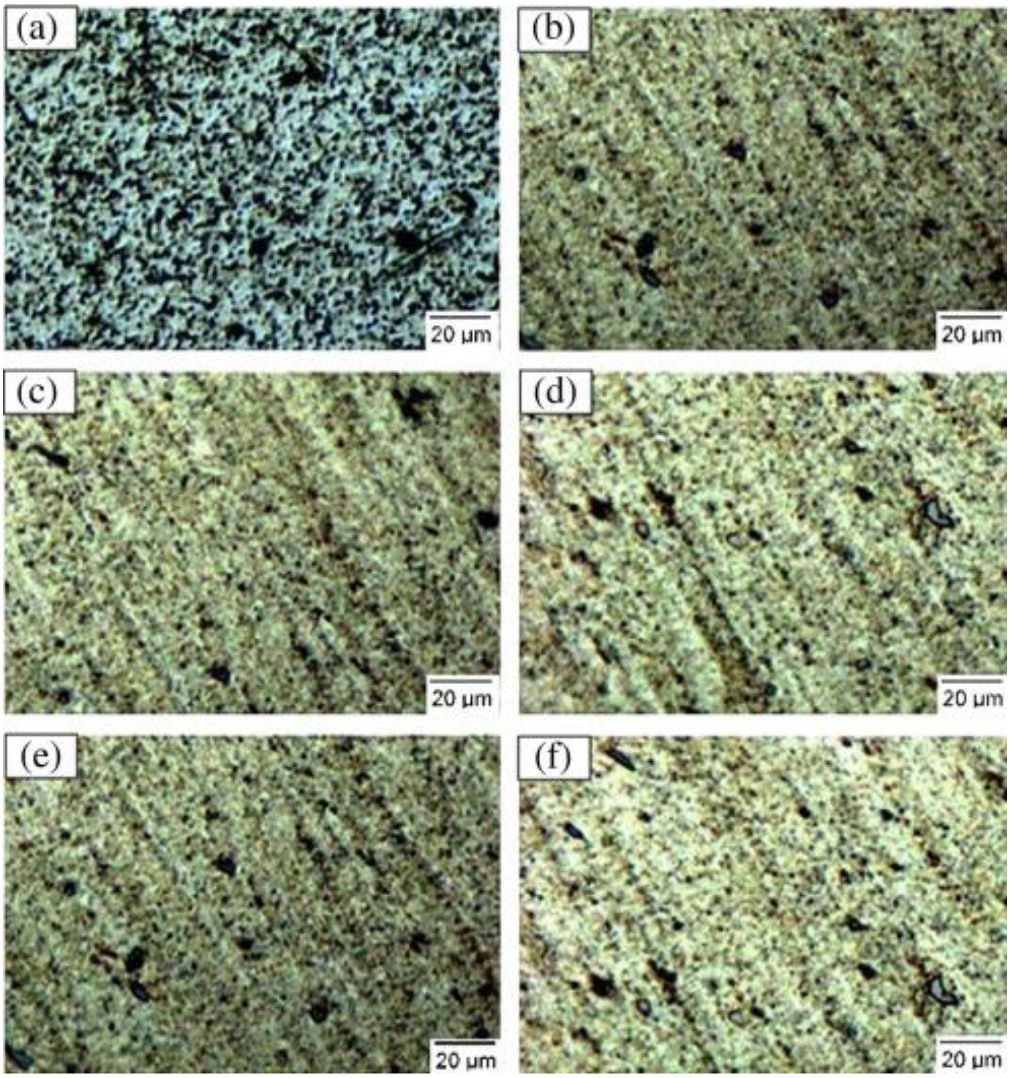

Figure 5. Microstructure of BM and NZ of FSW A 5052-O alloy: (**a**) base metal RS at (**b**) 800 rpm, (**c**) 1000 rpm, (**d**) 1500 rpm, (**e**) 2000 rpm, and (**f**) 3000 rpm, TS: 120 mm/min (constant). Fine, equiaxed, recrystallized grains can be seen in all microstructures [69].

2.1.4. Materials (Alloys and Composites)

FSW was applied successfully to join similar and dissimilar aluminum alloys and later extended to composites. Table 1 shows the work performed in FSW of alloys and composites during the past few years. Table 2 shows the work performed in dissimilar joints during the past few years. FSW can be applied to nickel–titanium shape memory alloys (SMAs) without causing any impact to the transformation temperature [71]. The method of joining steel to aluminum have limitations such as limited weldability, formation of pores, intermetallic oxide inclusions, and hot cracks [72]. FSW has been proven to overcome these limitations [2]. Experiments were conducted using a tungsten–rhenium tool with a different set of factors (with varying rotational speed (350, 400, 450 rpm) and maintaining a TS, dwell period, and tilt angle of 75 mm/min, 30 s, and 2.5°, respectively), which evaluated the mechanical, microstructure, corrosion behavior of parts. A grain size of 20.4 ± 1.8 µm was observed at the stir zone at 400 rpm. The joint efficiency was kept at a room temperature of 93% and an elevated temperature of 84%. At room temperature (martensite phase), tensile loading showed that the material had more strain hardening than the BM. At 125 °C (austenite phase), the alloy showed an elastoplastic tensile response, and no super elasticity was observed. At elevated ambient temperatures, microcracks perpendicular to tensile loading were observed in the stir zone. Figure 6 shows the microstructure of welded specimens under optical microscopy.

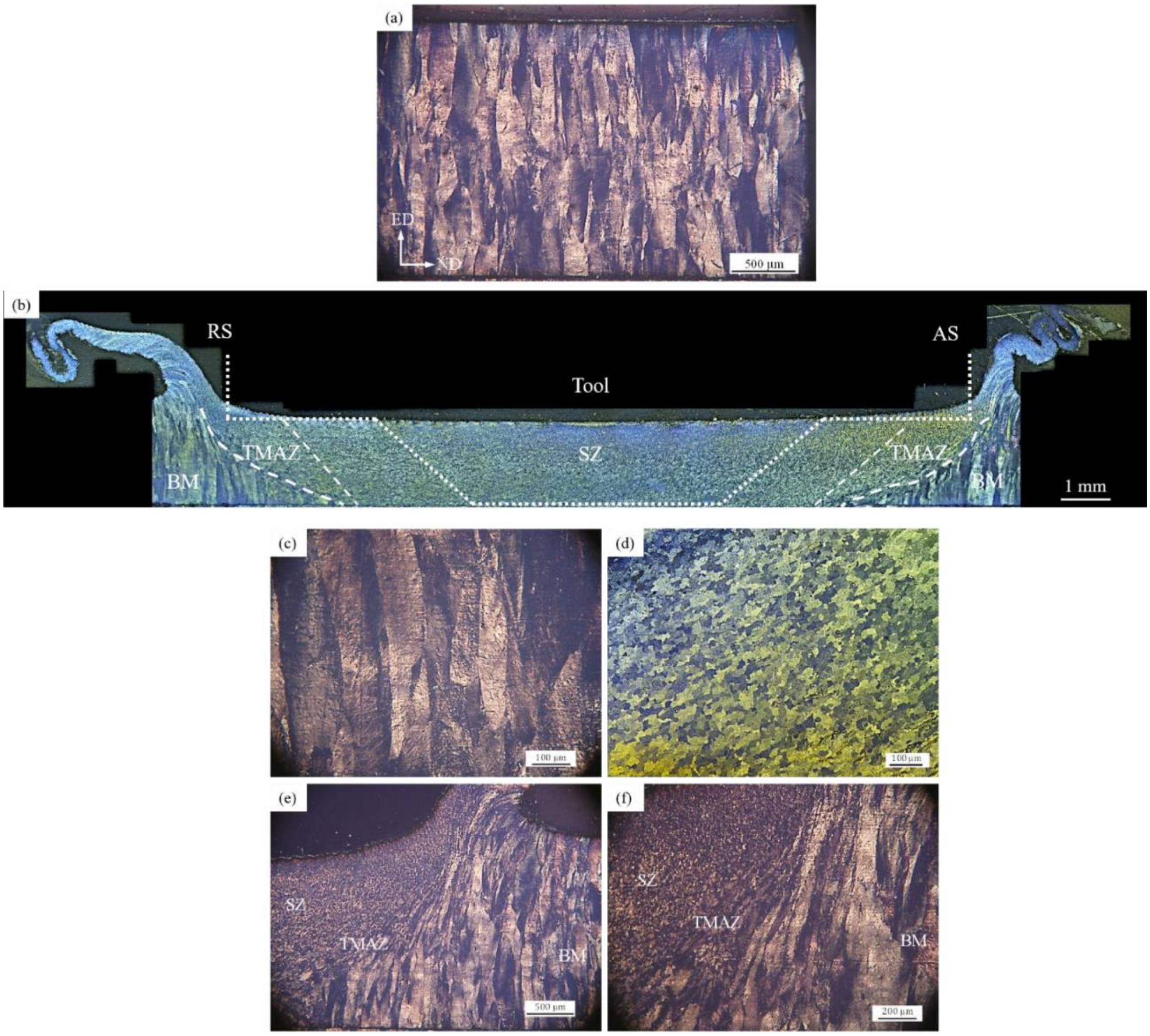

Figure 6. (**a**) Optical microscopy tests of the BM: (**b**) different zones of welded specimen at 400 rpm and (**c**–**f**) optical microscopy image of the BM, stir zone, and SZ-TMAZ-BM interface [71].

2.1.5. FSW Machines

Three types of machines are utilized for FSW, as stated in the literature:

- Conventional milling machines.
- Custom-made FSW machines.
- Specialized robots designed for FSW.

Researchers have used conventional milling machines to perform friction stir welding. This is because milling machines have a rotating tool, which is an essential requirement. Milling machines have high stiffness and low capacity to produce complex welds. This needs structural enhancements to withstand high axial loads. Apart from milling machines, there are custom-made FSW machines available. These machines have high stiffness but are very expensive. These customized machines are used for metals like aluminum, titanium, steel, and nickel. The third category is specialized robots. These machines have limited applications, but the significant advantage is the feasibility of three-dimensional welding.

Mendes et al. [73] surveyed the devices and control systems for FSW using robots and force control. Table 3 shows the comparison of FSW machines.

FSW has been used widely for soft materials, but FSW for high-stress and high-temperature materials like nickel alloys and steel alloys, polycrystalline cubic boron nitride (PCBN) was developed in 1998. Two materials have been found to have met the requirement of FSW of hard materials: refractory metal tools and super abrasive tools. Tungsten is the first refractory tool used in FSW but suffered problems during the plunge because of its ductile-to-brittle transition temperature, leading to wear and fracture resistance. The weld could be done up to 13 mm thick in one pass. Polycrystalline diamond (PCD) and polycrystalline cubic boron nitride (PCBN) are two existing varieties in the super abrasive category. PCD has been used for the processing of aluminum matrix composites, nickel, steel, and titanium alloys [74]. Because of the low coefficient of friction, smooth welding surfaces were found in PCBN because of their high strength and hardness at high temperatures [75]. The evolution of FSW in the recent past has been tremendous, and the focus needs to be on fabricating better parts and designing and developing low-cost FSW machines. Figures 7–9 show different FSW machines.

Table 1. FSW of alloys and composites.

Material	Tool Profile	Tool Material	Ref.
Al-SiC composite sheets	Cylindrical threaded	H-13 steel tool	[49]
Aluminium matrix composite	Cylindrical	M2 steel	[76]
AA6061-4.5Cu-5SiC (Wt.%)	Square	HSS M2	[77]
Cast aluminum 359 + 20% SiC metal–matrix composite	Cylindrical threaded	1/4–20, 01 AlSi oil-hardened	[78]
AA2009/SiCp composite	Cylindrical threaded	Steel	[79]
Aluminum 6092/SiC/25p/t6 metal matrix composite	Cylindrical	H13 tool steel	[80]
2124Al/25vol%SiCp	Cylindrical threaded	H13 steel (48 HRc) and MP159 alloy	[81]
Boron carbide particulate reinforced AA6061	Square profile	High-carbon high-chromium steel	[82]
Aluminium matrix nano-composite	Threaded taper	H13 steel	[83]
TiAl6V4 to AA2024-T3	Threaded taper	Tool steel	[42]
2024 and 7075 Al alloys	Cylindrical threaded	SKD61	[84]
(AMg6, AD1) and steels (St3ps; 12Kh18N10T)	--	--	[2]
Ti-6Al-4V	--	Tungsten carbide	[85]
Ti-6Al-4V	--	Tungsten rhenium	[86]
Ti–1.5Al–1Mn	Conical	As-cast ZhS32 nickel superalloy	[87]
Ti–6Al–4V	--	Tungsten rhenium	[88]
Titanium alloy T-joint	Cylindrical	W-25Re alloy	[89]
AZ31 magnesium alloy	Cylindrical stir	High-speed steel W18Cr4V	[90]
AZ31B magnesium alloy	Straight cylindrical, tapered cylindrical, threaded cylindrical, triangular and square	Mild steel, stainless steel, armour steel, high-carbon steel, high-speed steel	[91]
AZ31 magnesium alloy butt weld	--	65Mn steel	[92]
AZ80A and AZ91C Mg alloys	Cylindrical tapered	M35 high-speed steel	[93]
AZ31B magnesium alloy	Cylindrical threaded	H13 steel	[94]

Table 2. FSW of dissimilar materials.

Material	Tool Profile	Tool Material	Ref.
Al-Cu	Conical	Tool steel	[95]
Ti–6Al–4V to Al–6Mg	Tapered	WC–Co	[43]
AA7075-T651 to Ti-6Al-4V	Threaded taper	---	[96]
Noryl™ GFN2 (Polyphenylene ether (PPE) + high impact polystyrene (HIPS) + 20 wt% of short glass-fiber-reinforced) and AA6082-T6	Cylindrical threaded	Medium-carbon steel	[97]
AA6061-T6 and Ti6Al4V	Cylindrical and tapered	WC with 10% Co	[98]
Pure titanium (CP-Ti) and Ti6Al4V sheets	Truncated conical		[47]
Al 6061-T6 to AISi 316 stainless steel	Cylindrical	WC-Co	[99]
AA1050 and AZ91	Cylindrical	H13 steel	[100]
AA6061-T6 and pure Cu	Cylindrical	---	[101]
Pure Al–pure Cu	Cylindrical, tapered, straight triangle, and straight square	W302 steel	[102]
Galvanized steel (GS) and mild steel Q235	Conical tapered	WC	[103]
AZ31-AM60	--	Tool steel	[104]

Table 3. FSW machines and characteristics [105].

Characteristics	FSW Processing Machines			
	Milling Machine	Customized Machine	Parallel Robot	Articulated Robot
Capital investment	Low	High	High	Low
Stiffness	High	High	High	Low
Flexibility	Low	Medium	High	High
Setup Time	Low	High	Medium	Medium
Complex welds profiles	Low	Medium	High	High

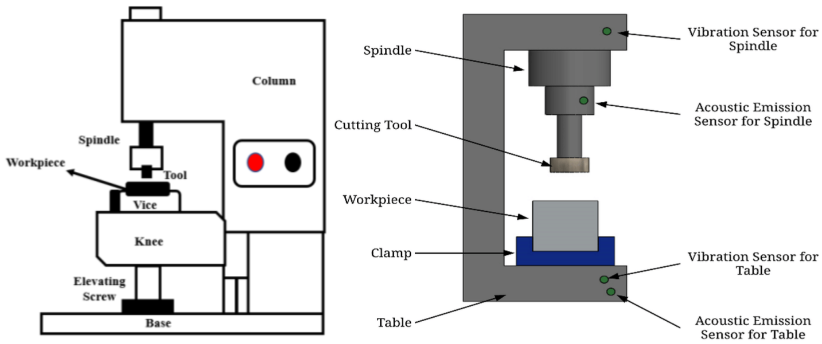

Figure 7. Vertical milling machine (redrawn from [106]).

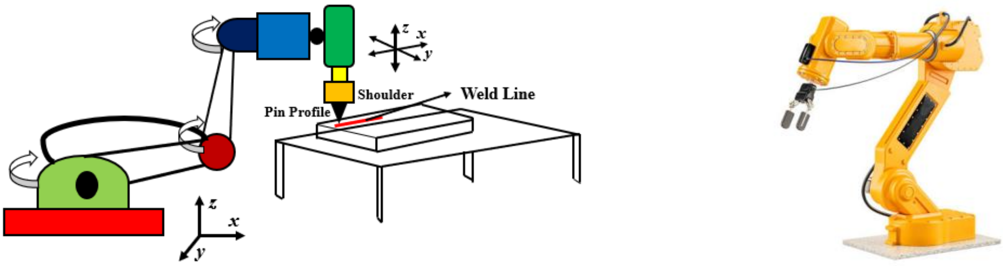

Figure 8. Robotic FSW (redrawn from [107]).

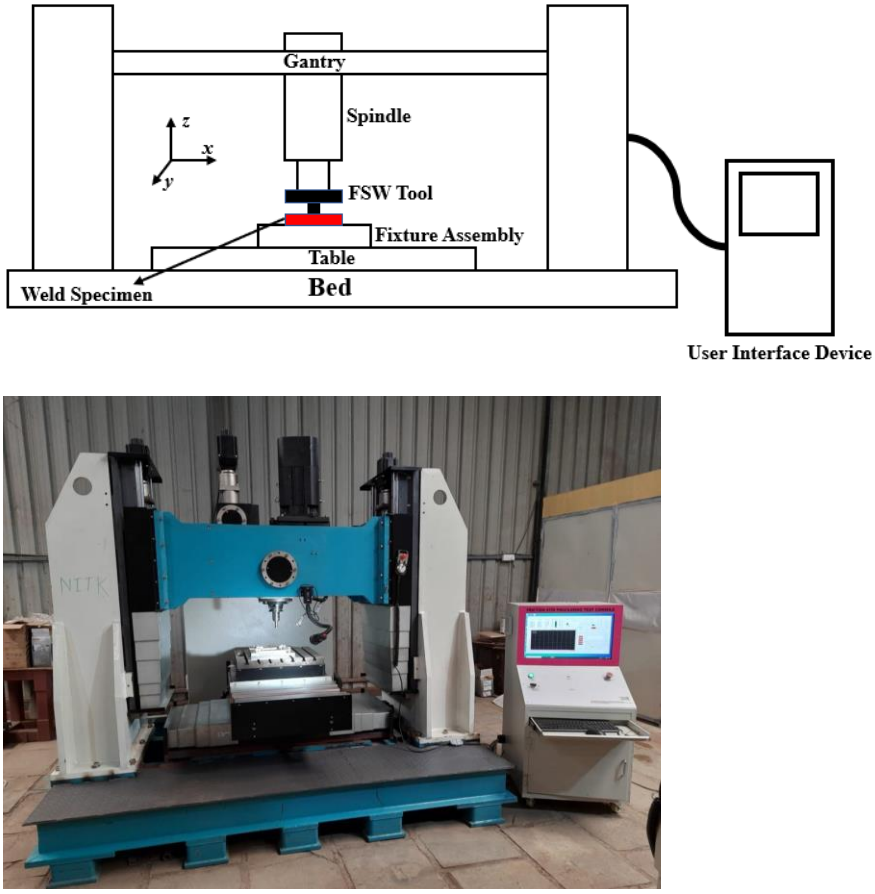

Figure 9. FSW machine (gantry type).

2.2. Summary

The following observations are made by highlighting the major points.

- Tool RS is related to heat generation, while TS relates to heat supply to the weld region.
- For friction stir welding involving a tool pin, a threaded pin profile is preferred because threads allow the proper flow of material from the shoulder down to the bottom of the pin.
- Preheating the tool pin is advisable to reduce yield stress to prevent wear out of the tool. This makes welding easier.
- Conventional milling machines with structural enhancements to withstand heavy loads can be used for FSW.
- NZ has a higher strength due to fine, equiaxed grain structure formation.
- It was also observed that with an increase in RS, tensile strength increased to a specific value and then decreased with a further rise in RS.

- A decrease in heat input led to a reduction in workpiece temperature and increased vertical force due to welding speed.
- Higher values of RS, TS, and penetration depth and a lower tilt angle are required to enhance joint efficiency and increase microhardness.

The above points depict that the process parameter strongly influences the joint properties, and therefore, optimization plays a vital role.

3. Optimization

Optimization algorithms, an embedded part of an optimization process, are numerical simulators where a realistic representation of physical models that need to be optimized is performed. One way of classifying algorithms is as being deterministic or stochastic. Deterministic algorithms respond in a set of defined rules without any randomness in their nature (i.e., actual output for some definite input), while in the case of stochastic, there is randomness in the output. For some definite input, the algorithm can give multiple outputs. Including randomness at every stage of the algorithm is called heuristics or, in some cases, metaheuristics [108]. This section discusses the various optimization techniques used so far in FSW. Figure 10 showcases different combinations that can be made possible for performing optimization.

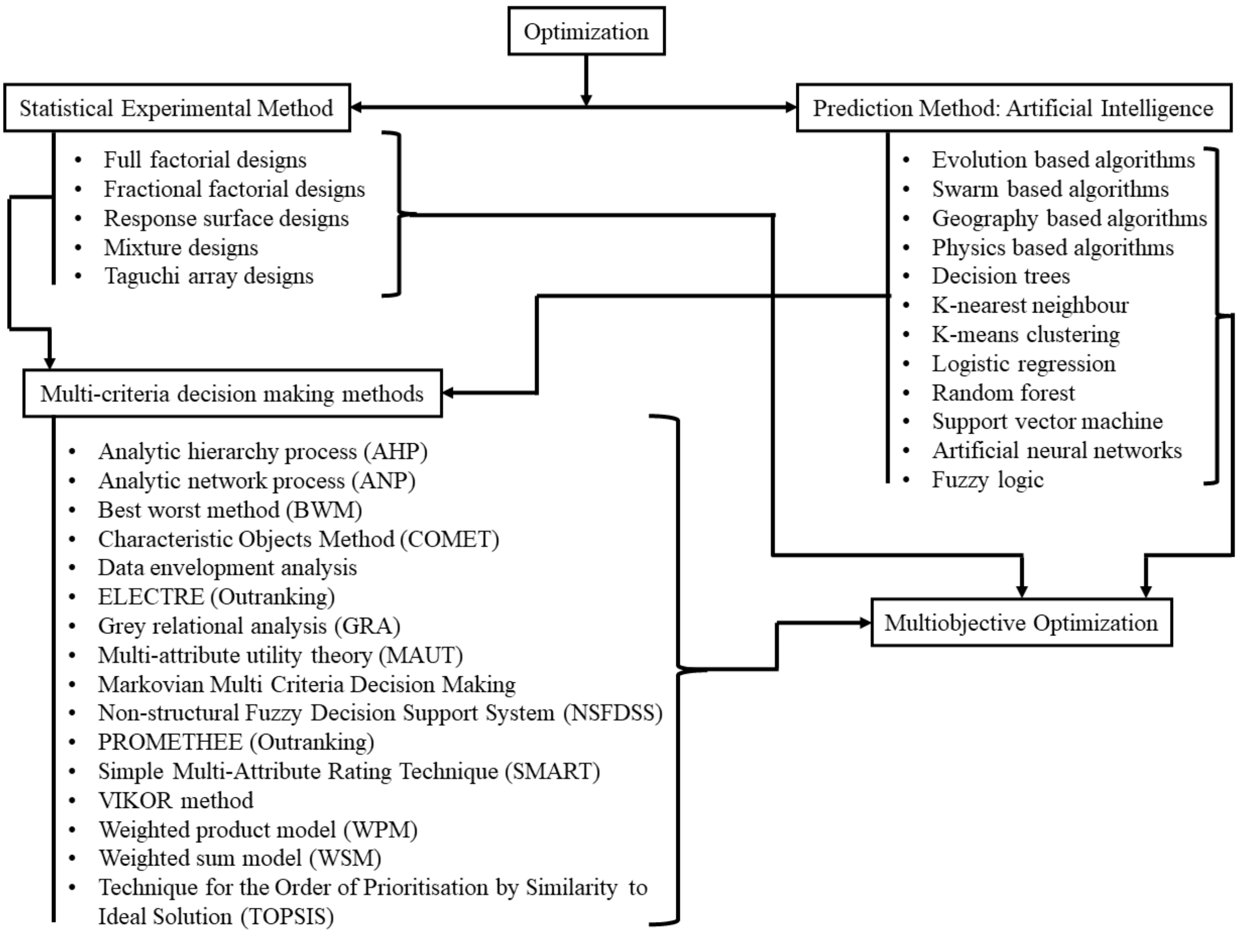

Figure 10. Different combinations that can be made possible for performing optimization.

3.1. Statistical Tools

3.1.1. Taguchi Optimization

Taguchi is a statistical method used to improve the quality of manufactured products. Dr. Genichi Taguchi developed it in 1978. He framed plans using experimentation called design of experiments (DoE) to make robust systems [109]. There are eight steps involved in Taguchi optimization:

- Determine the primary function of any process.
- To find various noise factors, test conditions, and quality characteristics.
- Define the objective function.
- Categorize different elements and provide value to them.
- Select the correct orthogonal matrix for multiple experiments.
- Experimentation.
- Investigation of data and prediction of optimum level of performance.
- Verification of experiments conducted and plan of future action.

The process parameters selected may affect the joints welded in FSW, material properties, microstructure, and grain refinement. Setting appropriate parameters is an essential step in this regard. Optimization tools help develop inter-relationships among various parameters collected and stored, and analysis is performed [110]. The algorithm gives the optimum or best possible combination of data that can be implemented in any process. Figure 11 shows a flowchart of the Taguchi optimization technique. Korgal et al. [111] studied the grain refinement and tensile strength of AA4032 alloy using Taguchi and ANOVA analysis. The significant advantage of the Taguchi method is that it focuses on the mean performance value rather than the value within certain limits. Narrowing it down to the main process parameter is the easiest method. Taguchi's orthogonal arrays (OAs) require less than 0.3% of the original number of experiments. However, Taguchi's OA does not test various combinations of process parameters, and the method does not consider the dynamic changes in the values. It emphasizes only the offline mode of optimization. It acts as an initial step of process development.

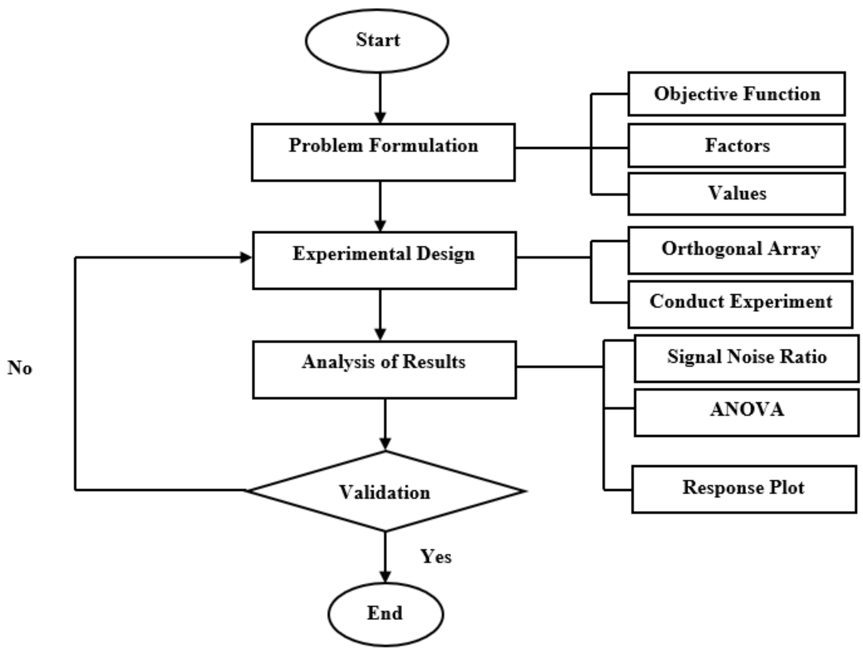

Figure 11. Taguchi optimization flowchart.

Taguchi L_{18} experiments (different sets of RS: 600–1200, pin shape: tapered and non-tapered, TS: 20–35 mm/min, and preheating) were conducted to weld 6 mm thick AA2014 aluminum alloy, AZ31 magnesium alloy, and Al–SiC composite using an alloy steel tool, and the strength of welded joints was analyzed [112]. Tool rotation was the major factor for tensile strength, whereas tool pin shape was insignificant. A tapered HSS tool without threads was used to weld 5 mm thick plates of AA6351 and AA5083 alloys coated with Cu and Zn [113]. The coating thickness had a significant impact on tensile strength. The optimal parameters obtained were 20 mm/min, 1300 rpm, and 50 microns of Cu coating on both sides of the aluminum plate, resulting in 141 to 149.5 MPa.

L_9 experiments were conducted (with varied sets of RS 1000–1600 rpm, traverse speed 3–5 mm/s, and axial force of 5–7 kN) to perform butt welding of AA6063 pipe [114]. The Taguchi method showed 62.75% impact with traverse speed and 50.43% with axial force on the residual stresses formed in the produced joint. Taguchi L_9 experiments with sets of RSs (1000–1400 rpm), feed rates (14–18 mm/min), and tool pin profiles (tapered, threaded, and cylindrical) were planned and used to analyze the performances (tensile strength, hardness, joint efficiency, and microstructure) of AA5451 plates in marine applications [115]. Taguchi optimal parametric combinations possessing a threaded tool profile resulted in better properties. A Taguchi experimental plan with a set of tool RS (710–1400 rpm), TS (16–40 mm/min), and dwell time (8–22 s) possessing an H-13 die steel tool with a cylindrical pin was used to perform Al-Li (AA8090) alloy joints [116]. An increase in TS and dwell time increased the UTS due to less heat flow into the weld zone. An increase in RS showed a steep rise in the hardness, while a decrease in hardness was shown with an increase in TS and dwell time. A microstructural analysis performed using SEM revealed that the density of the grains near the axis weld line improved the strength. Ductile failure was observed in the welded joints, and dimples were observed in welded specimens. The parameter (RS (700–1100 rpm), axial force (1.5–2.5 kN), tilt angle (1–3°), tapered threaded tool profile) optimization of dissimilar butt weld of AA6061 and AA7075 alloy was conducted [117]. Impact strength increased with RS until 100 rpm. An increase in tilt angle increased the impact strength of the weld, which decreased afterward. The effect of pin profiles (triangle, square, and cylindrical) and RS (450–1120 rpm), TS (100–250 mm/min), and tilt angle (1–3°) on the corrosion behavior of AA1080 alloy was studied [118]. It was observed that a pin with a smooth surface led to better corrosion behavior. SEM analysis showed the surface of samples welded using a triangle pin was more corroded. Cylindrical pin samples had more corrosion resistance, and the corrosion rate was higher in triangle pins. This was due to grain size because of the change in the pin profile.

A multi-objective optimization of parameters (shoulder diameter (14, 18 mm), PD (0.0, 0.4 mm), fixture position (30, 90 mm), and tapered profile tool) on the performances (SR, NZ hardness, and UTS) of AA6982-T6 parts were performed using GRA [119]. Increased shoulder diameter increased the surface roughness (SR) but decreased beyond the critical value. An increase in shoulder diameter decreased the UTS and hardness. An increase in PD up to 0.2 mm increased the value of SR, hardness, and UTS, which later decreased. At the fixture position of 60 mm, the highest value of hardness, surface roughness, and tensile strength was observed. GRA showed a maximum weight of the ninth test, resulting in the optimal condition (shoulder diameter was 14 mm, 0.2 mm of PD, 60 mm for the fixture position). Taguchi L_9 experiments (threaded pin profiles: cylindrical, tri-flute, and taper; RS: 900–1400 rpm, and TS (37.5–47.5 mm/min)) and GRA were applied to determine the optimal temperature corresponding to parameters for 5 mm AA6061 alloy butt joint configuration [120]. The k-type thermocouple measured the temperature on both the advancing and retreating sides. The optimal conditions (RS of 1400 rpm, 37.5 mm/min TS, tapered tool pin profile) showed a better tensile strength of 286.8 MPa and 77.96 HRA and a temperature of about 559.9 °C, respectively. Taguchi L_9 experiments with tapered cylindrical cam tri-flute with left-hand threads were used to fabricate AA2519-T87 plates of thickness 15.4 mm with varied parameters including shoulder diameter (23–29 mm), RS (450–710 rpm), TS (31.5–50 mm/min), and the joint efficiency was analyzed [121]. Tunneling defects in weld parts were reduced with decreased RS values. The SZ/TMAZ interface showed a high density of Al_2Cu coarser particles. Some other works using Taguchi optimization are summarized in Table 4. Fine and equiaxed grains are observed, leading to the highest UTS (refer to Figure 12).

Table 4. Other works applying the Taguchi method.

Process Parameters	The Objective of the Work	Ref.
L_9 experiments (three levels) RS: 500,650,800 rp; TS: 115, 135, 155 mm/s; Axial load: 9, 13, 17 kN; Cylindrical tapered column threaded tool	Process optimization of Al-Mg alloy	[123]
L_9 experiments (three levels) RS: 800, 1200, 1600 rpm; Tool tilt angle: 0°, 1°, 2°; TS: 20, 50, 80 mm/min; H13 tool steel with taper cylindrical pin profile	Process optimization of FSW of AA5083 and AA6061	[124]
L_{16} experiments (four levels) RS: 400, 800, 1250, 1600 rpm; TS: 20, 50, 80, 125 mm/min; Pin profile: square, pentagonal, hexagonal, circular; TA: 90°, 108°, 120° and 180° tool internal angle.	Process optimization of friction stir lap welding joint parameters of AA1100 alloy	[125]
L_{27} experiments (four levels) RS: 500, 1000, 1500 rpm; Feed rate: 30, 40, 50 mm/min; Pitch: 1, 2, 3 mm; HCHCr tool with taper threaded profile	Optimizing process parameters of FSW of Nylon 6A	[126]
L_9 experiments (three levels) RS: 910, 1280, 1700 rpm; Pin profile: square, cylindrical, triangle; Joint type: butt, stepped, and scarf	Optimizing FSW process parameters of self-supporting AA6063 pipe joints	[127]
L_{27} experiments (three levels) RS: 800, 950, 1100 rpm; TS: 30, 60, 90 mm/min; Pin profile: square, cylindrical, triangle	Process optimization of dissimilar joints of AA6061-T6 and AA5052-H32 alloy	[128]
L_{16} experiments (four levels) Vibration amplitude: 20–80µm; TS = 40–160 mm/min; RS: 630–1200 rpm	Optimizing ultrasonic-assisted FSW parameters for AA6082-T61 joints	[129]
L_{18} experiments (four levels) RS: 500, 600, 700 rpm; Axial load: 10, 15, 20 kN; Feed rate: 16, 20, 24 mm/min; Tilt angle: 0°, 1.5°	Optimizing mechanical and microstructural behavior of AA7075	[130]
L_{16} experiments (four levels) RS: 400, 630, 1000, 1600 rpm; TS: 10, 25, 40, 63 mm/min; Tool profile: square, cylindrical, triangular, and tapered	Optimization characteristics for AA6061 alloy	[131]
L_{16} experiments (four levels) Applied load: 10, 15, 20 25 N; Sliding velocity: 0.6, 0.8, 1.0, 1.2 mm/s; Sliding distance: 500, 1000, 1500, 2000 mm, cylindrical tool pin profile, RS: 800 rpm, Feed rate: 40 mm/min	Optimizing wear properties for AA6061 and AA7075 alloy	[132]
L_{27} experiments (four levels) RS: 900, 1100, 1400 rpm; TS: 20, 30, 40 mm/min; Tilt angle: 2°, 2.5°, 3°	Optimizing wear properties of AA6262/5456 Joints	[133]
L_9 experiments (four levels) RS: 560, 730, 900 rpm; TS: 60, 80, 100 mm/min; Tool tilt angle: 0°, 1°, 2°; Cylindrical threaded tool	Optimization and analysis of AA5083 alloy joints	[134]
L_9 experiments (four levels) RS: 400, 800, 1200, 1600 rpm; TS: 30, 60, 90, 120 mm/rev; Tilt angle of 1°, 2°, 3°,4° Pin profile: square, pentagonal, hexagonal, and circular	The optimal condition for AA1100 alloy lap joint	[135]
L_9 experiments (three levels) RS: 600 rpm, TS: 200, 400, 600 mm/min; Pin profile: cylindrical, square, and rectangle	Parameter optimization of AA1050 alloy using bobbin tool	[136]
L_{27} experiments for butt joint (three levels) Tilt Angle: 1–3°; RS: 725–1600 rpm; TS: 206–380 mm/min; Probe penetration: 1.95–3.95 mm Shoulder/probe ratio: 3.4–4.4 For T-joint: RS: 520–1600 rpm; TS: 79–400 mm/min; Probe penetration: 4.0–4.2; Shoulder/probe ratio: 3.4–4.6 For lap joint: RS: 830, 1600 rpm, TS: 310 mm/min	Optimizing parameters for high tensile strength in AA6262-T6 parts	[36]
L_{16} experiments (four levels) RS: 900, 1100, 1300, 1500 rpm; TS: 45, 60, 75, 90 mm/min; Tool profiles: tapered, tapered threaded, cylindrical, cylindrical threaded; Preheating temperature: room temperature, 80 °C, 100 °C, 120 °C	Optimizing AA2099-T8 parts to attain maximum tensile strength and reduced tool wear	[137]
L_{27} experiments (three levels) RS = 710, 900, 1120 rpm; TS = 160, 200, 250 mm/mi; Shoulder diameter = 10, 12, 14 mm Threaded cylindrical tool of high-carbon steel	Optimizing welding parameters for AA7475-T651 and AA2219-O joints	[138]

Table 4. *Cont.*

Process Parameters	The Objective of the Work	Ref.
L_9 experiments (three levels) AlSi H13 steel cylindrical probe; RS = 545, 765, 1070 rpm; TS = 20, 31.5, 50 mm/min; Tool tilt angle = 0°, 1°, 2°	Optimization of AA8090 parts quality using Taguchi and GRA	[116]
L_{16} experiments (four levels) RS = 450, 600, 750, 850 rpm; TS = 15, 35, 50, 65 mm/min; Tool profile: straight cylinder, tapered cylinder, cylindrical threaded, tapered threaded; D/d ratio = 2, 2.5, 2.75, 3.	Optimization of FSW of AA2618-T87 and AA5086-H321 plates	[139]
L_{27} experiments (three levels) RS: 500, 700, 900 rpm, TS: 30, 40, 50 mm/min; Axial load: 6, 7, 8 kN; Flattened round tool pin profile.	Taguchi and GRA optimization of the microstructure of AA1100 plates	[140]

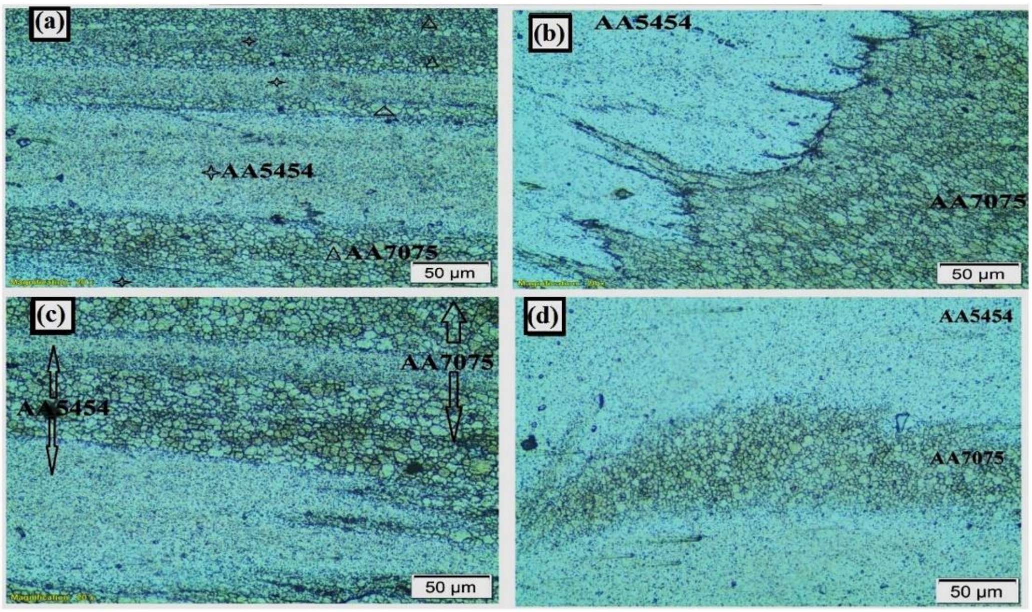

Figure 12. An optical micrograph of FSW of AA5454-AA7075 at optimum parameters of 0.1 mm PD, RS: 1225 rpm, TS: 21 mm/min, tapered pin profile, 2° tilt angle. Fine, equiaxed grains can be observed, which cause the highest UTS. (**a**) upper (**b**,**c**) middle, (**d**) bottom of the weld joint showing good stirring and finer, equiaxed grains in the NZ [122].

The conclusions drawn from the literature review on the use of the Taguchi method are discussed below:

1. The Taguchi matrix design for experimentation resulted in a cost-effective technique for parametric analysis and optimization.
2. Taguchi designed different experimental matrices; therefore, individual matrix selection relies mainly on the investigator's choice. The factors (individual, curvature, and interaction) and levels affecting the responses are to be considered by the investigator during the matrix or orthogonal array selection process.
3. The Taguchi method optimizes only one response at once.
4. The optimal setting for one response might not be true for the other.
5. The optimal condition is different for different materials due to differences in material properties.
6. The factors (RS, TS, axial load, pin profile, shoulder diameter, tool tilt angle, pin material, probe penetration, feed rate, tool vibration, etc.) critically affect the welded joint properties.
7. Most of the literature neglected the interaction factor effects, probably due to reduced experimental trials or matrices selected.

8. Taguchi determines the levels of factors that are the optimal conditions resulting in a local solution.

3.1.2. Advantages and Limitations

The significant advantage of Taguchi's design of experiment is as follows:

1. Taguchi's method focused on the performance value rather than the individual performance limit or range value.
2. The Taguchi method is applied to narrow down the main process parameter (i.e., focused on reducing the process parameters by conducting limited experiments and analyzing the output performance).
3. The Taguchi method enables conducting experimental trials to determine whether individual factors and interaction between process factors are less significant.
4. The Taguchi method ensures studying both continuous and discontinuous responses.

The disadvantages of Taguchi methods are as follows:

1. Taguchi's OA does not test various combinations of process parameters, and the method does not consider the dynamic changes in the values.
2. The Taguchi method can only optimize the process in offline mode.
3. In many applications, the method is applied at the initial process development step.
4. The matrices are limited in number and thus fail to test all factor interactions within the proposed experimental design.
5. The Taguchi method limits the experimental trials and is treated as a one-time improvement technique, resulting in local or sub-optimal solutions.
6. The Taguchi method only derives empirical equations with a mechanistic model, resulting in a local solution.
7. Taguchi's method refers to optimization without developing intrinsic empirical or mechanistic modeling, resulting in improper process insight.
8. The Taguchi method requires the support of alternating optimization methods (say, GRA, TOPSIS, MOORA, AI and ML algorithms, etc.) to optimize multiple outputs simultaneously.
9. The Taguchi method applied for multiple objective optimizations is based on judgmental and subjective methods, resulting in a less efficient model.

Scope of future work: It is combined with other AI-based techniques for more accurate results. This combination is called the multi-objective optimization technique, which is discussed later in this paper.

3.1.3. Response Surface Methodology (RSM)

In 1951, the RSM technique was developed by Box and Wilson to collect data and correlate input–output variables [141]. In other words, it develops a relationship between dependent and independent variables. The relationship is developed using many regression models [142]. It is based on the best-fit empirical model extrapolated from the experimental data [142,143]. The standard form of a regression model is:

$$y = f\ (x_1, x_2, \ldots\ldots x_n) + \varepsilon \quad \ldots\ldots \tag{1}$$

where y = *output variable;*

f = *function;*

$x_1, x_2, \ldots\ldots, x_n$ = *input variable;*

ε = *error.*

Researchers and engineers across the globe have widely used RSM for optimization and prediction purposes due to the following advantages:

1. Collecting huge information with limited experiments.
2. Collected data helps to build models and correlate input–outputs.
3. Graphical representation of data that correlates input–outputs of any process.

4. Help to analyze all individual, quadratic (nonlinear or linear), and interaction factor effects on responses.
5. Optimize multiple responses by determining a set of input variables.

The major disadvantages are:

1. The model does not explain the process mechanics.
2. The models fit data corresponding to first- or second-order polynomials and do not explain all curvature information.
3. An increase in independent variables increases the practical experiments, resulting in low prediction.
4. The models are best suited to analyze and optimize a few independent variables.

RSM was used to determine a correlation between input variables (tool RS: 650–850 rpm, TS: 10–50 mm/min, tool tilt angle: 1–3°, tool pin profile: cylindrical, tapered, taper threaded, cylindrical threaded, square) and an output variable (maximum tensile strength) for tailored welded blank sheets of FSW of AA1100 with AA6061 [144]. The model predicted a better correlation coefficient with an R^2 value of 0.96. Tensile strength increased with RS, TS, tilt angle, and pin profile up to middle value, and after that, decreased. Due to severe plastic deformation, fine and equiaxed grain structures could be observed at the stir zone. The TMAZ region showed deformed non-recrystallized coarse grain in the HAZ. Friction stir spot welding of AA6061-T6 aluminum alloy was carried out to correlate inputs (RS: 1300–1700 rpm, PD: 2.2–2.8, and sleeve moving rate: 0.75–1.25 mm/s) and lap shear fracture load (LSFL) [141]. The Box–Behnken design model developed a polynomial equation that predicted close to experimental values. An increase in process variables increased the LSFL, which thereafter decreased. The optimal conditions (7934 N for 1506 rpm, 1.01 mm/s, 2.46 mm) resulted in a maximum LSFL value equal to 7934 N. The RSM method was applied to analyze the process parameters (spindle speed: 1100–1500, welding speed: 2.4–4 mm/s, two pin profiles: tapered squared and tapered pentagonal) on performance (tensile strength, hardness, toughness) of double-side friction stir weld of AA6082-T6 alloy [145]. The tapered squared and pentagonal pin profiles resulted in a maximum strength equal to 149 and 155 MPa, hardness of 75 and 87 HV, and toughness value equal to 1.83 and 1.91 kg(f)m. The FSZ showed a fine-grain structure with a tapered pentagonal tool profile rather than a tapered square tool one. The RSM method was applied to analyze and optimize inputs (RS: 1200–1400 rpm, traverse speed: 75–125 mm/min, axial force: 5–7 kN) on the tensile strength of FSW of AA8011-6062 joints [146]. For the welding strength, the axial force contributed 90% to the welding strength, whereas the welding speed had the least significant effect. The tensile strength increased with an increase in RS up to a certain value, which thereafter decreased. Taguchi L_{18} experiments were conducted corresponding to inputs (RS: 560–1800 rpm, TS: 50–150 mm/min, tool tilt angle: 0–5°, tool material: stainless steel, carbon steel, anti-heat steel) on mechanical properties of butt welded AA6061 joint [147]. RSM-optimized conditions resulted in a maximum strength equal to 200 MPa and a hardness of 110 HV. Elongated and deformed grains with fracture occurred at the TMAZ. The grains appeared elliptical with an onion ring structure at the NZ. RSM (significant benefits in process analysis and optimization) is applied for Taguchi experiments (minimize experimental trials) to collect detailed insights into factors analysis (individual, curvature, and interaction) and perform process optimization. The RSM optimizer provides insights to apply weights to individual responses while performing multiple objective optimizations.

3.1.4. Factorial Design (FD)

In experiments that require the study of more than two factors, FD is an effective technique. The FD method tests all sets of factors and levels. For example, if the x and y levels for each factor are X and Y, then xy combinations are possible. In general, there are n replicates [148]. It is the most preferred DoE technique when there are few parameters [149]. FSW of AA7475-T7 lap joint properties (mechanical and microstructure) were evaluated [150]. Full factorial designed (FFD) experiments (say, 27) were conducted corresponding to three factors (RS: 1000–1400 rpm, traverse speed: 20–36 mm/min, and plunge speed rate: 0.04–0.08 mm/s) operating at three levels, and the joint strength and hardness were analyzed. RS contributed more towards UTS and hardness. The optimal conditions (RS: 1400 rpm, traverse speed: 30 mm/min, and plunge speed rate: 0.06 mm/s) resulted in 172.88 MPa and a hardness of 200 HV, compared with the initial condition of 130 MPa and 125 HV.

FSW of AA1100 aluminum rolled plates was examined for mechanical and microstructural characterizations [151]. Two-level FFD of experiments (say, eight) with different sets of RS: 1100–1500 rpm, traverse speed: 20–60 mm/min, and PD: 0.1–0.5 mm were conducted, and the joint strength was analyzed. The regression model developed from the experimental data examined the factor's effect on strength. Tool RS contributed more toward axial thrust and torque forces. A significant decrease in the two forces was observed. Microstructural studies revealed grain size refinement with increased factors (0.48 to 0.36 microns for RS, 0.45 to 0.40 microns for traverse speed, and an increase in grain size from 0.40 to 0.46 microns for PD). A microscopic examination of the joint revealed unrefined and irregular strip-like grains in the BM that were elongated in the rolling direction. No significant change in grain size was observed at the HAZ and BM zones. The TMAZ showed a deformed pattern and grain movement in the shoulder direction surrounding the NZ. The NZ displayed a fine equiaxed grain structure. At an RS of 1100 rpm, microhardness decreased around the periphery of the NZ, and 38 HV was measured in the NZ. An increase in the RS (1100–1400 rpm) witnessed higher tensile strength. However, tensile strength decreased at 1500 rpm. Low material flow stress between the tool and workpiece was attributed to increased heat generation during welding, changing the friction condition and forming a void defect in the weld joint. FFD experiments were conducted with selected process variables (RS: 1000–2600 rpm, TS: 10–30 mm/min, pin profiles: cylindrical, square, and triangular), and the strength of butt-configured polycarbonate joints was analyzed [152]. Axial force and torque signals were acquired from the machine, and K-type thermocouples were placed on advancing and retreating sides at 9 mm from the weld centerline. The highest welding strength was recorded with squared pin configuration, an RS at 1800 rpm, and a TS: 20 mm/min. A triangular pin profile resulted in a lower peak temperature and cooling rate. The literature review on the FFD technique confirms its effectiveness in providing detailed insights into the FSW process. Still, the cost of experimentations is comparatively higher than fractional factorial-designed experiments such as Box–Behnken (BBD) and central composite designs (CCDs). The optimal conditions for a response lie at the extreme corner of factor levels; the performance of CCD is better, and optimal conditions at the middle of the factor levels BBD are better. Unlike the Taguchi method, RSM derives empirical equations, which many researchers use to perform prediction and optimization.

Advantages and Limitations of RSM

The major advantage of RSM is as follows:

1. The possibility of obtaining huge amounts of information in a limited number of experiments.
2. It also provides build models and graphical data to correlate the relationship between the process parameters.
3. It provides optimum response and optimal conditions from multiple responses.
4. The RSM model provides detailed insight into full quadratic factor effects on response functions.
5. The RSM model derives empirical equations that can be applied for prediction and optimization.

The major disadvantage of the RSM method is as follows:

1. The RSM method does not explain process mechanisms.
2. It can fit data to first- or second-order order polynomials, so it cannot explain all systems containing curvature.

3. If the number of independent variables increases, the number of experiments also increases, thus lowering the prediction capability. So, it is feasible with few parameters.
4. The ML techniques discussed in Section 3.2 overcome these limitations.
5. The RSM method is not an efficient technique for solving multiple objective functions that are nonlinear and multi-modal.
6. RSM presents an unlimited saddle function in a quadratic model (response surface) possessing more than three responses and, therefore, is limited for responses ≤ 3.
7. RSM may not be a cost-effective technique for many manufacturing sectors.
8. RSM-derived response equations require continuous differentiable to locate optimal conditions.
9. RSM-derived empirical equations predict only one output at a time.

3.2. Artificial Intelligence (AI)

A computer's ability to carry out tasks using its reasoning skills, generalization, and past experiences is known as artificial intelligence. For AI to work independently, it needs to be trained. Data must be fed to it, and it must be taught to analyze the problem, consider past experiences and logic, and generate an optimal solution. AI is widely used worldwide for applications like medical, voting prediction, hacking, traffic control, autonomous robots, underwater robots, and many others. For AI to work efficiently, different methods are used. In the case of FSW, it has been predominantly used to optimize process parameters and generate the most favorable value. AI methods are classified into ANN, ML, fuzzy logic, and hybrid modes. AI methods help to reduce the computational cost of optimization. Multiple huge datasets will be fed into the system to perform complex tasks to minimize error and computational time. Automation is one of the benefits of using AI.

3.2.1. Artificial Neural Networks (ANNs)

Recently, many researchers have used ANNs, GAs, and ML algorithms in addition to Taguchi optimization techniques. ANNs predicts the FSW parameter's effects on the final part quality characteristics. Inspired by biological–architectural nodes, it uses existing data to train a network with specific input parameters (called neurons) and predicts outputs [153]. ANNs learn from input–output data and establish nonlinear and complex relationships using algorithms. The major disadvantages include computational burden, overfitting of the data, and a "black-box" nature (no information about its internal working). The main feature of ANNs resembles that of a human brain. The neuro-physical structure of the human brain inspires researchers/scientists to develop a mathematical model. Various artificial cells and network models were developed [31].

In general, ANN architecture comprises input (neurons of the input layer are process variables), hidden, and output (neurons of the output layer are output quality characteristics) layers. There are multiple hidden layers, and the neuron numbers are decided based on training data [154]. In addition, bias (helps in producing constant output during training), weights (acts as connection strength between layers), and transfer functions (tangent sigmoid $\phi(x)$, logarithmic sigmoid $\psi(x)$, and pure linear $\chi(x)$ compute the outputs from inputs of the preceding layer) are the network parameters. During the learning process, the weights are updated in the network architecture. The network performance is affected by the configuration of single and multiple layers [155]. Numerous iterations of training the network with different samples result in a corrected output. Figure 13 shows the architecture of an ANN.

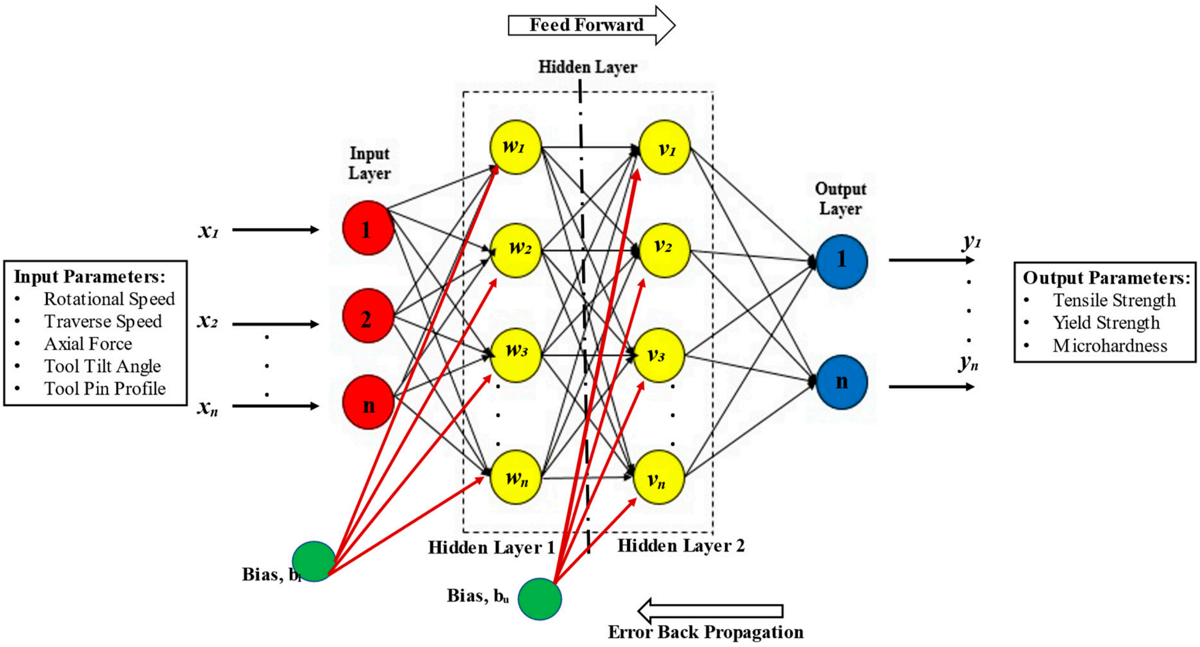

Figure 13. Architecture of an ANN (redrawn from [149]).

The mathematical expression of the transfer functions is given below [155]:

$$\varnothing(x) = \frac{2}{1+e^{-2x}} - 1 \quad \ldots\ldots\ldots\ldots \tag{2}$$

$$\psi(x) = \frac{1}{1+e^{-x}} \quad \ldots\ldots\ldots\ldots \tag{3}$$

$$\chi(x) = \text{linear}(x) \quad \ldots\ldots\ldots \tag{4}$$

The nodes and hidden layers are decided based on the error minimization criterion during training. The input values are normalized to 0–1 to prevent data scattering. This is performed by dividing all the values by the maximum value of that parameter and reaching a normalized value [154].

A supervised learning mechanism of the backpropagation algorithm is used to train an ANN. Input data are fed in batch mode to the input layer and transform computed outputs viz. transfer functions. The outputs of the input layer are the inputs to the hidden layer and generate hidden layer output viz. transfer function, and the hidden layer output is the input to the output layer, which produces output using the transfer function. The transfer function selection is investigator preference, and no universal standard rule has been defined yet. Mean squared errors (MSEs) are computed to record the difference between measured (target or experimental) values and network-predicted values [156]. The datasets are divided into 65–75% for training, and the remaining 15–30% is applied for testing and validating the network. The objective of the backpropagation algorithm is to reduce the errors to the minimum possible [154,156].

In Figure 13, x_1, x_2, x_n: input parameters, w_1, w_2, w_3: weighted average of hidden layer 1, v_1, v_2, v_3: weighted average of hidden layer 2, and y_1, y_2, y_n: output parameters.

FEM simulations were carried out to collect data required for optimization, and the multi-objective optimization of FSW parameters is performed using an ANN [157]. An ANN was hybridized with multi-objective particle swarm optimization (MOPSO) to determine RS and TS on an AA7075/AA5083 butt joint [158]. During the learning process, the BP algorithm optimized the network parameters by minimizing error. A trial–error approach was used to optimize network parameters. The network architecture comprised

2-6-2 (input, hidden, and output neurons). TS, RS, and the tensile shear force and hardness for the output layer represented neurons at the input layer. The Levenberg–Marquardt optimization learning algorithm was applied to train the ANN with 16 data patterns and compute correlation coefficient (R^2) with changes in network parameters (hidden neurons, bias, constants of transfer function, etc.). MOPSO determined the Pareto optimal solutions, and TOPSIS located the best solution. An RS: 1182.11 rpm and TS: 11 mm/min resulted in maximum hardness and UTS equal to 96 HV and 265 MPa.

A coupled Eulerian–Lagrangian (CEL) numerical simulation model was applied to determine the influence of RS and TS on temperature, von-mises stress, heat flux, and strain [159]. The ANN architecture (2-10-4) was trained with the BP algorithm based on 25 numerical simulation datasets. A total of 12 datasets were tested against prediction accuracy, resulting in the prediction of 1.25% for plastic strain, 0.164% for temperature, 0.2% for heat flux, and 0.3% for von-mises stress. High temperature and residual stresses were observed on the retreating side. An increase in RS resulted in increased grain size due to increased temperature, heat flux, stress, and plastic strain values. Experiments were conducted with different sets of traverse speed rates: 15–35 mm/min, RS: 800–1000 rpm, and H13 steel tool profiles: cylindrical threaded and square, and the AA6061-T6 joint strength was analyzed [160]. The cylindrical threaded tool profile, RS: 1000 rpm, and traverse speed rate: 15 mm/min produced higher YS and UTS equal to 78.4 MPa and 107.49 MPa. The squared tool profile with RS: 900 rpm and traverse speed rate: 25 mm/min resulted in higher YS and UTS equal to 121.79 MPa and 151.61 MPa. The ANN predictions were in reasonable compliance with the experimental data. Dissimilar welding of AA 6063-O and AA 2014-T6 plates was carried out with process variables such as RS: 635–1270 rpm, TS: 30–75 mm/min, and the strength and hardness were analyzed [161]. An ANN trained with the BP algorithm improved the correlation between the input and output. The datasets were divided into training and testing and validation equal to 60% and 40%. The ANN predicted hardness and strength close to the experimental values. The GRA was applied to optimize FSW parameters, resulting in better properties. The growing importance of ANNs indicates a lot of potential to explore ANNs in manufacturing. Table 5 shows the application of ANNs in FSW.

Table 5. Application of ANNs in FSW.

Material Details	Process Parameters	Description of the Work	ANN Architecture	Ref.
AA5086–H34 joints reinforced with Al_2O_3 nanoparticle reinforcement Material dimension: 200 × 50 × 6 mm plates	RS: 1000, 1250, 1600 rpm WS: 41.5, 80, 125 mm/min No. of weld pass: one, two, and four	Establish a correlation between FSW parameters and joint properties. Five-pin geometries (square, cylindrical) used to make 140 joints.	Training: 70% data Validation: 20% data Testing: 10% data Maximum epoch: 18 Feed-forward back-propagation neural network	[162]
Results: • Average error detected: 3.85%.				
AZ31 magnesium alloy sheet Material dimension: 180 × 80 × 2 mm	RS: 1350, 1700 rpm WS: 45, 80 mm/min	Establish a relationship between vertical force and processing time (PT). Support vector machine (SVM)-based ANN was trained with different values of processing parameters. LM algorithm trained ANN. Compare prediction accuracy with LM ANN and SVM ANN.	Two network architectures: Network 1: RS, WS, PT Network 2: RS, WS, PT, RS to traverse speed ratio Maximum epoch: 189 MSE: 0.0014	[163]
Results: • ANN model replicated the behavior and forecasted the negative relationship between vertical force and RS. • ANN model predicted a positive correlation between vertical force and traverse speed.				

Table 5. *Cont.*

Material Details	Process Parameters	Description of the Work	ANN Architecture	Ref.
7075-T6 aluminium alloy Material dimension: 150 × 300 × 5 mm Single-pass welding	Inputs: RS, AF, SD, PD, tool hardness Outputs: YS, UTS, hardness, notch tensile strength	BP algorithm-trained ANN. Prediction of mechanical properties of FSW processed 7075-T6 joints. Compare prediction and experimental values.	ANN architecture: 6-4-4 Training and testing data: 15 and 15 Normalization of inputs: 0 to 1 Sigmoid and linear transfer functions were used Optimum values: RS: 1400 rpm, AF: 8 kN, hardness: 45 HRc, SD: 15 mm, and PD: 5 mm	[164]
Results: • Optimum values: RS: 1400 rpm, AF: 8 kN, hardness: 45 HRc, SD: 15 mm and PD: 5 mm • ANN predictions closely resemble experimental data				
Aluminium alloy AA8014 Square butt joint Single-pass welding	SD: 16–24 mm RS: 355–2000 rpm WS: 20–63 mm/min AF: 1–4 kN Pin material: high carbon steel, high chromium steel, and H13 Output: tensile strength	Predict the tensile strength of FSW AA8014.	Network architecture: 4-5-1. 4-6-1. 4-7-1, 4-8-1. 4-10-1 Training data: 70% Testing and validation data: 15% Normalization: 0.1–0.9 Log–sigmoid transfer function Learning rate: 0.01 Momentum constant: 0.9	[165]
Results: • Better R^2 value equal to 0.99. • Optimal network configuration: 4-8-1.				
Aluminium plates Material dimension: 5 × 50 × 150 mm	RS: 500–1250 rpm TS: 6.25–20 mm/min Plunge force: 210 N	ANN for predicting properties of aluminium plates.	BP algorithm-trained ANN ANN architecture (2-5-7) Training data: 15 Testing data: 5	[166]
Results: • RMS error obtained for the hardness of HAZ: 0.0115, weld metal: 0.0064, elongation: 0.0566, yield strength: 0.0253, and tensile strength: 0.018. • The R^2 value for all the outputs was greater than 0.99.				
AA7050 aluminium alloy	Inputs: TS, rotation rate Outputs: Hardness and peak temperature at nugget and HAZ	Application of ANN to AA7050.	LM algorithms train the ANN Training data: 70% Testing and validation data: 15% + 15% Network architecture: 2-1-1; 2-5-1; 2-10-1	[167]
Results: • Network architecture (2-10-1) resulted in better correlation coefficients equal to 0.97. • Network architecture (2-10-1) for the hardness of HAZ with better correlation coefficients equal to 0.964. • Network architecture (2-10-1) for peak temperature of weld nuggets with better correlation coefficients than other networks. • The correlation coefficient increases with increased neurons at the hidden layer for hardness and peak temperature.				
AA6061 aluminium plates Material dimension: 130 mm × 100 mm × 6 mm	Inputs: Two pin profiles: triangle and tapered cylindrical RS: 1000 rpm TS: 28 mm/min Output: hardness	Predict the hardness of joints.	Datasets: 51 for triangle pin profile Log–sigmoid and Tan–sigmoid Triangle pin profile: 3-8-1, 3-4-7-1, 3-5-6-1, 3-6-4-1, and 3-5-6-2-1 Datasets: 48 for tapered cylindrical pin Tapered cylindrical profile: 3-6-1, 3-7-3-1, 3-7-5-1, 3-4-5-1, 3-3-6-2-1, and 3-6-5-2-1	[168]
Results: • ANN architectures 3-8-1 and 3-7-3-1 showed better performance for predicting the microhardness of the specimen. • Compared with flat, the best weld quality was observed with concave tool shoulders.				

Table 5. *Cont.*

Material Details	Process Parameters	Description of the Work	ANN Architecture	Ref.
AA 5052 to AISI 304 joints Material dimension: 150 mm × 100 mm × 3 mm	RS = 500–1000 rpm TS = 40–80 mm/min Tool offset = 1.6–2.0 mm	ANN and GA are applied to optimize process parameters.	ANN model correlates input–output variables BP algorithm is applied to train ANN Training and testing data: 21 and 6	[169]
Results: • ANN-GA predicted the optimal parameters equal to 500; 25 rpm, 80 mm/min, 1.76 mm tool offset. • The predicted UTS and %elongation values were 186.9 MPa and 6.84%. • The experimental values obtained were 194.03 MPa and 7.11%.				
AA7039 alloy Material dimension: 100 mm × 75 mm × 4.35 mm	RS = 1325–1812 rpm TS = 26–43 mm/min Tilt angle = 1.3–2°	LR, SVM, GPR, and ANN predict the tensile strength.	The parameters such as dwell time and tool plunge are maintained constant at the 30 s and 0.1 mm Training and testing data: 70% and 30%	[170]
Results: • The GPR model showed the best coefficient of correlation and root mean square error values equal to 0.984 and 9.985. • The ANN model showed the best coefficient of correlation and root mean square error values similar to 0.986 and 7.23. • ANN outperformed other models in predicting outputs.				
Copper alloys To classify mechanical properties	Inputs: RS, WS, SD, PD, and tool tilt angle Output: UTS	Four ML algorithms: K-nearest neighbor, (KNN), decision tree (DT) with Gini index, information gain, ANN classification model.	If UTS < 80%, parent metal output dataset is 0 and UTS > 80% of the output is treated as 1.	[171]
Results: • Based on the *p*-value ($p < 0.05$), the Pearson product-moment correlation revealed that traverse speed was the least significant parameter, so it was not considered. • From four ML models: ANN showed the highest accuracy of 92%, KNN and DT models revealed 92% accuracy, and the DT model with Gini index showed 89% accuracy.				

3.2.2. Machine Learning (ML)

Developments in mathematics and computer science lead to the creation of new software tools that can enhance manufacturing capability beyond restricted boundaries. Machine learning is a data-driven approach that uses algorithms to design models and draw inferences based on some patterns [172]. Using three different techniques—supervised, unsupervised, and reinforcement—ML draws inferences and suggests an ideal solution [173]. The authors of [174] surveyed various machine learning techniques used in FSW of different aluminum alloys and outlined the unresolved issues. These issues are highlighted in their paper's conclusion and future scope section. The algorithms (image pyramid and image reconstruction) were applied to determine the FSW-processed AA 6060 T5 plates [175]. Four welded specimens were prepared with different sets of RS: 1500–2000 rpm, TS: 200–400 mm/min, and AF: 1.5–2.5 kN. The image was divided by 1.2 in width and height for every iteration. The threshold value for noise removal was kept at 0.8. A grayscale image was the mask, and an eroded image was the marker. Sobel approximation was used to identify the image's edges. The authors were able to study the cracks and defects using an image processing technique and suggested the use of a convolutional neural network for better and optimized results. The tensile behavior of FSW processed AA7039 joints (inputs: RS: 1325–1812 rpm, WS: 26–43 mm/min, tilt angle: 1.3–2°) was predicted viz. ML algorithms (GPR, SVM, ANN, LR) [170]. The 70% training data reduced the RMSE, offered a better correlation coefficient, and resulted in better prediction with unknown test datasets. The highest tensile strength of 477 MPa was observed at RS: 1325 rpm, WS: 35 mm/min, and tilt angle: 1.65°. A detailed analysis of the review on artificial intelligence and machine learning algorithms was applied to confirm the prediction accuracies in optimizing the process. Many researchers used the design of experiments technique to collect data required to train a network, viz. different algorithms and then applied them for predicting outputs from a known set of inputs. Unlike RSM, an ANN can simultaneously predict multiple outputs from numerous input–output datasets.

Advantages and Limitations

The significant advantages of ANNs are as follows [176]:

1. The storage of information in the whole network is the ability to work with missing data and parallel processing capability.
2. ANNs can be applied to develop a process model relating linear or nonlinear relationships between responses.
3. An ANN is an efficient tool to overcome the shortcomings of low-order polynomial equations and data containing noise or missing data for better predictions.
4. The ANN model aims to predict multiple outputs simultaneously.
5. ANNs can be applied for both online and offline process monitoring.

The significant disadvantages of ANNs are as follows:

1. An ANN uses weight between the network layers without knowing their physical inference while modeling.
2. ANN models require tuning network architecture parameters (number of hidden layers and neurons, learning rate, momentum constants, transfer functions, bias) for accurate predictions.
3. The major limitation is determining the neural net's proper size and optimal structure.
4. An ANN is a "black-box" model; determining the weight relationships between input-output parameters is not known, and hardware implementation of neural networks is costly [166].

Welding processes (FSW, EBW, SAW, and GTAW) were optimized with an objective function derived based on regression models and applying quasi-oppositional-based Jaya algorithm (QO-Jaya) in [177]. Jaya algorithms and their variants were compared with GA, TLBO, and SA. In another study, FSW process parameters (pin profile, RS: 1000–1400 rpm, TS: 600–1000 mm/min, AF: 8–16 kN) were optimized for better corrosion resistance [178]. Jaya and QO-Jaya algorithms produced a computationally efficient solution with 5.73% better corrosion resistance than the others. Central composite design experiments were conducted with four different sets of inputs (tool pin profile: cylindrical, square, tapered cylindrical, threaded cylindrical, triangular, RS: 800–1600, WS: 0.25–2.25 mm/s, and AF: 5–9 kN) on mechanical properties (UTS, YS, and hardness) of FSW of AA7075 joints in [179]. The developed hybrid model (ANFIS and SA algorithm) was trained with 31 experimental datasets and tested with 10 datasets (which were not used during training). The ANFIS model consisted of five layers (input–product–normalization–defuzzification–output) trained with Takagi–Sugeno fuzzy type rules. The bell-shaped membership function helped to reduce the RMSE to a low value. The output of the ANFIS model served as an input to the simulated annealing algorithm. The square pin profile, RS: 1400 rpm, WS: 1.75 mm/s, and AF: 7.5 kN resulted in the highest mechanical properties in optimizing single and multi-responses simultaneously. In [179], FSW parameters (RS and WS) were optimized using GA for higher tensile strength in AA5083 and AA7075 joints. An empirical second-order regression model determined the correlation between inputs (RS and WS) and UTS joints. GA parameters (population: 25, elite count: 2–8, cross over: 0.8) resulted in maximum tensile strength (294.388 MPa) with 500 rpm and 50 mm/min. Note that variation in GA parameters produced undesired results.

In [180], ML algorithms (DT, RF, and XGBoost) were applied for predicting YS of AA6061-T6 joints, with the set of inputs being (RS, tilt angle, TS, SD, PD, tool hardness, and thrust force). The models were trained with 75% of the data and tested with 25% of the datasets. The XGBoost model showed the highest accuracy of 95.24% compared with DT and RF models, equal to 90.48%. In another study [181], ML algorithms (LR, PR, SVR, DTR, and RFR) were applied to predict the dissimilar butt-welded joint of AA7050-AA2014A from sets of input variables (RS: 1000–1600 rpm, TS: 30–70 mm/min, tilt angle: 0.5–2.5°).

There were 108 datasets, with 90% training and 10% testing data. The ML approaches reduced error (MSE, mean absolute error MAE, and RMSE). The experimental data were compared with ML-predicted data. Due to insufficient heat and plasticization, tunneling defects were observed with RS: 1000 rpm. A peak temperature < 300 °C was observed at RS: 1000 rpm to ensure defect-free and proper mixing of materials. Sufficient mixing of materials was not observed at 1200 rpm.

The significant advantages of ML are the ability to deal with high-dimensional problems and data, comfortable parameter adjustment, and increased classification performance. Also, ML can identify relationships between unknown knowledge and implicit relationships in datasets. It can adapt to dynamic systems and changing environments [182]. Although ML is effective, it cannot be considered the perfect solution to address all issues. They do not provide data about the algorithm's internal working process, i.e., the "black-box" model. ML model developed for one process cannot be replicated for other similar or different processes. This is due to the stochastic nature of weights and biases and the nature of the training algorithms. Though there are standardized tools for normalizing and filtering data, training data for specific algorithms is tough. The selection of an appropriate algorithm is an essential step in optimization. Real-time monitoring and control of the process using ML models is an area to explore. Pre-processing of data is a critical step.

3.3. Multi-Objective Optimization Techniques

Multi-objective optimization is performed with nature-inspired algorithms like GA, PSO, ABC, HS, and ACO. These are developed based on different natural phenomena. The main reason behind developing these algorithms is to improve the optimization process by parallelly solving two or more functions. In [183], the hybrid fuzzy–grey Taguchi method was used to optimize FSW of dissimilar Al/Cu joints. Taguchi L_{16} experiments (RS, WS, PD, and tool pin offset) were conducted, wherein the fuzzy–grey method ensured transforming multiple outputs into a single output. The average grain size of Al at the HAZ was 70.7 µm and Cu was 71.50 µm. At the TMAZ, the grain size of Al was 51.98 µm and for Cu, was equal to 60.6 µm. At the NZ, the grain size of Al and Cu were equal to 46.61 µm. The hybrid optimization method was effective with increased fuzzy sets and improved accuracy. Note that the average grain size of Al and Cu base metal is 73.64 µm and 228.64 µm. In another study, the dragon fly algorithm was applied to optimize inputs (RS: 700–910 rpm, tool tilt angle: 25–50 mm/s, and WS: 1–3°) for higher impact and tensile strength in FSW AA6082–T6 joints [184]. Taguchi L_{27} experiments were applied with different tool materials (steel, PCBN, and tungsten). The MATLAB version R2021a software platform optimized the inputs, resulting in tensile and impact strength equal to 221.6 MPa and 14 MPa. The algorithm determined the optimized conditions resulted in approximately similar experimental results.

Taguchi L_9 experiments were conducted with different input variable sets (RS: 900–1400 rpm, TS: 16–32 mm/min, tool tilt angle: 0–2°) on the dissimilar welding of AA6061-AA2024 joint properties (UTS and microhardness) in [185]. GRA and DFA were applied to optimize multiple outputs with sets of inputs. Factors contributing to individual output were estimated. Microstructure studies showed refined grains at the NZ compared to the TMAZ and HAZ. In [186], Taguchi L_{16} experiments were carried out with different input sets (RS: 480–1600 rpm, TS: 48–112 mm/min, penetration depth: 0.6–1.2 mm, and tool tilt angle: 0–4°) on the outputs (joint efficiency and microhardness) of AA6061 joints. A cylindrical, tapered tool made of H13 tool steel was applied to perform the welding process. ANFIS was used for prediction, and the neighborhood cultivation genetic algorithm (NCGA) was used for optimization with improved joint efficiency and microhardness. Joint efficiency improved with increased microhardness, corresponding to higher values of RS, TS, and depth of penetration and low values of tilt angle. The lower RS, TS, penetration depth, and higher tilt angle resulted in decreased specific weld energy. The optimal conditions (RS: 560 rpm, TS: 90 mm/min, penetration depth: 0.9 mm, and tool tilt angle: 2°) resulted in a 17% decrease in specific welding energy and an increase in joint efficiency and microhardness equal to 2.3% and 6.4%, respectively.

In [187], CCD based on the RSM technique was applied to optimize the FSW parameters (RS: 800–1200 rpm, TS: 20–60 mm/min, pin profiles: straight cylindrical, straight square, tapered cylindrical) on the performance (surface roughness, and tensile strength) of Al-Mg alloy joints. A higher surface roughness (10.705 µm) was observed at RS and TS equal to 800 rpm and 20 mm/min, and a lower surface roughness (4.9 µm) was recorded at the straight cylindrical pin profile, with RS and TS equal to 1200 rpm and 20 mm/min. The straight squared pin configuration resulted in higher hardness. Samples welded at RS: 1000 rpm and TS: 40 mm/min resulted in the highest tensile strength of 137 MPa, whereas the square pin configuration showed the lowest tensile strength equal to 56 MPa. At an RS maintained at 1000 rpm, the hardness of the samples was 80 BHN, while at RS: 800 and 1200 rpm, the hardness resulted was 70 and 72 BHN. Equiaxed grains were observed at the stir zone, whereas a dendritic structure was recorded at the BM. The BM, TMAZ, and NZ grain size equaled 35.06, 25.25, and 6.14 µm. UTS was 1.5 times higher than YS in the longitudinal direction, whereas it was 1.85 times higher in the transverse direction. The ANN model predicted accurately with experimental data trained with different transfer functions and ANN architectures.

Taguchi experiments with different sets of RS: 670–1180 rpm, TS: 17–48 mm/min, and D/d ratio: 3–3.5 were used to fabricate AA2024-T4 joints in [188]. Weighted principal component analysis (WPCA) was applied to transform multiple outputs into a single output. BP and LM algorithms were used to train the NN with 70% of training data, followed by validation with 15% and testing with 15%. The WPCA-ANN-PSO method was applied to optimize the inputs (D/d ratio: 3, RS: 1180 rpm, TS: 17 mm/min), which achieved the highest UTS and hardness equal to 108.105 MPa (improvement of 20%) and 76 (improvement in 25%), respectively. In [189], Taguchi experiments were carried out with different sets of inputs (RS: 700–1035 rpm, tool tilt angle: 1–3°, TS: 1–2 inches/s), and the strength (YS and impact strength) of AA6082-T6 alloy was analyzed. GRA was used to transform YS and impact strength into a single objective function for optimization. BP and an LM algorithm-trained ANN (training, testing, and validation data equal to 70%, 15%, and 15%) were applied to predict the optimal parameters (RS: 1002 rpm, tilt angle: 1.5°, TS: 1–2 inches/s), and the conical and pyramidal cross-sectioned profile resulted in the highest grey relational grade of 0.508, which was 9.7% better than the GRA alone. In addition, the advantages of obtaining the optimal conditions have been validated with the micro and macrostructure of welded joints (refer to Figure 14).

Advantages and Limitations of ANFIS

ANFIS can handle large amounts of data from nonlinear or complex dynamic systems. It helps in developing systems that have no relationship between inputs and outputs. It can integrate information from several sources for effective model development. While defining ANFIS, input–output variables should be noted, as representing them plays a crucial role. The major limitation is the requirement of a large amount of data for training and validation purposes to prevent under-fitting of the model [155,190]. Some of the recent work in the field of FSW is summarized in Table 6.

Table 6. Multi-objective optimization techniques.

Details (Objectives, Materials, Process Variables)	Optimization Techniques	Optimization Parameters	Ref.
To optimize factors of underwater FSW Aluminium alloy 6082-T6 joint SD: 17–20 mm RS: 710–1120 rpm TS: 50–80 mm/min	Taguchi	• L_{18} standard orthogonal array.	[191]
	PSO	• MI: 25,000, SS: 96, 192, 96. • Number of particles (elements)—32, 36, 32. • Weight damping ratio—0.99, C_1—1.2, 2.4.	
	Firefly	• MI: 5000, SS: 96, 192, 96,. • Number of particles (elements)—32, 36, 32. • Mutation coefficient—0.25. • Coefficient of light absorption—0.25. • Value of attraction coefficient—2.30.	
	NSGA-II	• MI: 20,000 iterations, PS: 300, MR: 0.05. • Number of particles (elements)—96. • Pc: 0.8.	
Results: • Prediction error (maximum and minimum) experiment-wise for UTS, % elongation, and impact strength (IS). • Minimum MSE for Firefly: 0.009% for UTS, 0.004% for % elongation, and 0.017% for IS. • NSGA-II performance was the lowest.			
A multi-objective framework for FSW process parameters AA6061-T6 and pure Cu RS: 800–1600 rpm TS: 0.50–3 mm/s	FFD	• A total of 72 experiments. • Analyzed main and interaction factor effects. • Test at 95% confidence interval.	[149]
	Fuzzy-Based Decision	For selection advancing side material: • Linguistic terms: seven. • Variables and linguistic variables for each parameter: three and three. • Total fuzzy rules = 3^3 = 27. • Cu is identified as an advancing material.	
	ANN	• Training and validation dataset = 26 and 10. • Training algorithm: L-M algorithm. • Learning parameters: momentum and bias constant. • Hidden neurons for UTS, hardness, impact energy: 6, 6, 7.	
	NSGA-II	• PS: 100, MI: 250, MR: 0.3, Pc: 0.8. • Parent selection strategy: binary tournament selection.	
Results: • The optimal result attained using the hybrid algorithm was UTS = 142.32 MPa, hardness = 101.9 HV, and IE = 8.3 J corresponding to inputs, RS = 1693 rpm, TS = 2.72 mm/s and Cu as advancing side material. • The error between the experiment and simulations was found equal to 2.8% for UTS, 1.9% for hardness and 13.7% for IE.			

Table 6. *Cont.*

Details (Objectives, Materials, Process Variables)	Optimization Techniques	Optimization Parameters	Ref.
Multi-objective optimization of FSW parameters using FEM and a neural network AA5083 aluminium alloy RS: 500–1600 rpm TS: 18–60 mm/min Tilt Angle: 3°	FEM	Analyzed RS and TS on outputs: width of HAZ, force and peak temperature. • Workpiece assumed as visco-plastic material. • Constant friction factor at tool–sheet interface • Rigid welding tool.	[157]
	ANN	To correlate inputs and outputs. • BP algorithm-trained ANN. • Network architecture: 2-8-2. • Log–sigmoid transfer function. • Training and testing data: 80% and 20%.	
	NSGA-II and TOPSIS	NSGA-II: Generation of a Pareto front • PS: 100, MI: 500, P_c and P_m: 0.7. TOPSIS is applied to select a single solution from the Pareto set: Four optimum design points oint A: 1344.599 rpm, 59.753 mm/min 529.3366 °C, 55.29098 mm, 548.8909 N Point B: 553.621 rpm, 42.901 mm/min 474.9437 °C, 22.77745 mm, 732.75 N Point C: 882.719 rpm, 57.773 mm/min 502.7696 °C, 31.68555 mm, 709.8935 N Point D: 1393.059 rpm, 32.137 mm/min 552.6367 °C, 89.62572 mm, 220.7031 N	
Results: • The correlation coefficient was equal to 0.9721 for peak temperature, 0.985 for force, and 0.9645 for HAZ width.			
Optimization of FSW parameters of ZE42 alloy AF: 3–7 N RS: 950–1350 rpm WS: 20–100 mm/min Pin profile: cylindrical, square	RSM	• BBD of experiments were conducted. • Process parameters are set at five levels: −2 to +2.	[192]
	GRA	• Optimal parameters: RS: 1250 rpm, WS: 40 mm/min, square profile, AF: 6 N. • Percent contribution for AF, RS, WS, and pin profiles equal to 3.5%, 13.1%, 9.98%, and 68.5%.	
Results: • ANOVA predicted that axial force contributed 68% impact, traverse speed 13% impact, and pin profile 9%. • Applying GRA increase in the hardness and UTS value from 86.14 to 89.31 BHN and 183.45 to 187.26 MPa.			
Optimization FSW process parameters of armor AA7039 T6 **Process Parameters:** SD: 15–21 mm Shoulder flatness (SF): 1–3 mm Pin profile: straight cylindrical, triangular, square WS: 15–45 mm/min Three levels: −1, 0, +1	RSM	• CCD composed of 21 experiments corresponding to three levels for each factor. • Identification of process parameters. • Three models were developed for UTS, YS and EL.	[193]
	PCA	• Determines weight fraction for individual output. • Comparative importance of each response. • Contribution of: UTS: 34.6%, YS: 34.6%, %EL: 30.8%.	

Table 6. *Cont.*

Details (Objectives, Materials, Process Variables)	Optimization Techniques	Optimization Parameters	Ref.
	GRA	• Normalize the data of each response. • A single score of each grey relation grade (GRG) response. • Optimal values correspond to higher values of GRG.	
Results: • Coefficient of determination R^2: 0.998 for UTS, 0.997 for YS, and 0.904 and EL. • The 14th experiment resulted in the highest GRG: 344.5 MPa for UTS, 253.8 MPa for YS, and 14.2% for %EL.			
Mechanical and corrosion studies of FSW Al_2O_3 nano-reinforcement in Al-Mg matrix composite Pin profile: straight cylindrical, tapered cylindrical, straight square RS: 800–1200 rpm TS: 20–60 mm/min	RSM	• CCD experiments for three factors and three levels. • Coefficient of determination: 0.9652 for YS	[194]
	ANN	• Three-layer ANN architecture. • Input layer: two neurons. • Output layer: one neuron for average tensile strength. • Hidden layer neurons for predicting YS: 6, 8, 10, 15, 20 and 25. • Hidden layer neurons for predicting UTS: 6, 8, 10, 12, 14, and 16. • Training, validation, and testing data: 70%, 15%, and 15% • L-M algorithm-trained ANN minimizes MSE.	
Results: • Maximum tensile strength of 203.95 ± 0.15 MPa obtained at 6 wt. % nano Al_2O_3-dispersed MMNCs, RS: 1000 rpm, WS: 60 mm/min, square pin profile, AF: 4 kN. • ANN predicted with 99.9% with 6–16 neurons in the hidden layer.			
Input–output modelling of FSW using metaheuristic tuned ANFIS model Aluminium magnesium alloy (AA5052-H32) Hexagon tool profile, 400 rpm, 45 mm/min, 0.5° Pentagon tool profile, 500 rpm, 55 mm/min, 1° Square tool profile, 600 rpm, 65 mm/min, 1.5° Cylindrical tool profile, 700 rpm, 75 mm/min, 2° Triangular tool profile, 800 rpm, 85 mm/min, 2.5°	RSM	To determine the mathematical relation between joint strength and FSW input parameters. • Four-factor five-level CCD is selected. • A total of 31 actual experiments. • Five levels: −2, −1, 0, 1, 2.	[195]
	GA-ANFIS	Optimized Internal Parameters: • MI: 1000, PS: 100, Pc: 0.8, Pm: 0.07, MR: 0.15. • Selection pressure (β): 8.	
	GA-PSO	Optimized Internal Parameters: • MI: 1000, PS: 100. • Cognitive acceleration (C_1): 1. • Social acceleration (C_2): 2. • Inertia weight (W_{min}): 1. • Inertia damping ratio (W_{damp}): 0.99.	

Table 6. *Cont.*

Details (Objectives, Materials, Process Variables)	Optimization Techniques	Optimization Parameters	Ref.
Results: • Joint strength (MPa): Experimental—180.9, GA-ANFIS: 180.45, PSO-ANFIS: 180.09; Regression—179.81 for square tool profile, 500 rpm, 55 mm/min, 0.5°. • Joint strength (MPa): Experimental—184.79, GA-ANFIS: 184.82, PSO-ANFIS: 184.77; Regression—182.33 for cylindrical tool profile, 500 rpm, 65 mm/min, 1°. • Joint strength (MPa): Experimental—195.93, GA-ANFIS: 193.87, PSO-ANFIS: 195.93; Regression—196.56 for square tool profile, 500 rpm, 75 mm/min, 1.5°. • Joint strength (MPa): Experimental—196.82, GA-ANFIS: 197.86, PSO-ANFIS: 196.89; Regression—192.71 for pentagon tool profile, 500 rpm, 75 mm/min, 2°. • Joint strength (MPa): Experimental—183.48, GA-ANFIS: 183.53, PSO-ANFIS: 183.48; Regression—180.94 for hexagon tool profile, 500 rpm, 65 mm/min, 2.5°.			

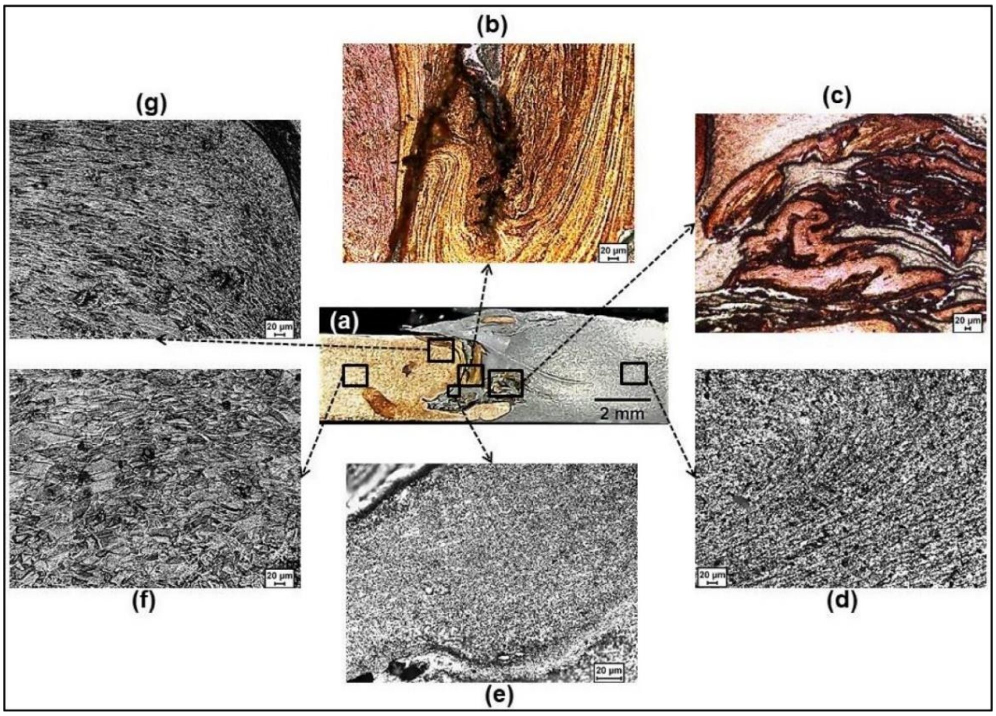

Figure 14. Microstructure of a welded specimen. (**a**) Macrostructure of a joint at the optimal parameter. (**b**) Lamellar flow in the middle part of the microstructure. (**c**) Complex mixing of Cu and Al denoting sufficient deformation and composite structure. (**d**,**f**) Different size, shape, and orientation of grains. (**e**) Fine grains of size 3μm at interface. (**g**) Variation in the grain size at the interface [149].

3.4. Summary

The following observations were made:

1. The main objective of RSM is to understand the topography of the response surface and find the region where optimal response occurs.
2. The linear regression model gives a minimum percentage error between experimental and predicted values. It is based on supervised learning and assumes a linear relationship between variables. This is one of the disadvantages of a linear regression model. ANFIS can be used for nonlinear relationships.
3. The backpropagation algorithm (BP) is the most extensively used ANN algorithm implemented online or in batch mode. Its accuracy is less than metaheuristic algorithms. Problems like determining the optimal number of neurons, the best learning rate in each hidden layer of an ANN, and the global optimum solution cannot be determined using the BP algorithm.

4. Underfitting and overfitting in an ANN generate errors during the network training. Underfitting occurs when an ANN cannot accurately capture the relationship between input and output variables, resulting in high error. Overfitting refers to extra data generated along with noise from the training stage.
5. The image processing technique has been predominantly used for detecting cracks and defects. Convolutional neural networks would yield better and optimized results.
6. Taguchi and RSM have been widely used with ML techniques for determining/predicting more optimal values. These include Taguchi-GRA, RSM-ANN, Taguchi-PSO, and RSM-PSO-Firefly, to name a few.

4. Process Measurement

The need for high-quality products requires the need for constant monitoring of any process. Industries are adopting newer technologies to improve the efficiency of the process. Sensors are an effective way to constantly monitoring the process. Real-time monitoring helps parameters adjust and enhance the mechanical properties of FSW components. Online process measurement of any manufacturing system assists in the smooth production of the process. An efficient system helps in the early detection of failures [196]. Process monitoring takes constant feedback from sensors and is performed in two ways: online and offline. In the case of FSW, the parameters are categorized into three parts: i. joining; ii. material; and iii. design. Heat generation is affected by joining parameters (including RS, TS, tilt angle, and PD) and is controlled with online methods. The tilt angle enhances the flow of plasticized material. Amongst the process parameters, rotational and welding speed plays a pivotal role in forming joint quality. Tool profile and dimensions are subcategorized into design parameters and are constant during the process. Tool profile dimensions affect the welded specimen properties. Workpiece material, tool material, and backing plate are material parameters that are kept constant [195]. Figure 15 shows the classification of various process parameters controlled with online and offline methods. Figure 16 shows the positioning of multiple sensors in an FSW machine.

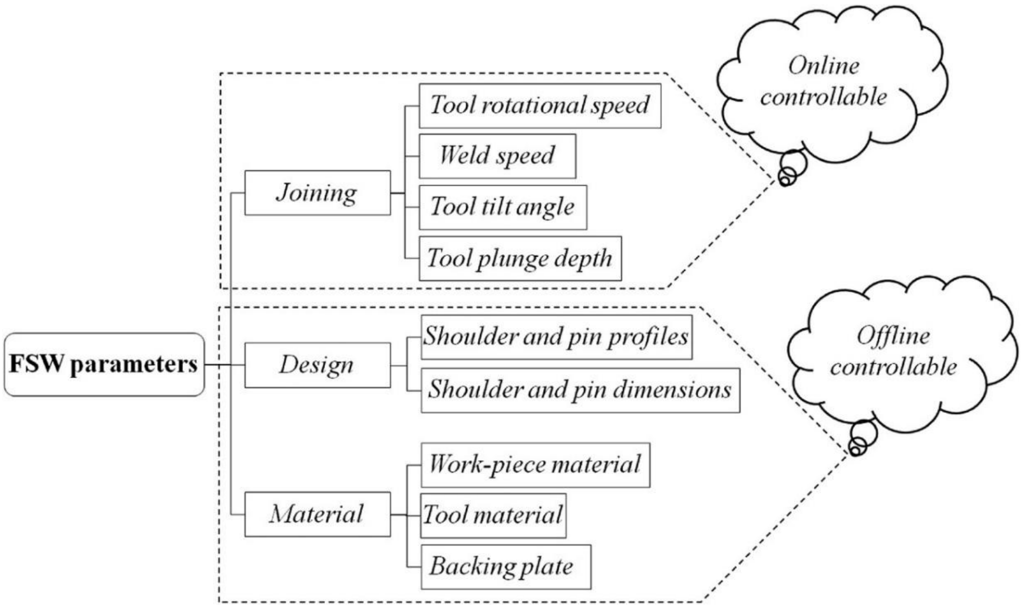

Figure 15. Classification of process parameters [197].

The basic process begins with identifying the process parameters and selecting a suitable sensor to acquire the parametric data. The next stage involves using processing techniques to extract data from the signal and analyze it to identify the errors and control the process accordingly. Once the sensor signal is acquired, suitable processing techniques are applied to extract the features. These signals show the variations that happen during the process and assist in controlling the process [196,197].

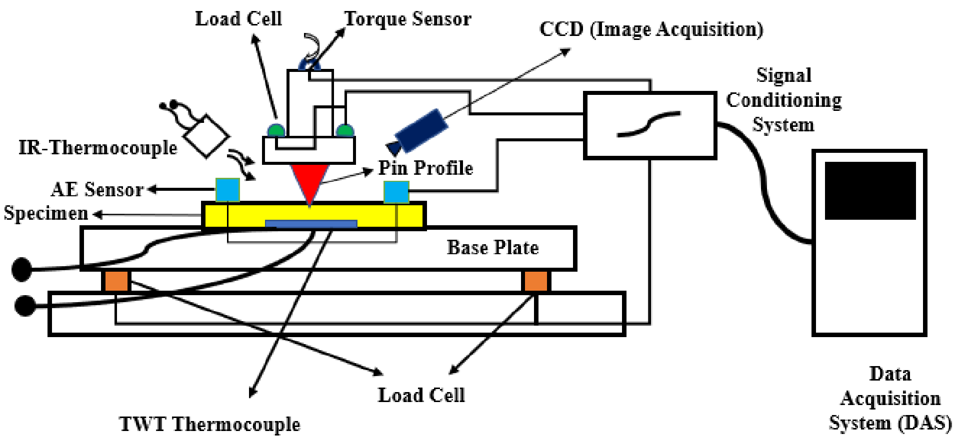

Figure 16. Sensors position in FSW machine (AE—acoustic emission, IR—infrared, CCD—charge-coupled device).

Babalola et al. [37] discuss the in-situ process monitoring strategies for FSW machines by considering three case studies: i. AA2014–AA6063 possessing at 6 mm thick; ii. AA6063-T6 keeping Ø50 mm pipes; and iii. AA1100 of 6 mm thick. Two case studies used a charge-coupled device (CCD) for experimental runs. Repeating experiments were eliminated to investigate the reliability issues for which the cause-and-effect approach has been used. The authors identified three sources to ensure a strong weld: i. FSW fixtures; ii. tool health; and iii. FSW machine compliance. To reduce errors due to fixtures and tools, periodic maintenance of the spindle, mechanical fixtures, and clamping fixtures is essential. Gradual degradation of machine drives, wear and tear of meshing gears, and poor lubrication are the prime reasons for the decrease in rigidity issues of the machine. The axial force should be monitored when the machine works in a force control mode. In position control mode, the tool PD should be monitored. For both control modes, the tool tilt angle and speed are standard parameters to be monitored.

The integration of sensors with FSW machines helps collect data like force, torque, power, and temperature. Real-time data can be collected and analyzed to predict the system's performance. Signal processing integrated with ML algorithms ensures improvement in weld quality. An acoustic emission sensor with image processing techniques for monitoring FSW of AA 6082-T6 was used in [198]. In [199], the best first tree (BFT) algorithm was used to classify data collected using a vibrational analysis of the tool during FSW of AA5202 alloy based on pre-pruning and post-pruning processes. The experiment was conducted at 1400 and 1800 rp, with a 30 mm/min constant feed rate. A piezo-electric type accelerometer was used to measure the vibration from the tool in the FSW machine. Twelve datasets were extracted and given as inputs to the BFT algorithm for training purposes. Post-pruning the best first tree showed a better classification accuracy of 93.0736%. The authors used a support vector machine (SVM) to classify the weld images produced with FSW of Al 2024 alloy. A maximally stable extremal region algorithm was applied for feature extraction from weld images. With an accuracy of 95.8%, the retrieved features were used as inputs in the SVM training to distinguish between good and bad welding.

4.1. Force Measurement

FSW tools experience axial, longitudinal, and lateral forces. An axial force is generated by lifting the tool during the plunge condition when it begins rotating inside the workpiece and is opposed by the applied axial force via the tool shoulder. The FSW tool generates longitudinal power when it moves in a linear direction. Asymmetric flow occurs around the tool due to the interaction between lateral and axial forces [75,200]. The force and torque measurement of the tool is essential for three reasons: large torque relates to more power for the process, enhancement in tool wear and deformation with an increase in load, and tool wear leads to a fault in the weld and deterioration in joint properties [201,202]. As per the literature, there are two positions wherein sensors were placed: i. on top of the workbench and ii. on the spindle, tool, or head of the tool machine. The major downside of a force sensor is the dependence on welding conditions like RS, plunge depth, and TS [197,203]. Over a period, to address rising uncertainties, an adaptive PID controller can be used. The torque sensor is a better predictor of tool position. This was found to be due to a continuous increase in torque throughout the welding process, irrespective of the increase or decrease in axial force. Axial force and RS are the most critical parameters for measuring torque and force during the process.

In Zuluaga-Posada et al. [204], a novel force-measuring device based on the Ulrich methodology was designed and developed to measure axial force. The authors explored two possible concepts were i. the sensor could be placed directly on the spindle or ii. the entire system could be placed on the machine workbench. The novel device developed had two load cells, additional support for balance, and a flat ball bearing combined with a frame. There was a provision for adding one more load cell to measure the traverse force. Experiments were performed with 36 different parametric combinations viz. RS: 600 to 1600 rpm, TS: 40 to 140 mm/min, plunge speed: 30 mm/min, tilt angle: 0°, and dwell time of 20 s. The maximum axial force was observed during the plunge state, and stable values were seen during the dwell and weld stage. Radiographic inspection of the specimen revealed tunnel and wormhole defects. Fleming et al. [205] discussed force sensors (Kistler dynamometer) to determine the position of a tool during welding. A box and whisker plot was used to record the axial forces against tool offsets at each trial. A general regression neural network trained with the signals captured and predicted the forces. A total of 30 welds with different welding parameters were treated as inputs to the network, and forces were the output of the network. The network predicted an absolute error and standard deviation for each sample equal to 0.42 mm and 0.508 mm. The application of force and torque sensors in determining defects occurring during the FSW process was investigated by Das et al. [202,206]. Welding of AA1100 alloy (thickness: 6 mm) experiments (L_9 experiments: RS: 815–1500 rpm, traverse speed: 63–132 mm/min) were carried out to obtain butt joint configuration. SS316 material was used as the welding tool. Eddy current sensors were used to collect the signals from the spindle motor and feed motor, and a voltage sensor was used to manage the spindle motor's voltage signals. A noncontact laser tacho probe was used to acquire the tool RS signal. Regression models produced the best fit with 0.9998 for UTS and 0.9781 for YS. The spindle motor current signal was more effective in predicting UTS and YS. In [207], discrete wavelet transform was used to detect faults (defects) using force and torque signals during the FSW process. Welding was performed on 2.5 mm thickness AA1100 aluminum alloy. The force signals were divided into three levels using a Daubechis wavelet of order 4. A strain gauge sensor was applied in z-the direction to acquire the load data. Meridian filters were used to filter the raw sensor data before utilizing the discrete wavelet transform technique to disintegrate it. Surface defects were observed in the weld, which was performed at an RS of 500 rpm, a feed rate of 50 mm/min, 0° tilt angle, and 0.05 mm PD, resulting in a 603.06 N load.

A parametric study and force analysis of the AA6063 joint were investigated by Arya et al. [208]. A compression-type load cell was used to monitor the vertical and horizontal forces, and an S-type load cell was used. It was found that sheer force increases while plunging, indicating that the material beneath the FSW tool was softened. The force increased with an increase in PD, implying rubbing of the tool shoulder with the base plate. Square pins produced less vertical force in comparison with triangular and cylindrical profiles. The specimens were welded at an RS of 1000, 1200, and 1400 rpm and a TS of 30, 45, and 60 mm/min. An L_9 orthogonal array was used for optimization in their study. The experiments at 1200 rpm and 60 mm/min welding speed showed a more significant impact and tensile strength. In [209], experiments (RS: 600–1500 rpm, TS: 100–200 mm/min) were carried out with a square pin profile to obtain AA5052-H34 joints. A mathematical model was used to determine the tool forces (piezoelectric dynamometer) and analyze process dynamics. Heat input increased with RS, resulting in reduced yield stress. The maximum radial force for all combinations of process parameters occurred at 45° of the welding direction.

The observations made from the above literature review on force and torque measurement are as follows: force and torque measurements are essential in analyzing energy consumption and determining tool life and weld properties. The analysis also shows that pin profile configurations, PD, RS, TS, and DT, directly influence joint properties and forces generated.

4.2. Temperature Measurement

Temperature is an essential factor that affects the process. Pyrometers, thermocouples, and resistance temperature detectors (RTDs) can measure temperature. The microstructure developed during the welding process is directly influenced by temperature evolution. The welding temperature is transient. Fehrenbacher et al. [210] developed a closed-loop control for automating the welding process by varying the RS, and De Backer et al. [211] used a PI controller by considering RS as the parameter. RS had a greater influence on temperature measurements. In [212], the temperature sensors (thermocouple embedded: tool, workpiece, and between the tool and workpiece) were located at different places during the FSW process. Stir zones in the weld were the hottest part of the weld. Thermocouples embedded in workpieces and beneath the area of the rotating pin were the standard temperature measurement methods. Uncertainty in temperature data was recorded from the thermocouple due to rotating pin and plastic deformation at the stirring zone. There is also a possibility of a change in the position of the thermocouple at the weld center [213]. In [214], k-type thermocouples were embedded between the tool–workpiece interface and recorded the transient tool temperature. The thermocouple produced localized temperature values in nondestructive testing. The ASTM E-1461 modification of the laser flash method was used for the investigation.

Wire-type thermocouples wrapped in a stainless-steel sheath were used to create tool-embedded temperature-sensing equipment [210] including weld zone closed-loop control and wireless data acquisition system implementation. The voltage pulse was used as an input to the laser in a continuous mode at a maximum power output of 200 W. The oscilloscope was used to read the temperature sensor and laser pulse data. The Seebeck effect was used to measure the temperature (chromel–alumel K-type thermocouple) of the turning tool in the turning process [215] and at the tool–material interface of two dissimilar metals of FSW parts [216]. The approach was calibrated for a single tool–workpiece combination, and a Seebeck coefficient of 12 V/K was seen. The coating of the copper/tool interface was reported to influence TWT measurement significantly. Incorporating correction factors enhanced the measurement accuracy. A comparison between numerical and experimentally measured values showed that TWT measured temperature was 60 to 90 K less than the modeled one. This method was found to be suitable for online temperature control. Due to geometric changes in the tool, the technique effectively determined the temperature change at the interface.

Experiments were performed to examine the tool–workpiece interface temperature on the weld quality [217]. A real-time wireless temperature closed-loop control system was used to monitor the tool temperature between the tool shoulder and workpiece interface. Thermocouples were mounted in holes (0.8 mm diameter using EDM method) of the specimen for direct contact between the tip of the thermocouple and the workpiece material. At an angular resolution of 17–41°, various spindle speeds, and a 250 Hz sampling rate, the system captured 8.8 to 21 measurements per rotation of the tool. Tool temperature was recorded between the tool shoulder and workpiece interface. The effect of PD, travel speed, spindle speed, and thermal boundary conditions on weld quality was investigated in three studies. Butt joints possessing 175 mm length were made between two AA606-T6 workpieces. A total of 29 welding experiments with full factorial matrices were conducted in the second study. In the third study, butt welds on backing plates (steel, Ti, Cu) were performed. The authors observed that interface temperatures strongly affect the weld. The interface temperature was influenced by spindle speed and thermal boundary conditions (UTS ranging from 25% to 76% of parent material). The approach successfully detected and prevented welds with poor weld quality due to insufficient shoulder and workpiece contact. The backing plate affected the weld quality due to different interface temperatures. This altered the thermal boundary conditions, which could be regulated by adjusting other process parameters using a temperature control system.

Residual stresses alter the microstructure, fatigue life, and corrosion resistance. In [218], laser-assisted FSW and cold FSW helped minimize residual stresses in butt-welded AA5754-H111 plates. Eddy current testing was used to examine the FSW joint [219]. The acoustoelastic technique was applied with frequencies of 3.5 MHz and 5 MHz along the longitudinal direction of a weld joint in FSW of 7050-T7451 aluminum alloy [220]. The authors developed a quadratic equation to estimate the temperature of AZ80A Mg joints [221]. A numerical solution was performed using COMSOL software version 5.2. Experimental and simulated data were compared for verification. The experimental work carried out at traversing speeds: 0.5–3 mm/s, force: 3–5 kN, and RS: 500–1000 rpm was found to have linear contributions equal to 32.82%, 41.65%, and 21.76%, respectively. Both experimental and simulation results showed a dominant effect with traversing speed. The generated temperature contour graphs showed the maximum peak temperature to be 368 °C. This was caused by the high RS and axial force values and low TS, resulting in sound-quality welds. In [222], numerical investigations were conducted to determine the influence of parameters (RS, TS, and axial force) on AlSi304L stainless steel. The process was modeled as a 3D non-Newtonian fluid, with heat input calculated from friction between the tool and plate and plastic deformation. ANSYS-fluent simulations and experimental data were compared against thermocouple measurements. The numerical analysis revealed wormholes and flashes. TS was observed to be an essential factor in the formation of wormholes.

The main objective of performing numerical investigation studies is to reduce the cost incurred in conducting experiments and to determine the temperatures at different welded zones. Temperature measurements are essential and directly influence the evolution of microstructures (helps control the grain size and reduce residual stresses) and, in turn, the mechanical properties of welded joints.

4.3. Vibration and Acoustic Measurement

Acoustic sensors are more effective than vibration sensors in detecting higher frequencies [197]. A threshold above 45 dB resulted in a higher frequency of AE signals in 100–270 kHz [223]. Acoustic sensors are preferred over vibration sensors due to the high-frequency phenomenon that could help monitor the defects. A challenging task involves handling vast amounts of data during the monitoring process. In [223], experiments were conducted to monitor acoustic emissions and examine the SS316 material-based tool pin profile (triangular, circular, and square) effect on the tensile strength of the AA6063-T6 joint. Three experiments were conducted with each tool for preset conditions (traverse speed: 40 mm/min, spindle speed: 1000 rpm, and PD of 0.3 mm) for measurement consistency. Time and frequency domains were computed to monitor the process. The square tool pin profile resulted in a higher strength of 196 MPa due to more tool pin edges, high amplitude, and long duration. Acoustic emission parameters (total hits, rise time, and acoustic energy signals) increased tensile strength by 175–200 MPa.

In [224], the AE technique was applied for in-process monitoring (mounting two AE sensors on both sides of the butt joint at 70 mm apart from the butt line) by applying the Fourier transformation method and determining the reason for the lack of contact between the tool shoulder and workpiece. Couplant was used to provide an excellent acoustic path. A Bandpass filter was used to reduce mechanical noise and collect signals in the 10–400 kHz range, utilizing a preamplifier of 40 dB gain. Two different frequency ranges were observed during the process. At low frequencies (100–170 kHz), the temperature and thermal stresses increased with an increase in power spectral density (PSD). PSD was amplified at a higher frequency (220–260 kHz) when the workpiece material temperature reached the melting point. Wavelet transformation was used to detect the change in shoulder and workpiece contact due to a sudden peak in the plot. The short-time Fourier transform could provide little information on the thermomechanical conditions of the weld. The wavelet transform was used to analyze the time–frequency characteristics of AE signals (collected using two AE sensors mounted 70 mm apart along the butt line and weld direction) and features related to tool movement states and AA6061 alloy weld quality [225]. Silicon rubber was used as an AE couplant. A frequency of 20 kHz was applied to filter the mechanical noises. Daubechies wavelets were used to nullify the signals. The friction between the tool and material and the materials' thermoactivated deformation were the sources of the AE signals. The band energy variation during welding provided a more specific indication of the effects caused by gaps. The other process monitoring techniques include a machine vision system. Machine vision systems use pattern recognition algorithms on the set of digital images and determine the process effects. Process monitoring is an essential aspect of producing high-quality products, and there is potential for integrating ML, ANNs, and signal conditioning techniques to obtain optimized values.

4.4. Summary

The following observations were made:

- Workpiece material, tool material, and backing plate are material parameters that are kept constant.
- When the machine works in a force control mode, axial force should be monitored in a control mode position, and the tool PD should be monitored. For both control modes, the tool tilt angle and speed are common parameters to be monitored.
- The FSW tool experiences axial, longitudinal, and lateral forces. During the plunge state, when the tool starts rotating inside the workpiece, an axial force is generated, lifting the tool, which is opposed by the applied axial force via the tool's shoulder. The linear motion of the tool results in a longitudinal force on the FSW tool. The combination of longitudinal and axial forces results in lateral force, leading to an asymmetric flow around the tool.
- It can be concluded that RS is the most important parameter for temperature measurement.
- The most common method of temperature measurement found in the literature was using embedded thermocouples inside the workpiece and near the rotating pin area.
- Spindle speed and thermal boundary conditions strongly affected the joint interface temperature.

Acoustic sensors are preferred over vibration sensors due to high-frequency phenomena. Acoustic sensors in FSW have been used to monitor gap defects and change processes to different tool profiles. A major challenge involves in handling big data generated during the monitoring process. Table 7 shows some of the work performed in the field of process measurement of the FSW process.

Table 7. Sensors and process measurements in FSW.

Objective of the work: Force data followed by two ML techniques to assess weld quality.	[226]
Sensors used: Load cell.	
Material: AA6061.	
Experiment: A total of 42 experiments with a total of 64 samples were fabricated. One ML technique was used for the assessment of weld quality. 1. Time–frequency domain analysis using discrete wavelet transform. 2. Coefficients of the first level were extracted from the force signal, and an ANN was applied. 3. It consists of eight hidden neurons. Another ML technique was used to predict the controlled parameters to determine weld defect occurrence. 1. A genetic algorithm was used. 2. Minimum absolute error (MAE) was used to correlate between predicted and actual outputs. 3. It consisted of 10 hidden neurons. 4. Overall 70% training, 20% validation, and 10% testing. 5. Models were trained using the backpropagation algorithm.	
Process Measurement: • Sampling rate: 10 Hz. • Data acquired from the sensor was sent to a cloud server. • Client-to-server data transfer was performed by socket programming. • Input parameters to the ML model were current signals extracted from the spindle and feed motors. • Predicted parameters: 2633 rpm, 56–81 mm/min traverse speed resulting in UTS of 210 MPa.	
Results: • Real-time predicted values: 600 rpm, 250 mm/min. • The mean prediction error from ML models was 7.7%. • The acquisition time for 64 samples = 8 s, program execution time = 0.53 s, and execution of one feedback loop = 8.53 s.	
Objective of the work: Cloud-based remote monitoring of the process to determine weld defects.	[227]
Sensors used: Force and torque sensors using load cell.	
Material: AA6061.	
Experiment: Experiments were conducted in three phases: initial process parameters (two samples were made), optimum process parameters, and multi-sensor approach over a single sensor. • Phase 1: 600 rpm, 150 mm/min. Desired UTS value = 210 MPa. • Phase 2: 1000 rpm, 150 mm/min. Desired UTS value = 240 MPa. • Phase 3: three samples were welded, 600 rpm, 150 mm/min. Desired UTS value = 210 MPa. • ANN with eight hidden neurons was selected for predicting the UTS of the weld. • The backpropagation algorithm was used to train the networks. • Mean square error (MSE) was used to validate the ANN model. • The weld samples made were divided into four segments for conducting the study for phase 1, three segments for phase 2.	
Process Measurement: • The load cell was integrated into the FSW machine to acquire force and torque data. • The data collected from sensors using data acquisition card NI 6211 were saved in a cloud server. • Time-controlled 4:1 multiplexer was used to record the force, torque, power, and marker value. Outputs: the multiplexer's output is connected to the TCP write block's input. • Remote monitoring with server-side GUI. • The data acquisition rate was 10 Hz. • Transmitting data using TCP/IP at a rate of eight samples per second. • The dataset consisted of 64 samples of each sensor. • Discrete wavelet transform extracted the data from the sensors. • Image processing and ML techniques applied to monitor weld quality with appropriate feedback	

Table 7. *Cont.*

Results: First Phase: I. Sample 1: Segment 1: flash, voids, and rough surfaces were observed at 600 rpm, 150 mm/min. Segments 2, 3, and 4: the clear surface was observed progressing along the length of the specimen. a. Segment 2: 735 rpm, 153 mm/min. UTS: actual value = 170.74 MPa, predicted value = 176 MPa, error = −3.08%. b. Segment 3: 1912 rpm, 57 mm/min. UTS: actual value = 191.98 MPa, predicted value = 202 MPa, error = −5.21%. c. Segment 3: 2166 rpm, 215 mm/min. UTS: actual value = 198 MPa, predicted value = 208 MPa, error = −5.05%. II. Sample 2: Segment 1: a rough surface and voids were observed at 600 rpm, 250 mm/min. Segments 2 and 3: the clear surface was observed progressing along the length of the specimen. a. Segment 2: 1212 rpm, 50 mm/min. UTS: actual value = 193.84 MPa, predicted value = 201 MPa, error = −3.69%. b. Segment 3: 2000 rpm, 100 mm/min. UTS: actual value = 197.59 MPa, predicted value = 208 MPa, error = −5.26%. Second Phase: Segment 1: smooth surface observed at 1000 rpm, 150 mm/min. Segment 2: smoothness increased along the length of the specimen at 1610 rpm, 58 mm/min. UTS: actual value = 193.8 MPa, predicted value = 208 MPa, error = −7.32%. a. To validate, the sample was welded with a predicted value of UTS kept in the range of 230–240 MPa at 1000 rpm, 150 mm/min. Samples welded were defect-free and void-free. The authors concluded that a band of desired UTS value ensures a defect-free model and its performance. Third Phase: • Three welds. One weld with data acquired from the force sensor, one weld from the torque sensor, and one from the power sensor. The number of predictions was more with a single sensor. • With multiple sensors, the prediction error was less. Compensation of the other two sensors in case of one sensor fails.	
The objective of the work: Measure temperature at multiple locations of the tool and determine peak temperature and temperature changes at the advancing and retracting sides.	[228]
Sensors used: Tool–workpiece thermocouple.	
Material: AA6082-T6.	
Experiment: • Three thermocouples were inserted inside the tool. • A 400 rpm clockwise rotation, 2° tilt angle, 18.6 mm PD, 200 mm/min traverse speed over 30 mm, and 40 kN force for the remaining part of the weld. • TWT temperature = 587 °C.	
Process Measurement: • Standard N-type thermocouple of 1 mm diameter mounted at three locations: tool shoulder outer diameter, on probe tip, and transition from shoulder to probe. • Data transmission was performed through a three-channel slip ring to acquire the thermocouple and TWT signal. • A passive first-order low-pass filter (LP Filter) of 2.3 Hz bandwidth was used for the TWT signal. • Synchronization of the angular position of the tool with temperature signals. • A total of 75 measurement samples are recorded per rotation.	
Results: • Periodic variation in temperature oscillations of thermocouple for each tool revolution. • The highest temperature was recorded at the retreating side of the tool. • The difference between the hot and cold points was recorded at shoulder outer diameter. • TWT temperature increased drastically from the start to the end of the weld; however, the thermocouple measurements did not show a similar trend	
The objective of the work: To gain insight into dissimilar welding with force and temperature evolution.	[229]
Sensors used: K-type thermocouple placed at HAZ of advancing and retreating side at 7 mm from the weld center line.	
Material: AA2219-O and AA7475-T761.	
Experiment: • Cylindrical tool pin, RS = 710 rpm, TS = 160, 200, 250 mm/min, tilt angle = 2.5°.	
Process Measurement: Using a customized data acquisition device, real-time values of temperature and traverse force were collected and shown in relation to the distance.	

Table 7. *Cont.*

Results: • The advancing side results in higher heat and plastic deformation. • High TS causes high longitudinal force due to high flow stresses, high strain rate and low temperature. • Peak temperatures of 218, 189 and 162 °C were observed at 160, 200, and 250 mm/min on the advancing side of HAZ and the retreating side peak temperatures decreased to 191, 151 and 141 °C.

5. Industry 5.0 and the Digital Twin Framework

5.1. Industry 5.0

The origin and progress of industrial evolution have transformed manufacturing dynamics and taken the world into a new dimension of technological innovation. The focus is now on sustainable development, wherein systems are oriented more toward societal needs. Industry 5.0 comes with a fresh approach to solving problems like pollution and carbon emissions and emphasizes sustainability. Collaboration between autonomous machines and people is part of Industry 5.0. Figure 17 illustrates how Industry 5.0 is interpreted. The tri-dimension architecture used to implement Industry 5.0 is shown in Figure 18.

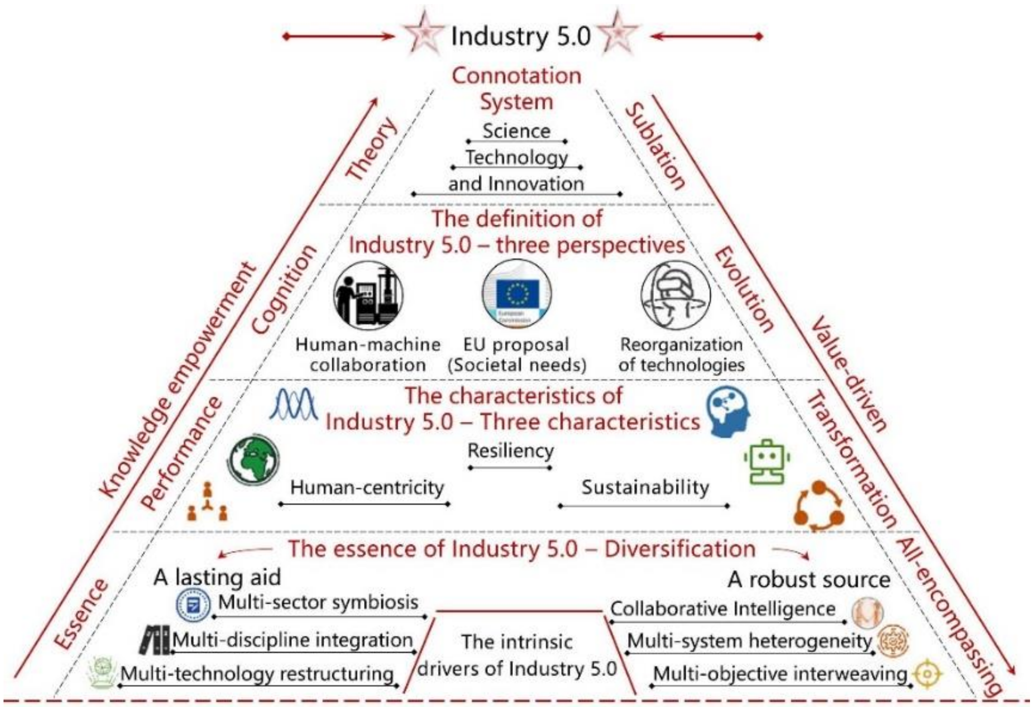

Figure 17. Connotation system of Industry 5.0 [230].

Industry 5.0 reduces the repetitive tasks of human workers, and intelligent manufacturing helps people protect their designs and technology by saving them in the cloud and using them from various places [231]. Using wireless technology, intelligent manufacturing can help the industry achieve the objectives of Industry 5.0 [232]. Safety management through cyber–physical systems and cyber-physical human systems are the core elements in Industry 5.0 relating to human-centered manufacturing. This focuses on communication between humans, machines, and the environment. Wang et al. [233] approached the safety management system of Industry 5.0 based on digital twin technology and discussed the challenges associated with the safety management system. The authors have also proposed an approach to solve the challenges associated with it. Integration of a vision system with semantic web technology can identify unsafe states. del Real Torres et al. [234] explained the deep reinforcement learning (DRL) approach for the Industry 4.0 and 5.0 frameworks.

It can help machine vision systems identify unsafe states and adapt to scenarios. Cloud infrastructure supports IoT platforms to manage edge devices like autonomous robots on the shop floor. To reduce the volume of data accessed from servers, Industry 5.0 can reduce the volume of data transferred to a server. In the case of FSW, sensor data and process parameters can be saved in servers and used by machines in other locations. Industry 5.0 must develop specialized software linking workplaces, collaborative robots, AI, and IoT. For efficient adoption of Industry 5.0, stringent laws and guidelines must be framed. Data security and privacy are other vital concerns to consider before adopting 5.0.

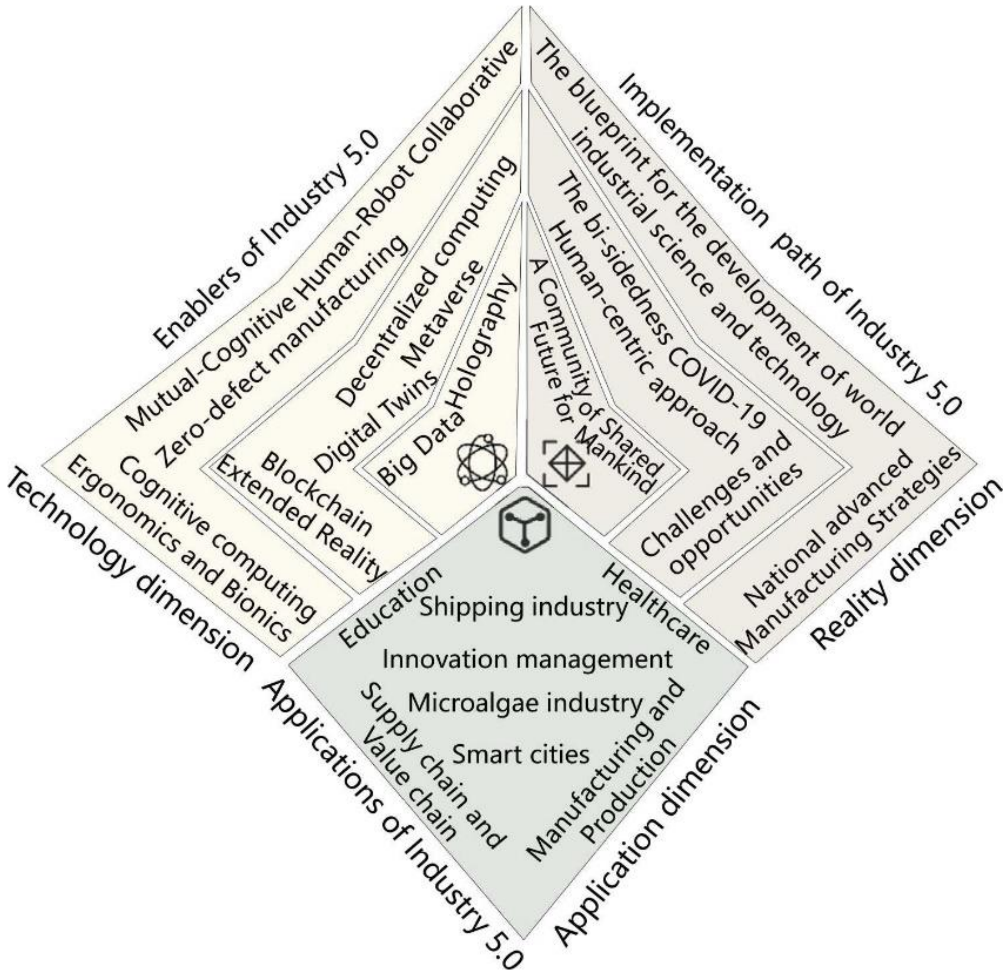

Figure 18. Tri-dimension architecture of Industry 5.0 implementation [230].

5.2. Digital Twin (DT) Technology

A DT is a strategy for a real-time, digital, and precise replica of the manufacturing process. It has two worlds: the digital world and the real world. The real world turns digital tools for modeling and simulation into physical models and virtual representations of the real world with remote monitoring. The virtual world involves task assignments, planning, and synchronization with robotic systems. The real world comprises synchronization, communication, and tracking of multifunctional technologies in manufacturing and assembly systems [235]. DT has been applied to over 50 fields and efficiently implements safe management infrastructure.

In [236], DT was applied for temperature measurement during the FSW process. To evaluate the in-progress 3D temperature field, the scientists created an iterative cyber–physics fusion algorithm by combining recorded temperature data (collected viz. K-type thermocouples) with a moving heat source analysis of AA2024 and AA6061 alloys. DT technology has also been applied to monitor the welding force signals using a strain gauge integrated into the FSW machine [237]. The experiment built DT links to the machine utilizing sensory data that resides in the cloud. DT was used to create a dashboard that tracks welding noise levels, tool health, motor health, and hydraulic oil state. AA6061 alloy welding experiments were conducted with sets of parameters including 1200 rpm RS and 50 mm/min TS, 2° tilt angle, and 0.1 mm PD, and the spindle power was analyzed. Sensors such as flow rate and capacitive-type oil were used during experiments. Five tools (weld material stuck on the tool, pin-less, half-broken pin, cracked, and a normal tool) were used during experimentation. The developed system was found to be adequate to demonstrate the in situ monitoring of FSW machines.

5.3. Summary

Industry 5.0 helps solve the problem of a mismatch between manufacturing and social needs. Cloud computing, blockchain, big data analytics, and IoT are technologies related to Industry 5.0. The challenges associated with Industry 5.0 included embedding human-centric values in 5.0 technologies, symbiosis of different technologies, data security, and other relevant information to establish trust in the 5.0 ecosystem. Some of the future work includes a combination of DT with augmented reality (AR), representing the integration of real and virtual environments. The prior identification of problems during a virtual stage in DT can increase the efficiency of the production line. Both technologies are at the initial stage and have a lot of scope for developing sophisticated systems focusing on sustainable development and human-centric needs.

6. Conclusions and Future Scope

FSW is a suitable alternative to fusion-based welding techniques for producing parts with minimal defects. RS, TS, PD, and tilt angle are the vital process parameters for FSW. Amongst them, RS is the most significant parameter. Optimization determines the best possible combination of various process parameters to fabricate parts with better mechanical properties. Taguchi, RSM and FD, AI and ML, and ANN techniques have been used for FSW. Taguchi, response surface methodology, and factorial design are categorized under the statistical optimization approach, while machine learning algorithms are categorized under AI-based optimization. Researchers have also implemented hybrid and multi-objective and hybrid optimization techniques for optimization. In the case of FSW, temperature plays an important role. Researchers predominantly used thermocouples to monitor temperature evolution. Force and torque measurements have been performed using load cells to determine the effect of vertical load on the mechanical properties and vibration, and acoustic sensors for frequencies measured during the FSW process. Data acquired from the sensors have been analyzed with AI and ML algorithms to determine the optimum parameters. Future research should concentrate on developing real-time feedback systems with multiple sensors and multi-objective optimization techniques for determining the best-suited parameters for FSW.

Below, some future work for the FSW process are highlighted, referencing microstructure and mechanical properties, simulation and modeling, optimization techniques, commercialization and economics of the process, process monitoring, and advanced sensor and artificial intelligence enable technologies:

1. FSW specimen evaluation of microstructure and mechanical characteristics regarding corrosion and wear resistance, fracture toughness, and fatigue strength is essential for widening the present applications.
2. High-temperature plastic flow behavior and mechanical properties for dissimilar welding can be studied further.
3. Analyzing characteristics of FSW, namely, corrosion resistance, fatigue life, and residual stresses.
4. Analyzing the impact of peak temperature on the microstructure and mechanical characteristics of hard materials using numerical and analytical methods.

5. Further studies can be carried out in FSW of stainless steel to develop functions for variable friction and slip rate coefficients.
6. Another topic to research is analyzing the impact of pre- and post-weld treatments for steels.
7. More research must address the effects of various bobbin tool profiles on steel.
8. In simulation modeling, the parameters connected to the tool pin, such as temperature, torque, and maximum shear stress, can reduce the incidence of poor welds by 4%. Techniques like ANNs and image processing enhance the procedure.
9. Thick non-ferrous, ferrous, and metal-based composite materials can be manufactured using temperature simulation-based optimization techniques.
10. Objective determination of the weights on each response should be included instead of subjectively choosing the values.
11. Validation of datasets generated using ML models in the prediction of UTS.
12. In situ data from the thermal camera generates temperature data during the welding process and sends it as an input to ML, and ANN models will drastically improve performance.
13. Integration of FSW with AI and ML techniques for quality inspection and monitoring is another area to explore to obtain better quality and defect-free joints.
14. The impact of welding conditions on the cost of the process can be another area to explore.
15. Economic feasibility of research for FSW of steels and process commercialization.
16. Multi-sensor feedback system coupled with multi-objective optimization techniques for better weld specimens and improved mechanical properties.
17. Based on the work by [172], where the force model was developed for the square profile tool, similar works can be carried out for other tool profiles.
18. Improvement in camera motion for better image extraction and processing.
19. The determination of a relationship between measured data and weld quality can be further explored.
20. An innovative ML-based model for determining tool conditioning monitoring systems (TCMSs) to predict tool wear and breakage measurement systems.
21. Optimization of feature extraction, data reduction in void deduction, and defect identification in welded samples using image segmentation techniques.
22. As most of the DRL work is simulation-based, implementing DRL into the FSW process by selecting an appropriate algorithm and defining guidelines is an important task.
23. Implementing digital twin technology for in situ process monitoring and establishing a steady and stable production line for multiple FSW machines.
24. Implementation of cloud-based platform controls.
25. The design and deployment of 5G technologies into the FSW process is another area that can be explored.
26. Integrate Industry 4.0 and 5.0 concepts and framework in the FSW process.
27. Application of an online monitoring system for vibration, torque, and temperature measurement and converting the design into a digital system by implementing IoT.
28. FSW of polymers can be explored. This can include the effect of PD or axial force on the morphology and strength of the joint, the relationship between physical properties and optimal parameters, and the quantification of the heat generated and its effect on the weld.

Author Contributions: Conceptualization, D.A.P.P., M.A.H. and A.K.S.; methodology, A.K., M.A.H., A.K.S. and M.P.G.C.; software, D.Y.P. and K.G.; formal analysis, M.P.G.C., D.Y.P. and K.G.; investigation, D.A.P.P., M.A.H. and A.K.S.; resources, A.K., M.A.H., A.K.S. and D.A.P.P.; data curation, M.P.G.C., D.Y.P. and K.G.; writing—original draft preparation, A.K., M.A.H., A.K.S. and D.A.P.P.; writing—review and editing, M.P.G.C., D.Y.P. and K.G.; supervision, A.K.S. and M.A.H. All authors have read and agreed to the published version of the manuscript.

Funding: This research received no external funding.

Data Availability Statement: The data will be made available upon request to the authors.

Conflicts of Interest: The authors declare no conflict of interest.

Nomenclature

ABC: Artificial Bee Colony
ACO: Ant Colony Optimization
ANFIS: Artificial Neuro-fuzzy Inference System
ANN: artificial neural network
ANOVA: Analysis of Variance
AS: advancing side
BM: base metal
BPA: backpropagation algorithm
C1: correction factor
CCD: central composite design
CDR: continuous dynamic recrystallization
DDR: discontinuous dynamic recrystallization
DFA: desirability function approach
DoE: design of experiment
DTR: decision tree regression
EBW: electron beam welding
FEM: finite element model
FSW: friction stir welding
GA: genetic algorithm
GPR: Gaussian progression regression
GRA: Grey Relational Analysis
GTAW: gas–tungsten arc welding
HAZ: heat-affected zone
HS: harmony search
IS: impact strength
IE: impact energy
JA: Jaya algorithm
JE: joint efficiency
L-M: Levenberg–Marquardtt
LR: linear regression
MAE: mean absolute error
MH: microhardness
MI: maximum iterations
ML: machine learning
MR: mutation rate
MSE: mean square error
NCGA: neighborhood cultivation genetic algorithm
NZ: nugget zone
OA: orthogonal array
Pc: probability of crossover
PA-FSW: plasma-assisted friction stir welding
PCBN: polycrystalline cubic boron nitride
PCD: polycrystalline diamond
PD: plunge depth
PR: polynomial regression
PS: population size
PSO: particle swarm optimization
PWHT: post-weld heat treatment
RFR: random forest regression
RS: rotational side
RSM: response surface methodology
SA: simulated annealing
SAW: submerged arc welding
SEM: scanning electron microscope
SVM: support vector machine
SVR: support vector regression
SZ: stir zone SS: swarm size
TLBO: teaching–learning-based optimization
TMAZ: thermomechanical affected zone
TS: tensile strength
UTS: ultimate tensile strength

References

1. Mohan, D.G.; Wu, C.S. A Review on Friction Stir Welding of Steels. *Chin. J. Mech. Eng.* **2021**, *34*, 137. [CrossRef]
2. Chularis, A.A.; Rzaev, R.A.; Valisheva, A.G.; Kogan, V.V. Joining of Steels to Aluminum and its Alloys by Friction Stir Welding. *Met. Sci. Heat Treat.* **2021**, *62*, 738–747. [CrossRef]
3. Ahmed, M.M.Z.; El-Sayed Seleman, M.M.; Fydrych, D.; Cam, G. Friction stir welding in the aerospace industry: The current progress and state-of-the-art review. *Materials* **2023**, *16*, 2971. [CrossRef]
4. Kashaev, N.; Ventzke, V.; Cam, G. Prospects of laser beam welding and friction stir welding processes for aluminum airframe structural applications. *J. Manuf. Process.* **2018**, *36*, 571–600. [CrossRef]
5. Cam, G.; Ipekoglu, G. Recent developments in joining of aluminium alloys. *Int. J. Adv. Manuf. Technol.* **2017**, *91*, 1851–1866. [CrossRef]
6. Kavathia, K.; Badheka, V. Application of Friction Stir Welding (FSW) in Automotive and Electric Vehicle. In *Recent Advances in Mechanical Infrastructure*; Parwani, A.K., Ramkumar, P., Abhishek, K., Yadav, S.K., Eds.; Lecture Notes in Intelligent Transportation and Infrastructure Book Series; Springer: Singapore, 2022. [CrossRef]
7. Martin, J.; Wei, S. Friction Stir Welding Technology for Marine Applications. In *Friction Stir Welding and Processing VIII*; Mishra, R.S., Mahoney, M.W., Sato, Y., Hovanski, Y., Eds.; Springer: Cham, Switzerland, 2015. [CrossRef]
8. İpekoğlu, G.; Erim, S.; Kıral, B.G.; Çam, G. Investigation into the effect of temper condition on friction stir weldability of AA6061 Al-alloy plates. *Kov. Mater.* **2013**, *51*, 155–163. [CrossRef]

9. Çam, G.; Javaheri, V.; Heidarzadeh, A. Advances in FSW and FSSW of dissimilar Al-alloy plates. *J. Adhes. Sci. Technol.* **2023**, *37*, 162–194. [CrossRef]
10. El-Sayed, M.M.; Shash, A.Y.; Abd-Rabou, M.; ElSherbiny, M.G. Welding and processing of metallic materials by using friction stir technique: A review. *J. Adv. Join. Process.* **2011**, *3*, 100059. [CrossRef]
11. Singh, K.; Singh, G.; Singh, H. Review on friction stir welding of magnesium alloys. *J. Magnes. Alloys* **2018**, *6*, 399–416. [CrossRef]
12. Cui, L.; Peng, Z.; Chang, Y.; He, D.; Cao, Q.; Guo, X.; Zeng, Y. Porosity, microstructure and mechanical property of welded joints produced by different laser welding processes in selective laser melting AlSi10Mg alloys. *Opt. Laser Technol.* **2022**, *150*, 107952. [CrossRef]
13. Ipekoglu, G.; Cam, G. Formation of weld defects in cold metal transfer arc welded 7075-T6 plates and its effect on joint performance. *IOP Conf. Ser. Mater. Sci. Eng.* **2019**, *629*, 012007. [CrossRef]
14. Cam, G. Prospects of producing aluminum parts by wire arc additive manufacturing (WAAM). *Mater. Today Proc.* **2022**, *62*, 77–85. [CrossRef]
15. Liu, F.; Dong, Y.; Tan, Z.; Wang, H.; Tan, C.; Chen, B.; Song, X. Mechanism analysis on suppressing porosity in laser-MIG hybrid welding of aluminum alloy via external magnetic field. *J. Manuf. Process.* **2023**, *101*, 1124–1135. [CrossRef]
16. Deng, A.; Chen, H.; Zhang, Y.; Liu, Y.; Yang, X.; Zhang, B. Effect of filler materials on the porosity formation of aluminum alloy by laser welding with filler wire. *Opt. Laser Technol.* **2023**, *159*, 109000. [CrossRef]
17. Wang, L.; Liu, Y.; Yang, C.; Gao, M. Study of porosity suppression in oscillating laser-MIG hybrid welding of AA6082 aluminum alloy. *J. Mater. Process. Technol.* **2021**, *292*, 117053. [CrossRef]
18. Chen, L.; Wang, C.; Xiong, L.; Zhang, X.; Mi, G. Microstructural, porosity and mechanical properties of lap joint laser welding for 5182 and 6061 dissimilar aluminum alloys under different place configurations. *Mater. Des.* **2020**, *191*, 108625. [CrossRef]
19. Zhang, Y.N.; Cao, X.; Larose, S.; Wanjara, P. Review of tools for friction stir welding and processing. *Can. Met. Q.* **2012**, *51*, 250–261. [CrossRef]
20. Simar, A.; Bréchet, Y.; de Meester, B.; Denquin, A.; Gallais, C.; Pardoen, T. Integrated modeling of friction stir welding of 6xxx series Al alloys: Process, microstructure and properties. *Prog. Mater. Sci.* **2012**, *57*, 95–183. [CrossRef]
21. Prabhakar, D.A.P.; Shettigar, A.K.; Herbert, M.A.; Gowdru, C.M.P.; Pimenov, D.Y.; Giasin, K.; Prakash, C. A comprehensive review of friction stir techniques in structural materials and alloys: Challenges and trends. *J. Mater. Res. Technol.* **2022**, *20*, 3025–3060. [CrossRef]
22. Andrade, D.G.; Leitão, C.; Dialami, N.; Chiumenti, M.; Rodrigues, D.M. Analysis of contact conditions and its influence on strain rate and temperature in friction stir welding. *Int. J. Mech. Sci.* **2021**, *191*, 106095. [CrossRef]
23. Andrade, D.G.; Leitão, C.; Dialami, N.; Chiumenti, M.; Rodrigues, D.M. Modelling torque and temperature in friction stir welding of aluminium alloys. *Int. J. Mech. Sci.* **2020**, *182*, 105725. [CrossRef]
24. Leitãoa, C.; Louro, R.; Rodrigues, D.M. Using torque sensitivity analysis in accessing Friction Stir Welding/Processing conditions. *J. Mater. Process. Technol.* **2012**, *212*, 2051–2057. [CrossRef]
25. Leal, R.M.; Leitãoa, C.; Loureiroa, A.; Rodrigues, D.M.; Vilaca, P. Material flow in heterogeneous friction stir welding of thin aluminium sheets: Effect of shoulder geometry. *Mater. Sci. Eng. A* **2008**, *498*, 384–391. [CrossRef]
26. Simões, F.; Rodrigues, D.M. Material flow and thermo-mechanical conditions during Friction Stir Welding of polymers: Literature review, experimental results and empirical analysis. *Mater. Des.* **2014**, *59*, 344–351. [CrossRef]
27. Kalita, K.; Burande, D.; Ghadai, R.K.; Chakraborty, S. Finite Element Modelling, Predictive Modelling and Optimization of Metal Inert Gas, Tungsten Inert Gas and Friction Stir Welding Processes: A Comprehensive Review. *Arch. Comput. Methods Eng.* **2023**, *30*, 271–299. [CrossRef]
28. Shen, Z.; Ding, Y.; Gerlich, A.P. Advances in friction stir spot welding. *Crit. Rev. Solid State Mater. Sci.* **2020**, *45*, 457–534. [CrossRef]
29. Ogunsemi, B.T.; Abioye, T.E.; Ogedengbe, T.I.; Zuhailawati, H. A review of various improvement strategies for joint quality of AA 6061-T6 friction stir weldments. *J. Mater. Res. Technol.* **2021**, *11*, 1061–1089. [CrossRef]
30. Mofid, M.A.; Abdollah-Zadeh, A.; Ghaini, F.M. The effect of water cooling during dissimilar friction stir welding of Al alloy to Mg alloy. *Mater. Des.* **2012**, *36*, 161–167. [CrossRef]
31. Eren, B.; Guvenc, M.A.; Mistikoglu, S. Artificial intelligence applications for friction stir welding: A review. *Met. Mater. Int.* **2021**, *27*, 193–219. [CrossRef]
32. Smith, I.J.; Lord, D.D. *FSW Patents-A Stirring Story*; SAE Transactions; SAE International: Warrendale, PA, USA, 2007; pp. 772–780. [CrossRef]
33. Birdi, A.; Procha, A.; Brar, A.S.; Kumar, R.; Kumar, S. Effect of tool pin profile on mechanical characteristics of friction stir welded al alloys: A critical review. *Int. Res. J. Nat. Sci.* **2019**, *1*, 15–21. Available online: https://www.scienceresearchjournals.org/IRJNST/volume-1%20issue-5.html (accessed on 2 February 2023).
34. Kumar, A.; Raju, L.S. Influence of tool pin profiles on friction stir welding of copper. *Mater. Manuf.* **2012**, *27*, 1414–1418. [CrossRef]
35. Mishra, R.S.; Ma, Z.Y. Friction stir welding and processing. *Mater. Sci. Eng. R Rep.* **2005**, *50*, 1–78. [CrossRef]
36. Kamal, S.; Parthiban, V.; Puthilibai, G.; Thirumal Azhagan, M.; Kamal, N.; Senthil, T.S.; Yishak, S. Investigation on tensile behaviour of different weld joints through Taguchi approach. *Adv. Mater. Sci. Eng.* **2022**, *2022*, 5258014. [CrossRef]
37. Babalola, S.A.; Dutta, S.; Murmu, N.C.; Akinnuli, B.O. In-situ process reliability monitoring strategy for friction stir welding machine. *Mater. Today Proc.* **2022**, *66*, 3883–3889. [CrossRef]

38. Ehiasarian, A.; Purandare, Y.; Sugumaran, A.; Hovsepian, P.; Hatto, P.; de Backer, J. Improving the Quality of Friction Stir Welds in Aluminium Alloys. *Coatings* **2021**, *11*, 539. [CrossRef]
39. Nandan, R.; DebRoy, T.; Bhadeshia, H.K.D.H. Recent advances in friction-stir welding–process, weldment structure and properties. *Prog. Mater. Sci.* **2008**, *53*, 980–1023. [CrossRef]
40. MohammadiSefat, M.; Ghazanfari, H.; Blais, C. Friction Stir Welding of 5052-H18 aluminum alloy: Modeling and process parameter optimization. *J. Mater. Eng. Perform.* **2021**, *30*, 1838–1850. [CrossRef]
41. Mijajlović, M.; Milčić, D. Analytical model for estimating the amount of heat generated during friction stir welding: Application on plates made of aluminium alloy 2024 T351. In *Welding Processes*; IntechOpen: London, UK, 2012; pp. 247–274. [CrossRef]
42. Dressler, U.; Biallas, G.; Mercado, U.A. Friction stir welding of titanium alloy TiAl6V4 to aluminium alloy AA2024-T3. *Mater. Sci. Eng. A* **2009**, *526*, 113–117. [CrossRef]
43. Li, B.; Zhang, Z.; Shen, Y.; Hu, W.; Luo, L. Dissimilar friction stir welding of Ti–6Al–4V alloy and aluminum alloy employing a modified butt joint configuration: Influences of process variables on the weld interfaces and tensile properties. *Mater. Des.* **2014**, *53*, 838–848. [CrossRef]
44. Albannai, A.I. Review the Common Defects in Friction Stir Welding. *Int. J. Sci. Technol. Res.* **2020**, *9*, 318–329.
45. Mao, Y.; Yang, P.; Zhang, W.; Li, N.; Nie, H.; Lin, D.; Ke, L. Improving tensile-shear properties of friction stir lap welded dissimilar Al/Mg joints by eliminating hook defect and controlling interfacial reaction. *Chin. J. Aeronaut.* **2022**, *36*, 257–267. [CrossRef]
46. Wang, X.; Xiao, Y.; Shi, L.; Zhai, M.; Wu, C.; Chen, G. Revealing the mechanism of tool tilting on suppressing the formation of void defects in friction stir welding. *J. Mater. Res. Technol.* **2023**, *25*, 38–54. [CrossRef]
47. Lunetto, V.; De Maddis, M.; Russo Spena, P. Similar and Dissimilar Lap Friction Stir Welding of Titanium Alloys: On the Elimination of the Hook Defect. *Int. J. Adv. Manuf. Technol.* **2023**, *126*, 3417–3435. [CrossRef]
48. Chen, S.; Zhang, H.; Jiang, X.; Yuan, T.; Han, Y.; Li, X. Mechanical properties of electric assisted friction stir welded 2219 aluminum alloy. *J. Manuf. Process.* **2019**, *44*, 197–206. [CrossRef]
49. Zamani, S.M.M.; Behdinan, K.; Razfar, M.R.; Fatmehsari, D.H.; Mohandesi, J.A. Studying the effects of process parameters on the mechanical properties in friction stir welding of Al-SiC composite sheets. *Int. J. Adv. Manuf. Technol.* **2021**, *113*, 3629–3641. [CrossRef]
50. Elangovan, K.; Balasubramanian, V. Influences of pin profile and rotational speed of the tool on the formation of friction stir processing zone in AA2219 aluminium alloy. *Mater. Sci. Eng.* **2007**, *459*, 7–18. [CrossRef]
51. Sahali, M.A.; Aini, A.; Bouzit, L.; Himed, L.; Benaissa, B. Experimental modeling and multi-objective optimization of friction stir welding parameters of AA 3004 aluminum alloy. *Int. J. Adv. Manuf. Technol.* **2023**, *124*, 1229–1244. [CrossRef]
52. Oakes, T.; Landers, R.G. Design, and implementation of a general tracking controller for friction stir welding processes. In Proceedings of the 2009 American Control Conference, St. Louis, MO, USA, 10–12 June 2009; pp. 5576–5581. [CrossRef]
53. Safeen, M.W.; Russo Spena, P.; Buffa, G.; Campanella, D.; Masnata, A.; Fratini, L. Effect of position and force tool control in friction stir welding of dissimilar aluminum-steel lap joints for automotive applications. *Adv. Manuf.* **2020**, *8*, 59–71. [CrossRef]
54. Zhao, X.; Kalya, P.; Landers, R.G.; Krishnamurthy, K. Path force control for friction stir welding processes. *Dyn. Syst. Control. Conf.* **2008**, *43352*, 87–94.
55. Jaffarullah, M.S.; Low, C.Y.; Shaari, M.S.B.; Jaffar, A. A review of force control techniques in friction stir process. *Procedia Comput. Sci.* **2015**, *76*, 528–533. [CrossRef]
56. Shettigar, A.K.; Manjaiah, M. Friction Stir Welding—An Overview. In *Advanced Manufacturing Technologies*; Gupta, K., Ed.; Materials Forming, Machining and Tribology Book Series; Springer: Cham, Switzerlad, 2017. [CrossRef]
57. Noreña, E.; Zuluaga, M.; Hoyos, E.; Montoya, Y. Model-based proposal of a control strategy for friction stir welding. In Proceedings of the 2019 IEEE 4th Colombian Conference on Automatic Control (CCAC), Medellin, Colombia, 15–16 October 2019; pp. 1–6. [CrossRef]
58. Zhao, S.; Bi, Q.; Wang, Y. An axial force controller with delay compensation for the friction stir welding process. *Int. J. Adv. Manuf. Technol.* **2016**, *85*, 2623–2638. [CrossRef]
59. Teng, L.; Lu, X.; Luan, Y.; Sun, S. Predicting axial force in friction stir welding thick 2219 aluminum alloy plate. *Int. J. Adv. Manuf. Technol.* **2023**, *126*, 1025–1034. [CrossRef]
60. Rabe, P.; Schiebahn, A.; Reisgen, U. Force feedback-based quality monitoring of the friction stir welding process utilizing an analytic algorithm. *Weld. World* **2021**, *65*, 845–854. [CrossRef]
61. Guan, W.; Cui, L.; Liang, H.; Wang, D.; Huang, Y.; Li, M.; Li, X. The response of force characteristic to weld-forming process in friction stir welding assisted by machine learning. *Int. J. Mech. Sci.* **2023**, *253*, 108409. [CrossRef]
62. Rabe, P.; Schiebahn, A.; Reisgen, U. Deep learning approaches for force feedback based void defect detection in friction stir welding. *J. Adv. Join. Process.* **2022**, *5*, 100087. [CrossRef]
63. Karlsson, M.; Bagge Carlson, F.; Holmstrand, M.; Robertsson, A.; de Backer, J.; Quintino, L.; Johansson, R. Robotic friction stir welding–seam-tracking control, force control and process supervision. *Ind. Robot. Int. J. Robot. Res. Appl.* **2023**, *50*, 722–730. [CrossRef]
64. Xiao, J.; Wang, M.; Liu, H.; Liu, S.; Zhao, H.; Gao, J. A constant plunge depth control strategy for robotic FSW based on online trajectory generation. *Robot. Comput. Integr. Manuf.* **2023**, *80*, 102479. [CrossRef]
65. Schmidt, H.; Hattel, J.; Wert, J. An analytical model for the heat generation in friction stir welding. *Model. Simul. Mater. Sci. Eng.* **2003**, *12*, 143. [CrossRef]

66. Song, M.; Kovacevic, R. Thermal modeling of friction stir welding in a moving coordinate system and its validation. *Int. J. Mach. Tools Manuf.* **2003**, *43*, 605–615. [CrossRef]
67. Amara, K.; Badji, R.; Bouabdallah, M.; Cheniti, B.; Aissani, M.; Haddad, A.; Ziouche, A. Effect of PWHT on microstructure and corrosion resistance of the nugget zone in AZ31 friction stir weld. *Int. J. Adv. Manuf. Technol.* **2022**, *123*, 2757–2769. [CrossRef]
68. Tiwari, A.; Pankaj, P.; Suman, S.; Singh, P.; Biswas, P.; Pal, S.; Rao, A.G. Effect of plasma preheating on weld quality and tool life during friction stir welding of DH36 steel. *Proc. Inst. Mech. Eng.* **2021**, *235*, 1458–1472. [CrossRef]
69. Moshwan, R.; Yusof, F.; Hassan, M.A.; Rahmat, S.M. Effect of tool rotational speed on force generation, microstructure and mechanical properties of friction stir welded Al–Mg–Cr–Mn (AA 5052-O) alloy. *Mater. Des.* **2015**, *66*, 118–128. [CrossRef]
70. Salloomi, K.N. Defect monitoring in dissimilar friction stir welding of aluminum alloys using Coupled Eulerian-Lagrangian (CEL) finite element model. *Adv. Mater. Process.* **2022**, *16*, 301. [CrossRef]
71. West, P.; Shunmugasamy, V.C.; Usman, C.A.; Karaman, I.; Mansoor, B. Part I.: Friction stir welding of equiatomic nickel titanium shape memory alloy–microstructure, mechanical and corrosion behavior. *J. Adv. Join. Process.* **2021**, *4*, 100071. [CrossRef]
72. Subramanya, P.; Amar, M.; Arun, S.; Mervin, H.; Shrikantha, R. Friction stir welding of Aluminium matrix composites–A Review. *MATEC Web Conf.* **2018**, *144*, 03002. [CrossRef]
73. Mendes, N.; Neto, P.; Loureiro, A.; Moreira, A.P. Machines and control systems for friction stir welding: A review. *Mater. Des.* **2016**, *90*, 256–265. [CrossRef]
74. Sorensen, C.D.; Nelson, T.W. Friction stir welding of ferrous and nickel alloys. *Frict. Stir Weld. Process.* **2007**, *44073*, 111–121. [CrossRef]
75. Rai, R.; De, A.; Bhadeshia, H.K.D.H.; DebRoy, T. Friction stir welding tools. *Sci. Technol. Weld. Join.* **2011**, *16*, 325–342. [CrossRef]
76. Prabhu, R.S.B.; Shettigar, A.K.; Patel, G.C.M.; Herbert, M.; Rao, S.S. Influence of process variables on joint attributes of friction stir welded aluminium matrix composite. *Adv. Mater. Process.* **2022**, *8*, 1550–1559. [CrossRef]
77. Shettigar, A.K.; Salian, G.; Herbert, M.; Rao, S. Microstructural characterization and hardness evaluation of friction stir welded composite AA6061-4.5 Cu-5SiC (Wt.%). *Def. Sci. J.* **2013**, *63*, 429. [CrossRef]
78. Fernandez, G.J.; Murr, L.E. Characterization of tool wear and weld optimization in the friction-stir welding of cast aluminum 359 + 20% SiC metal-matrix composite. *Mater. Charact.* **2004**, *52*, 65–75. [CrossRef]
79. Feng, A.H.; Xiao, B.L.; Ma, Z.Y. Effect of microstructural evolution on mechanical properties of friction stir welded AA2009/SiCp composite. *Compos. Sci. Technol.* **2008**, *68*, 2141–2148. [CrossRef]
80. Patthi, U.B.; Awang, M. Friction stir welding on aluminum 6092/sic/25p/t6 metal matrix composite: Its microstructure evolution and mechanical properties. In Proceedings of the 2011 National Postgraduate Conference, Perak, Malaysia, 19–20 September 2011; pp. 1–6. [CrossRef]
81. Cioffi, F.; Fernández, R.; Gesto, D.; Rey, P.; Verdera, D.; González-Doncel, G. Friction stir welding of thick plates of aluminum alloy matrix composite with a high-volume fraction of ceramicreinforcement. *Compos.-A Appl.* **2013**, *54*, 117–123. [CrossRef]
82. Kalaiselvan, K.; Dinaharan, I.; Murugan, N. Characterization of friction stir welded boron carbide particulate reinforced AA6061 aluminum alloy stir cast composite. *Mater. Des.* **2014**, *55*, 176–182. [CrossRef]
83. Bahrami, M.; Dehghani, K.; Givi, M.K.B. A novel approach to develop aluminum matrix nano-composite employing friction stir welding technique. *Mater. Des.* **2014**, *53*, 217–225. [CrossRef]
84. Aonuma, M.; Nakata, K. Dissimilar metal joining of 2024 and 7075 aluminium alloys to titanium alloys by friction stir welding. *Mater. Trans.* **2011**, *52*, 948–952. [CrossRef]
85. Nguyen, Q.M.; Do, T.V.; Nguyen, V.N. A study on the microstructure, mechanical properties, and corrosion behavior for friction stir welded Ti-6Al-4V alloys. *Int. J. Mech. Eng. Robot. Res.* **2021**, *10*, 163e8. [CrossRef]
86. Han, Y.; Chen, S.; Jiang, X.; Bai, Y.; Yuan, T.; Wang, X. Effect of microstructure, texture and deformation behavior on tensile properties of electrically assisted friction stir welded Ti-6Al-4 V joints. *Mater. Charact.* **2021**, *176*, 111141. [CrossRef]
87. Eliseev, A.; Amirov, A.; Kalashnikova, T.; Vorontsov, A.; Kolubaev, E. Production of Ti–1.5 Al–1Mn Titanium Alloy Butt Joints by Friction Stir Welding. *Metals* **2021**, *11*, 1566. [CrossRef]
88. Liu, H.J.; Zhou, L.; Liu, Q.W. Microstructural characteristics and mechanical properties of friction stir welded joints of Ti–6Al–4V titanium alloy. *Mater. Des.* **2010**, *31*, 1650–1655. [CrossRef]
89. Su, Y.; Li, W.; Gao, F.; Vairis, A. Effect of FSW process on anisotropic of titanium alloy T-joint. *Mater. Manuf.* **2022**, *37*, 25–33. [CrossRef]
90. Wang, W.; Han, P.; Qiao, K.; Li, T.; Wang, K.; Cai, J.; Wang, L. Effect of the rotation rate on the low-cycle fatigue behavior of friction-stir welded AZ31 magnesium alloy. *Eng. Fract. Mech.* **2020**, *228*, 106925. [CrossRef]
91. Padmanaban, G.; Balasubramanian, V. Selection of FSW tool pin profile, shoulder diameter and material for joining AZ31B magnesium alloy–an experimental approach. *Mater. Des.* **2009**, *30*, 2647–2656. [CrossRef]
92. Xunhong, W.; Kuaishe, W. Microstructure and properties of friction stir butt-welded AZ31 magnesium alloy. *Mater. Sci. Eng. A* **2006**, *431*, 114–117. [CrossRef]
93. Sevvel, P.; Jaiganesh, V. Influence of the arrangement of materials and microstructural analysis during FSW of AZ80A & AZ91C Mg alloys. *Arch. Met. Mater.* **2017**, *62*, 1795–1801. [CrossRef]
94. Yang, J.; Wang, D.; Xiao, B.L.; Ni, D.R.; Ma, Z.Y. Effects of rotation rates on microstructure, mechanical properties, and fracture behavior of friction stir-welded (FSW) AZ31 magnesium alloy. *Met. Mater. Trans.* **2013**, *44*, 517–530. [CrossRef]

95. Tan, C.; Jiang, Z.; Li, L.; Chen, Y.; Chen, X. Microstructural evolution and mechanical properties of dissimilar Al–Cu joints produced by friction stir welding. *Mater. Des.* **2013**, *51*, 466–473. [CrossRef]
96. Dias, F.; Cipriano, G.; Correia, A.N.; Braga, D.F.O.; Moreira, P.; Infante, V. Joining of Aluminum Alloy AA7075 and Titanium Alloy Ti-6Al-4V through a Friction Stir Welding-Based Process. *Metals* **2023**, *13*, 249. [CrossRef]
97. Correia, A.N.; Santos, P.A.; Braga, D.F.; Cipriano, G.P.; Moreira, P.M.; Infante, V. Effects of processing temperature on failure mechanisms of dissimilar aluminum-to-polymer joints produced by friction stir welding. *Eng. Fail. Anal.* **2023**, *146*, 107155. [CrossRef]
98. Mustafa, S.E.; Rai, R.N.; Firoz, R. Enhancement of joint properties and reduction of intermetallics in FSW of highly dissimilar Al/Ti alloys. *Weld. World* **2023**, *67*, 1393–1410. [CrossRef]
99. Newishy, M.; Jaskari, M.; Järvenpää, A.; Fujii, H.; Abdel-Aleem, H.A. Friction Stir Welding of Dissimilar Al 6061-T6 to AISI 316 Stainless Steel: Microstructure and Mechanical Properties. *Materials* **2023**, *16*, 4085. [CrossRef] [PubMed]
100. Torabi, K.; Beygi, R.; Eisaabadi Bozchaloei, G.; da Silva, L.F.M. The Effect of Tool Rotation Speed on the Formation of Eutectic Structure during Friction Stir Welding of Aluminum to Magnesium. *Appl. Sci.* **2023**, *13*, 7133. [CrossRef]
101. Tang, J.; Shi, L.; Wu, C.; Wu, M. Development of novel double-side friction stir Z shape butt-lap welding process for dissimilar joining of 12 mm medium-thick Al/Cu plates. *Mater. Lett.* **2023**, *331*, 133445. [CrossRef]
102. Elmetwally, H.T.; Abdelhafiz, M.A.; El-Sheikh, M.N.; Abdullah, M.E. Effect of Friction Stir-Welding Tool Pin Geometry on the Characteristics of Al-Cu Joints. *Appl. Eng. Lett.* **2023**, *8*, 60–69. [CrossRef]
103. Hu, J.; Cao, F.; Shen, Y.; Guo, C.; Yang, Z. Superior strength and ductility in friction stir welded dissimilar joint of galvanized steel and Q235 steel. *CIRP J. Manuf. Sci. Technol.* **2023**, *45*, 190–199. [CrossRef]
104. Zhang, J.; Zhang, Y.; Chen, X.; Li, Z.; Huang, G.; Pan, F. Improving joint performance of friction stir welded AZ31/ AM60 dissimilar Mg alloys by double-sided welding. *Mater. Sci. Eng. A* **2023**, *882*, 145444. [CrossRef]
105. Srivastava, M.; Rathee, S.; Maheshwari, S.; Noor Siddiquee, A.; Kundra, T.K. A review on recent progress in solid state friction-based metal additive manufacturing: Friction stir additive techniques. *Crit. Rev. Solid State Mater. Sci.* **2019**, *44*, 345–377. [CrossRef]
106. Khusainov, R.M.; Sabirov, A.R.; Mubarakshin, I.I. Study of deformations field in the working zone of vertical milling machine. *Procedia Eng.* **2017**, *206*, 1069–1074. [CrossRef]
107. Zhao, J.; Duan, Y.; Xie, B.; Zhang, Z. FSW robot system dimensional optimization and trajectory planning based on soft stiffness indices. *J. Manuf. Process.* **2021**, *63*, 88–97. [CrossRef]
108. Yang, X.S. Optimization and metaheuristic algorithms in engineering. In *Metaheuristics in Water, Geotechnical and Transport Engineering*; Elsevier: Amsterdam, The Netherlands, 2013; pp. 1–23. [CrossRef]
109. Modi, V.K.; Desai, D.A. Review of Taguchi Method, Design of Experiment (DOE) & Analysis Of Variance (ANOVA) For Quality Improvements through Optimization in Foundry. *J. Emerg. Technol. Innov. Res.* **2018**, *5*, 184–194. Available online: https://www.jetir.org/papers/JETIR1801035.pdf (accessed on 4 January 2023).
110. Jagdev, H.S.; Browne, J.; Keogh, J. Manufacturing Process Optimisation—A Survey of Techniques. In Proceedings of the Twenty-Eighth International: Matador Conference, Macmillan Education, Manchester, UK, 18–19 April 1990; pp. 205–215. [CrossRef]
111. Korgal, A.; Upadhyaya, S.; Anilkumar, T. Grain refinement of aluminium 4032 alloy with the impact of vibration using Taguchi technique and analysis of variance (ANOVA). *Mater. Today Proc.* **2022**, *54*, 507–512. [CrossRef]
112. Chauhan, A.; Kumar, S. Optimization of Friction Stir Welding Parameters for Similar Base Material Combinations. In *Advances in Engineering Materials: Select Proceedings of FLAME*; Springer: Berlin/Heidelberg, Germany, 2021; pp. 665–675. [CrossRef]
113. Krishna, G.G. Improving joint strength of the friction stir welding of dissimilar aluminium alloy by using coating technique. *Sādhanā* **2022**, *47*, 7. [CrossRef]
114. Ismail, A.; Zulkipli, F.N.; Awang, M.; Ab Rahman, F.; Khalid, P.Z.M.; Baharudin, B.A. Optimum Welding Parameters for Friction Stir Welded AA6063 Pipe Butt Joint Using the Taguchi Method. *Trans. Marit. Sci.* **2021**, *10*, 404–413. [CrossRef]
115. Tutum, C.C.; Hattel, J.H. Optimisation of process parameters in friction stir welding based on residual stress analysis: A feasibility study. *Sci. Technol. Weld. Join.* **2010**, *15*, 369–377. [CrossRef]
116. Panwar, R.; Chandna, P. Parameter optimization of FSW aviation-grade AA8090 using Taguchi grey relational analysis. *Aircr. Eng. Aerosp. Technol.* **2023**, *95*, 715–724. [CrossRef]
117. Seshu Kumar, G.S.V.; Kumar, A.; Rajesh, S.; Chekuri, R.B.R.; Ramakotaiah, K. An experimental study and parameter optimization of FSW for welding dissimilar 6061 and 7075 Al alloys. *Int. J. Interact. Des. Manuf.* **2023**, *17*, 215–223. [CrossRef]
118. Delir Nazarlou, R.; Arghavanian, R.; Omidbakhsh, F. The effect of pin shape on the corrosion behaviour of friction stir welded 1080 aluminium alloy. *Adv. Mater. Process.* **2023**, *9*, 507–518. [CrossRef]
119. El-Zathry, N.E.; Hassan, A.I.; El-Betar, A.A.; Sabry, I. Optimization of friction stir welding AA6082-T6 parameters using analysis of variance and grey relational analysis. *J. Phys. Conf. Ser.* **2022**, *2299*, 012015. [CrossRef]
120. Sefene, E.M.; Tsegaw, A.A. Temperature-based optimization of friction stir welding of AA 6061 using GRA synchronous with Taguchi method. *Int. J. Adv. Manuf. Technol.* **2022**, *119*, 1479–1490. [CrossRef]
121. Ubaid, M.; Bajaj, D.; Mukhopadhyay, A.K.; Siddiquee, A.N. Friction stir welding of thick AA2519 alloy: Defect elimination, mechanical and micro-structural characterization. *Met. Mater. Int.* **2020**, *26*, 1841–1860. [CrossRef]

122. Abd Elnabi, M.M.; Abdel-Mottaleb, M.M.; Osman, T.A.; El Mokadem, A. Influence of friction stir welding parameters on metallurgical and mechanical properties of dissimilar AA5454–AA7075 aluminum alloys. *J. Mater. Res. Technol.* **2019**, *8*, 1684–1693. [CrossRef]
123. Vijayan, S.; Raju, R.; Subbaiah, K.; Sridhar, N.; Rao, S.R.K. Friction stir welding of Al–Mg alloy optimization of process parameters using Taguchi method. *Exp. Tech.* **2010**, *34*, 37–44. [CrossRef]
124. Prasad, M.D.; Kumar Namala, K. Process parameters optimization in friction stir welding by ANOVA. *Mater. Today Proc.* **2018**, *5*, 4824–4831. [CrossRef]
125. Khalkhali, A.; Sarmadi, M.; Sarikhani, E. Investigation on the best process criteria for lap joint friction stir welding of AA1100 aluminum alloy via Taguchi technique and ANOVA. *Proc. Inst. Mech. Eng.* **2017**, *231*, 329–342. [CrossRef]
126. Kumar, G.S.V.S.; Kumar, A.; Rajesh, S.; Chekuri, R.B.R.; Sundaramurthy, V.P. Experimental and thermal investigation with optimization on friction stir welding of nylon 6A using Taguchi and microstructural analysis. *Adv. Mech. Eng.* **2021**, *13*, 16878140211050737. [CrossRef]
127. Arof, S.; Diyanah, N.; Yaakop, N.; Mawby, P.; Arof, H. Advanced Engineering for Processes and Technologies. *AIP Conf. Proc.* **2019**, *2195*, 020032. [CrossRef]
128. Balamurugan, S.; Jayakumar, K.; Subbaiah, K. Influence of friction stir welding parameters on dissimilar joints AA6061-T6 and AA5052-H32. *Arab. J. Sci. Eng.* **2021**, *46*, 11985–11998. [CrossRef]
129. El-Wazery, M.S.; Mabrouk, O.M.; El Sissy, A.R. Optimization of ultrasonic-assisted friction stir welded using taguchi approach. *Int. J. Eng.* **2022**, *35*, 213–219. [CrossRef]
130. Mahesha, C.R.; Suprabha, R.; Kumar, N.M.; Kosanam, K.; Anandaram, H.; Naidu, S.R.M.; Chakravarthi, M.K.; Govindarajan, V. Effect of Friction Stir Welding on the Mechanical and Microstructural Behaviour of AA7075 Aluminium Alloy. *Adv. Mater. Sci. Eng.* **2022**, *2022*, 2788479. [CrossRef]
131. Kumar, R.R.; Singh, A.; Kumar, A.; Ansu, A.K.; Kumar, A.; Kumar, S.; Chakravarthi, M.K.; Singh, D. Enhancement of friction stir welding characteristics of alloy AA6061 by design of experiment methodology. *Int. J. Interact. Des. Manuf.* **2022**, *16*, 1–13. [CrossRef]
132. Madhusudan, M.; Shanmuganatan, S.P.; Kurse, S. Optimization of Wear Parameters on Friction Stir Welded Dissimilar Aluminium Joints. *J. Inst. Eng. (India) Ser. D* **2022**, *103*, 1–16. [CrossRef]
133. Vijayakumar, S.; Manickam, S.; Seetharaman, S.; Rao, T.; Pounraj, D.; Pydi, H.P. Examination of friction stir-welded AA 6262/5456 joints through the optimization technique. *Adv. Mater. Sci. Eng.* **2022**, *2022*, 4527595. [CrossRef]
134. Muthurasu, P.; Kathiresan, M. Optimization and analysis of microstructural friction stir welded AA5083 grade aluminium alloy. *J. Ceram. Process. Res.* **2021**, *22*, 697–704. [CrossRef]
135. Sivasubramaniam, S.; Ramanathan, T.; Shanmugham, N.; Sekar, K. Investigation of Welding Process Parameters in Friction Stir Welding of AA1100 Alloy Using Taguchi Technique. *Chiang Mai J. Sci.* **2022**, *49*, 1416–1427. [CrossRef]
136. Ahmed, M.M.; Touileb, K.; El-Sayed Seleman, M.M.; Albaijan, I.; Habba, M.I. Bobbin Tool Friction Stir Welding of Aluminum: Parameters Optimization Using Taguchi Experimental Design. *Materials* **2022**, *15*, 2771. [CrossRef]
137. Alam, M.P.; Sinha, A.N. Optimization of process parameters of friction stir welding using desirabilityfunction analysis. *Weld. Int.* **2022**, *36*, 129–143. [CrossRef]
138. Raja, R.; Parthiban, A.; Nandha Gopan, S.; Degefa, D. Investigate the process parameter on the friction stir welding of dissimilar aluminium alloys. Adv. *Mater. Sci. Eng.* **2022**, *2022*, 4980291. [CrossRef]
139. Sasikala, G.; Jothiprakash, V.M.; Pant, B.; Subalakshmi, R.; Thirumal Azhagan, M.; Arul, K.; Praveen Kumar, S. Optimization of process parameters for friction stir welding of different aluminum alloys AA2618 to AA5086 by Taguchi method. *Adv. Mater. Sci. Eng.* **2022**, *2022*, 3808605. [CrossRef]
140. Thirumalai, R.; Karthick, S.; Giriraj, M. Microstructural analysis and optimization of welding parameters for AA1100 welded plates. *J. Ceram. Process. Res.* **2022**, *23*, 221–227. [CrossRef]
141. Zhou, L.; Luo, L.Y.; Wang, R.; Zhang, J.B.; Huang, Y.X.; Song, X.G. Process parameter optimization in refill friction spot welding of 6061 aluminum alloys using response surface methodology. *J. Mater. Eng. Perform.* **2018**, *27*, 4050–4058. [CrossRef]
142. Patel, G.C.M.; Krishna, P.; Parappagoudar, M.B. Squeeze casting process modeling by a conventional statistical regression analysis approach. *Appl. Math. Model.* **2016**, *40*, 6869–6888. [CrossRef]
143. Patel, G.C.M.; Shettigar, A.K.; Parappagoudar, M.B. A systematic approach to model and optimize wear behaviour of castings produced by squeeze casting process. *J. Manuf. Process.* **2018**, *32*, 199–212. [CrossRef]
144. Mallieswaran, K.; Padmanabhan, R.; Balasubramanian, V. Friction stir welding parameters optimization for tailored welded blank sheets of AA1100 with AA6061 dissimilar alloy using response surface methodology. *Adv. Mater. Process.* **2018**, *4*, 142–157. [CrossRef]
145. Vignesh, S.; Dinesh Babu, P.; Nalla Mohamed, M.; Martin Vinoth, S.; Surya, G.; Dinesh, S. Investigation on the process parameters of double-sided friction stir welded AA6082-T 6 joints with different tool pins using response surface methodology. In *Advances in Manufacturing Processes: Select Proceedings of ICEMMM 2018*; Springer: Singapore, 2019; pp. 309–319. ISBN 978-981-13-1723-1.
146. Akhai, S.; Srivastava, P.; Sharma, V.; Bhatia, A. Investigating weld strength of AA8011-6062 alloys joined via friction-stir welding using the RSM approach. *J. Phys. Conf. Ser.* **2021**, *1950*, 012016. [CrossRef]
147. Zhang, C.Y.; Chen, Q.D.; Jean, M.D. Optimization of the welding properties of friction stir weld butt joints using the response surface method based on taguchi's design. *Strength Mater.* **2022**, *54*, 267–280. [CrossRef]

148. Phanphet, S.; Sukprasert, N.; Wangmai, A.; Bangphan, S.; Bangphan, P. Application of factorial design to study the effect of moisture and rice of varieties on the production of Paddy Husker Machine. In Proceedings of the World Congress on Engineering, London, UK, 4–6 July 2018; Volume 2. [CrossRef]
149. Medhi, T.; Hussain, S.A.I.; Roy, B.S.; Saha, S.C. An intelligent multi-objective framework for optimizing friction-stir welding process parameters. *Appl. Soft Comput.* **2021**, *104*, 107190. [CrossRef]
150. Anand, R.; Sridhar, V.G. Microstructure and mechanical properties of interlock friction stir weld lap joint AA7475-T7 using fractional factorial design. *Proc. Inst. Mech. Eng. Part C* **2022**, *236*, 318–329. [CrossRef]
151. Senapati, P.N.; Bhoi, R.K. Characterization of Friction-Stir Welded Joints of AA1100 by Factorial Design Based Hierarchical Regression Model. *Ann. Chim. Sci. Mater.* **2020**, *44*, 271–280. [CrossRef]
152. Sahu, S.K.; Mishra, D.; Pal, K.; Pal, S.K. Multi-sensor-based strategies for accurate prediction of friction stir welding of polycarbonate sheets. *Proc. Inst. Mech. Eng. Part C* **2021**, *235*, 3252–3272. [CrossRef]
153. Bector, K.; Tripathi, A.; Pandey, D.; Butola, R.; Singari, R.M. A review on the fabrication of surface composites via friction stir processing and its modeling using ANN. In *Advances in Manufacturing and Industrial Engineering: Select Proceedings of ICAPIE 2019*; Springer: Berlin/Heidelberg, Germany, 2021; pp. 1–11. [CrossRef]
154. Patel, G.C.M.; Shettigar, A.K.; Krishna, P.; Parappagoudar, M.B. Back propagation genetic and recurrent neural network applications in modelling and analysis of squeeze casting process. *Appl. Soft Comput.* **2017**, *59*, 418–437. [CrossRef]
155. Haykin, S. *Neural Networks: A Comprehensive Foundation*; Prentice Hall: Hoboken, NJ, USA, 1998.
156. Patel, G.C.M.; Krishna, P.; Parappagoudar, M.B. An intelligent system for squeeze casting process—Soft computing-based approach. *Int. J. Adv. Manuf. Technol.* **2016**, *86*, 3051–3065.
157. Shojaeefard, M.H.; Akbari, M.; Asadi, P. Multi-objective optimization of friction stir welding parameters using FEM and neural network. *Int. J. Precis. Eng. Manuf.* **2014**, *15*, 2351–2356. [CrossRef]
158. Shojaeefard, M.H.; Behnagh, R.A.; Akbari, M.; Givi, M.K.B.; Farhani, F. Modelling and Pareto optimization of mechanical properties of friction stir welded AA7075/AA5083 butt joints using neural network and particle swarm algorithm. *Mater. Des.* **2013**, *44*, 190–198. [CrossRef]
159. Salhan, P.; Singh, R.; Jain, P.; Butola, R. Prediction of heat generation and microstructure of AA7075 friction stir welding using ANN: Effect of process parameters. *Manuf. Lett.* **2022**, *32*, 5–9. [CrossRef]
160. Vangalapati, M.; Balaji, K.; Gopichand, A. ANN modeling and analysis of friction welded AA6061 aluminum alloy. *Mater. Today Proc.* **2019**, *18*, 3357–3364. [CrossRef]
161. Senthilnathan, T.; Balachandar, K. Prediction of mechanical properties and optimization of process parameters in friction-stir-welded dissimilar aluminium alloys. *World J. Eng.* **2020**, *17*, 519–526. [CrossRef]
162. Jamalian, H.M.; Eskandar, M.T.; Chamanara, A.; Karimzadeh, R.; Yousefian, R. An artificial neural network model for multi-pass tool pin varying FSW of AA5086-H34 plates reinforced with Al2O3 nanoparticles and optimization for tool design insight. *CIRP J. Manuf. Sci. Technol.* **2021**, *35*, 69–79. [CrossRef]
163. D'Orazio, A.; Forcellese, A.; Simoncini, M. Prediction of the vertical force during FSW of AZ31 magnesium alloy sheets using an artificial neural network-based model. *Neural. Comput. Appl.* **2019**, *31*, 7211–7226. [CrossRef]
164. Maleki, E. Artificial neural networks application for modeling of friction stir welding effects on mechanical properties of 7075-T6 aluminum alloy. *IOP Conf. Ser. Mater. Sci. Eng.* **2015**, *103*, 012034. [CrossRef]
165. Ghetiya, N.D.; Patel, K.M. Prediction of tensile strength in friction stir welded aluminium alloy using artificial neural network. *Proc. Technol.* **2014**, *14*, 274–281. [CrossRef]
166. Okuyucu, H.; Kurt, A.; Arcaklioglu, E. Artificial neural network application to the friction stir welding of aluminum plates. *Mater. Des.* **2007**, *28*, 78–84. [CrossRef]
167. Dutt, A.K.; Sindhuja, K.; Reddy, S.V.N.; Kumar, P. Application of Artificial Neural Network to Friction Stir Welding Process of AA7050 Aluminum Alloy. In *Advances in Industrial Automation and Smart Manufacturing*; ICAIASM; Springer: Singapore, 2019; Volume 2021, pp. 407–414. [CrossRef]
168. Dehabadi, V.M.; Ghorbanpour, S.; Azimi, G. Application of artificial neural network to predict Vickers microhardness of AA6061 friction stir welded sheets. *J. Cent. South Univ.* **2016**, *23*, 2146–2155. [CrossRef]
169. Darzi Naghibi, H.; Shakeri, M.; Hosseinzadeh, M. Neural network and genetic algorithm based modeling and optimization of tensile properties in FSW of AA 5052 to AISI 304 dissimilar joints. *Trans. Indian Inst. Met.* **2016**, *69*, 891–900. [CrossRef]
170. Verma, S.; Misra, J.P.; Singh, J.; Batra, U.; Kumar, Y. Prediction of tensile behavior of FS welded AA7039 using machine learning. *Mater. Today Commun.* **2021**, *26*, 101933. [CrossRef]
171. Thapliyal, S.; Mishra, A. Machine learning classification-based approach for mechanical properties of friction stir welding of copper. *Manuf. Lett.* **2021**, *29*, 52–55. [CrossRef]
172. Singh, R.; Kainthola, A.; Singh, T.N. Estimation of elastic constant of rocks using an ANFIS approach. *Appl. Soft Comput.* **2012**, *12*, 40–45. [CrossRef]
173. Monostori, L.; Márkus, A.; van Brussel, H.; Westkämpfer, E. Machine learning approaches to manufacturing. *CIRP Ann.* **1996**, *45*, 675–712. [CrossRef]
174. Chadha, U.; Selvaraj, S.K.; Gunreddy, N.; Sanjay Babu, S.; Mishra, S.; Padala, D.; Adefris, A. A survey of machine learning in friction stir welding, including unresolved issues and future research directions. *Mater. Des. Process. Commun.* **2022**, *2022*, 2568347. [CrossRef]

175. Mishra, A.; Dutta, S.B. Detection of surface defects in friction stir welded joints by using a novel machine learning approach. *Appl. Eng. Lett.* **2020**, *5*, 16–21. [CrossRef]
176. Mukherjee, I.; Ray, P.K. A review of optimization techniques in metal cutting processes. *Comput. Ind. Eng.* **2006**, *50*, 15–34. [CrossRef]
177. Rao, R.V.; Rai, D.P. Optimisation of welding processes using quasi-oppositional-based Jaya algorithm. *J. Exp. Theor. Artif. Intell.* **2017**, *29*, 1099–1117. [CrossRef]
178. Rambabu, G.; Naik, D.B.; Rao, C.V.; Rao, K.S.; Reddy, G.M. Optimization of friction stir welding parameters for improved corrosion resistance of AA2219 aluminum alloy joints. *Def. Technol.* **2015**, *11*, 330–337. [CrossRef]
179. Saeidi, M.; Manafi, B.; Besharati Givi, M.K.; Faraji, G. Mathematical modeling and optimization of friction stir welding process parameters in AA5083 and AA7075 aluminum alloy joints. *Proc. Inst. Mech. Eng. Part B* **2016**, *230*, 1284–1294. [CrossRef]
180. Kumar, A.K.; Surya, M.S.; Venkataramaiah, P. Performance evaluation of machine learning based-classifiers in friction stir welding of Aa6061-T6 alloy. *Int. J. Interact. Des. Manuf.* **2023**, *17*, 469–472. [CrossRef]
181. Anandan, B.; Manikandan, M. Machine learning approach for predicting the peak temperature of dissimilar AA7050-AA2014A friction stir welding butt joint using various regression models. *Mater. Lett.* **2022**, *325*, 132879. [CrossRef]
182. Aghbashlo, M.; Peng, W.; Tabatabaei, M.; Kalogirou, S.A.; Soltanian, S.; Hosseinzadeh-Bandbafha, H.; Lam, S.S. Machine learning technology in biodiesel research: A review. *Prog. Energy Combust. Sci.* **2021**, *85*, 100904. [CrossRef]
183. Sahu, P.K.; Kumari, K.; Pal, S.; Pal, S.K. Hybrid fuzzy-grey-Taguchi based multi weld quality optimization of Al/Cu dissimilar friction stir welded joints. *Adv. Manuf.* **2016**, *4*, 237–247. [CrossRef]
184. Pitchipoo, P.; Muthiah, A.; Jeyakumar, K.; Manikandan, A. Friction stir welding parameter optimization using novel multi objective dragonfly algorithm. *Int. J. Light. Mater. Manuf.* **2021**, *4*, 460–467. [CrossRef]
185. Nadikudi, B.K.B. Parametric optimization of friction stir welding process parameters of dissimilar welded joints using grey relational analysis and desirability function approach. *World J. Eng.* **2022**, *20*, 609–617. [CrossRef]
186. Van, A.L.; Nguyen, T.T. Optimization of friction stir welding operation using optimal taguchi-based ANFIS and genetic algorithm. *Stroj. Vestn./J. Mech. Eng.* **2022**, *68*, 424–438. [CrossRef]
187. Anjinappa, C.S.; Alamri, S.; Afzal, A.; Razak Kaladgi, A.; Saleel, C.A.; Hasan, N.; Saleh, B. Response surface, neural network, and experimental approach to optimize process parameters and characterization of Al-Mg alloy by friction stir welding. *Adv. Mech. Eng.* **2022**, *14*, 16878132221120460. [CrossRef]
188. Ambekar, M.; Kittur, J. Multiresponse optimization of friction stir welding process parameters by an integrated WPCA-ANN-PSO approach. *Mater. Today Proc.* **2020**, *27*, 363–368. [CrossRef]
189. Wakchaure, K.N.; Thakur, A.G.; Gadakh, V.; Kumar, A. Multi-objective optimization of friction stir welding of aluminium alloy 6082-T6 Using hybrid Taguchi-Grey relation analysis-ANN method. *Mater. Today Proc.* **2018**, *5*, 7150–7159. [CrossRef]
190. Al-Mahasneh, M.; Aljarrah, M.; Rababah, T.; Alu'datt, M. Application of hybrid neural fuzzy system (ANFIS) in food processing and technology. *Food Eng. Rev.* **2016**, *8*, 351–366. [CrossRef]
191. Wahid, M.A.; Masood, S.; Khan, Z.A.; Siddiquee, A.N.; Badruddin, I.A.; Algahtani, A. A simulation-based study on the effect of underwater friction stir welding process parameters using different evolutionary optimization algorithms. *Proc. Inst. Mech. Eng. Part C* **2020**, *234*, 643–657. [CrossRef]
192. Gopalakrishnan, R.; Kanakaraj, D.A.; Dennis, B.P.R.; Rajendran, A.R. Multi-response Optimization of FSW Process Parameters of ZE42 Alloy Using RSM-Based Grey Relational Analysis. In *Intelligent Manufacturing and Energy Sustainability: Proceedings of ICIMES*; Springer: Singapore, 2020; pp. 125–133. [CrossRef]
193. Ghangas, G.; Singhal, S. Modelling and optimization of process parameters for friction stir welding of armor alloy using RSM and GRA-PCA approach. *Mater. Res. Express* **2018**, *6*, 026553. [CrossRef]
194. Chaluvaraju, B.V.; Afzal, A.; Vinnik, D.A.; Kaladgi, A.R.; Alamri, S.; Tirth, V. Mechanical and corrosion studies of friction stir welded nano Al_2O_3 reinforced Al-Mg matrix composites: RSM-ANN modelling approach. *Symmetry* **2021**, *13*, 537.
195. Jaypuria, S.; Mahapatra, T.R.; Jaypuria, O. Metaheuristic tuned ANFIS model for input-output modeling of friction stir welding. *Mater. Today Proc.* **2019**, *18*, 3922–3930. [CrossRef]
196. Kandavalli, S.R.; Khan, A.M.; Iqbal, A.; Jamil, M.; Abbas, S.; Laghari, R.A.; Cheok, Q. Application of sophisticated sensors to advance the monitoring of machining processes: Analysis and holistic review. *Int. J. Adv. Manuf. Technol.* **2023**, *125*, 989–1014. [CrossRef]
197. Mishra, D.; Roy, R.B.; Dutta, S.; Pal, S.K.; Chakravarty, D. A review on sensor-based monitoring and control of friction stir welding process and a roadmap to Industry 4.0. *J. Manuf. Process.* **2018**, *36*, 373–397. [CrossRef]
198. Murthy, V.; Ullegaddi, K.; Mahesh, B.; Rajaprakash, B.M. Application of image processing and acoustic emission technique in monitoring of friction stir welding process. *Mater. Today Proc.* **2017**, *4*, 9186–9195. [CrossRef]
199. Balachandar, K.; Jegadeeshwaran, R.; Gandhikumar, D. Condition monitoring of FSW tool using vibration analysis–A machine learning approach. *Mater. Today Proc.* **2020**, *27*, 2970–2974. [CrossRef]
200. Kumar, R.; Singh, K.; Pandey, S. Process forces and heat input as function of process parameters in AA5083 friction stir welds. *Trans. Nonferrous Met. Soc. China* **2012**, *22*, 288–298. [CrossRef]
201. Atharifar, H.; Lin, D.; Kovacevic, R. Numerical and experimental investigations on the loads carried by the tool during friction stir welding. *J. Mater. Eng. Perform.* **2009**, *18*, 339–350. [CrossRef]

202. Das, B.; Pal, S.; Bag, S. Design and development of force and torque measurement setup for real time monitoring of friction stir welding process. *Measurement* **2017**, *103*, 186–198. [CrossRef]
203. Gibson, B.T.; Lammlein, D.H.; Prater, T.J.; Longhurst, W.R.; Cox, C.D.; Ballun, M.C.; Strauss, A.M. Friction stir welding: Process, automation, and control. *J. Manuf. Process.* **2014**, *16*, 56–73. [CrossRef]
204. Zuluaga-Posada, M.; Hoyos, E.; Montoya, Y. Performance evaluation of a novel force measuring device for Friction Stir Welding (FSW) of aluminum alloys. *DYNA* **2019**, *86*, 150–155. [CrossRef]
205. Fleming, P.A.; Lammlein, D.H.; Wilkes, D.M.; Cook, G.E.; Strauss, A.M.; DeLapp, D.R.; Hartman, D.A. Misalignment detection and enabling of seam tracking for friction stir welding. *Sci. Technol. Weld. Join.* **2009**, *14*, 93–96. [CrossRef]
206. Das, B.; Pal, S.; Bag, S. Monitoring of friction stir welding process through signals acquired during the welding. In Proceedings of the AIMTDR 2014, Guwahati, India, 12–14 December 2014; pp. 12–14.
207. Kumar, U.; Yadav, I.; Kumari, S.; Kumari, K.; Ranjan, N.; Kesharwani, R.K.; Pal, S.K. Defect identification in friction stir welding using discrete wavelet analysis. *Adv. Eng. Softw.* **2015**, *85*, 43–50. [CrossRef]
208. Arya, H.K.; Jaiswal, D. Parametric Study and Force Analysis of Friction Stir Welded Aa-6063 Joint. *Int. J. Mech. Eng.* **2022**, *7*, 756–768. Available online: https://kalaharijournals.com/ijme-vol7-issue-jan2022.php (accessed on 16 January 2023).
209. Terra, C.S.; Silveira, J.L.L. Models for FSW forces using a square pin profile tool. *J. Manuf. Process.* **2021**, *68*, 1395–1404. [CrossRef]
210. Fehrenbacher, A.; Duffie, N.A.; Ferrier, N.J.; Pfefferkorn, F.E.; Zinn, M.R. Toward automation of friction stir welding through temperature measurement and closed-loop control. *J. Manuf. Sci. Eng.* **2011**, *133*, 051008. [CrossRef]
211. De Backer, J.; Bolmsjö, G.; Christiansson, A.K. Temperature control of robotic friction stir welding using the thermoelectric effect. *Int. J. Adv. Manuf. Technol.* **2014**, *70*, 375–383. [CrossRef]
212. Silva, A.C.F.; de Backer, J.; Bolmsjö, G. Temperature measurements during friction stir welding. *Int. J. Adv. Manuf. Technol.* **2017**, *88*, 2899–2908. Available online: https://link.springer.com/article/10.1007%2Fs00170-016-9007-4 (accessed on 12 February 2023). [CrossRef]
213. Threadgill, P.L.; Leonard, A.J.; Shercliff, H.R.; Withers, P.J. Friction stir welding of aluminium alloys. *Int. Mater. Rev.* **2009**, *54*, 49–93. [CrossRef]
214. Schmale, J.; Fehrenbacher, A.; Shrivastava, A.; Pfefferkorn, F.E. Calibration of dynamic tool–workpiece interface temperature measurement during friction stir welding. *Measurement* **2016**, *88*, 331–342. [CrossRef]
215. D'Errico; Calzavarini, R.; Settineri, L. Experiments on self-tuning regulation of cutting temperature in turning process. In Proceedings of the 1994 Proceedings of IEEE International Conference on Control and Applications, Glasgow, UK, 24–26 August 1994; pp. 1165–1169. [CrossRef]
216. de Backer, J.; Bolmsjö, G. Thermoelectric method for temperature measurement in friction stirwelding. *Sci. Technol. Weld. Join.* **2013**, *18*, 558–565. [CrossRef]
217. Fehrenbacher, A.; Duffie, N.A.; Ferrier, N.J.; Pfefferkorn, F.E.; Zinn, M.R. Effects of tool—Workpiece interface temperature on weld quality and quality improvements through temperature control in friction stir welding. *Int. J. Adv. Manuf. Technol.* **2014**, *71*, 165–179. [CrossRef]
218. Campanella, D.; Casavola, C.; Cazzato, A.; Fratini, L.; Moramarco, V.; Pappalettere, C. Residual Stress Measurement in Innovative Friction Stir Welding Processes. *Key Eng. Mater.* **2017**, *754*, 391–394. [CrossRef]
219. Brauer, H.; Otterbach, J.M.; Ziolkowski, M.; Toepfer, H.; Graetzel, M.; Bergmann, J.P. Friction stir weld inspection using the motion induced eddy current testing technique. *AIP Conf. Proc.* **2019**, *2102*, 080004. [CrossRef]
220. García Ruano, S.A.; Bertelli, F.; dos Santos, A.A., Jr. Evaluation of 7050 Aluminum Plates Joined by Friction Stir Welding Using Acoustoelastic. *ASME Int. Mech. Eng. Congr. Expo.* **2017**, *58356*, V002T02A089. [CrossRef]
221. Sevvel, P.; Babu, S.D.; Kumar, R.S. Peak Temperature Correlation and Temperature Distribution during Joining of AZ80A Mg Alloy by FSW-A Numerical and Experimental Investigation. *Stroj. Vestn./J. Mech. Eng.* **2020**, *66*, 395–407. [CrossRef]
222. da Silva, Y.C.; Oliveira Junior, F.J.; dos Santos, J.F.; Marcondes, F.; Silva, C. Numerical investigation of the influence of FSW parameters on the heat and mass transfer of austenitic stainless steels. *Weld. World* **2020**, *64*, 2019–2032. [CrossRef]
223. Subramaniam, S. Acoustic emission–based monitoring approach for friction stir welding of aluminum alloy AA6063-T6 with different tool pin profiles. *Proc. Inst. Mech. Eng. Part B* **2013**, *227*, 407–416. [CrossRef]
224. Soundararajan, V.; Atharifar, H.; Kovacevic, R. Monitoring and processing the acoustic emission signals from the friction-stir-welding process. *Proc. Inst. Mech. Eng. Part B* **2006**, *220*, 1673–1685. [CrossRef]
225. Chen, C.; Kovacevic, R.; Jandgric, D. Wavelet transform analysis of acoustic emission in monitoring friction stir welding of 6061 aluminum. *Int. J. Mach. Tools Manuf.* **2003**, *43*, 1383–1390. [CrossRef]
226. Mishra, D.; Gupta, A.; Raj, P.; Kumar, A.; Anwer, S.; Pal, S.K.; Pal, S. Sensor based real-time information for monitoring and control of a manufacturing process. *Eng. Res. Express* **2021**, *3*, 025040. [CrossRef]
227. Mishra, D.; Gupta, A.; Raj, P.; Kumar, A.; Anwer, S.; Pal, S.K.; Misra, S. Real-time monitoring and control of friction stir welding process using multiple sensors. *CIRP J. Manuf. Sci. Technol.* **2020**, *30*, 1–11. [CrossRef]
228. Silva-Magalhães, A.; de Backer, J.; Martin, J.; Bolmsjö, G. In-situ temperature measurement in friction stir welding of thick section aluminium alloys. *J. Manuf. Process.* **2019**, *39*, 12–17. [CrossRef]
229. Khan, N.Z.; Siddiquee, A.N.; Khan, Z.A.; Bajaj, D.; Ubaid, M. Understanding the dissimilar friction stir welding through force and temperature evolution. *Mater. Today Proc.* **2018**, *5*, 17125–17131. [CrossRef]

230. Leng, J.; Sha, W.; Wang, B.; Zheng, P.; Zhuang, C.; Liu, Q.; Wang, L. Industry 5.0: Prospect and retrospect. *J. Manuf. Syst.* **2022**, *65*, 279–295. [CrossRef]
231. Adel, A. Future of industry 5.0 in society: Human-centric solutions, challenges and prospective research areas. *J. Cloud Comput.* **2022**, *11*, 40. [CrossRef] [PubMed]
232. Noor-A-Rahim, M.; John, J.; Firyaguna, F.; Sherazi, H.H.R.; Kushch, S.; Vijayan, A.; Armstrong, E. Wireless communications for smart manufacturing and industrial IoT: Existing technologies, 5G and beyond. *Sensors* **2022**, *23*, 73. [CrossRef] [PubMed]
233. Wang, H.; Lv, L.; Li, X.; Li, H.; Leng, J.; Zhang, Y.; Thomson, V.; Liu, G.; Wen, X.; Sun, C.; et al. A safety management approach for Industry 5.0′ s human-centered manufacturing based on digital twin. *J. Manuf. Syst.* **2023**, *66*, 1–12. [CrossRef]
234. del Real Torres, A.; Andreiana, D.S.; Ojeda Roldán, Á.; Hernández Bustos, A.; Acevedo Galicia, L.E. A review of deep reinforcement learning approaches for smart manufacturing in industry 4.0 and 5.0 framework. *Appl. Sci.* **2022**, *12*, 12377. [CrossRef]
235. Mincă, E.; Filipescu, A.; Cernega, D.; Șolea, R.; Filipescu, A.; Ionescu, D.; Simion, G. Digital Twin for a Multifunctional Technology of Flexible Assembly on a Mechatronics Line with Integrated Robotic Systems and Mobile Visual Sensor—Challenges towards Industry 5.0. *Sensors* **2022**, *22*, 8153. [CrossRef]
236. Chen, G.; Zhu, J.; Zhao, Y.; Hao, Y.; Yang, C.; Shi, Q. Digital twin modeling for temperature field during friction stir welding. *J. Manuf. Process.* **2021**, *64*, 898–906. [CrossRef]
237. Roy, R.B.; Mishra, D.; Pal, S.K.; Chakravarty, T.; Panda, S.; Chandra, M.G.; Chakravarty, D.; Misra, S. Digital twin: Current scenario and a case study on a manufacturing process. *Int. J. Adv. Manuf. Technol.* **2020**, *107*, 3691–3714. [CrossRef]